

## **General Disclaimer**

### **One or more of the Following Statements may affect this Document**

- This document has been reproduced from the best copy furnished by the organizational source. It is being released in the interest of making available as much information as possible.
- This document may contain data, which exceeds the sheet parameters. It was furnished in this condition by the organizational source and is the best copy available.
- This document may contain tone-on-tone or color graphs, charts and/or pictures, which have been reproduced in black and white.
- This document is paginated as submitted by the original source.
- Portions of this document are not fully legible due to the historical nature of some of the material. However, it is the best reproduction available from the original submission.

(NASA-CR-153294) FINAL REPORT ON TECHNICAL  
WORK ACCOMPLISHED UNDER CONTRACT NASW-2953  
Final Report, 1 Jul. 1976 - 30 Jun. 1977  
(TRW Defense and Space Systems Group) 148 p  
HC A07/MF A01

N77-27258  
THRU  
N77-27263  
Unclass  
15039

CSSL 20N G3/32

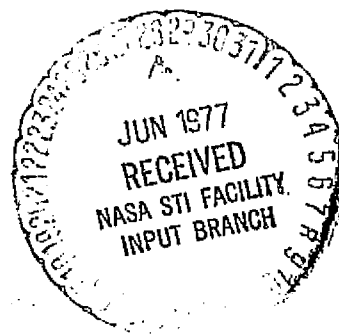
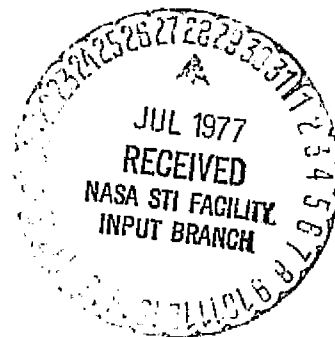
FINAL REPORT  
ON  
CONTRACT NASw-2953

TRW REPORT NUMBER 29697-6002-RU-00

PERIOD: JULY 1, 1976 to JUNE 30, 1977

Prepared for: NASA HEADQUARTERS  
CODE ST  
WASHINGTON, D.C. 20546  
ATTN: Dr. W.W.L. Taylor

Prepared By: R.W. FREDRICKS, Principal Investigator  
Plasma Physics Department  
RI/2012  
TRW Defense & Space Systems Group  
Redondo Beach, California 90278  
(213) 536-1063  
JUNE 30, 1977



FINAL REPORT  
ON  
CONTRACT NASw-2953

TRW REPORT NUMBER 29697-6002-RU-00  
PERIOD: JULY 1, 1976 to JUNE 30, 1977

Prepared for: NASA HEADQUARTERS  
CODE ST  
WASHINGTON, D.C. 20546  
ATTN: Dr. W.W.L. Taylor

Prepared By: R.W. FREDRICKS, Principal Investigator  
Plasma Physics Department  
RI/2012  
TRW Defense & Space Systems Group  
Redondo Beach, California 90278  
(213) 536-1063

JUNE 30, 1977

## CONTENTS

GENERAL INTRODUCTION . . . . .	1
ORAL PRESENTATIONS AND PUBLICATIONS . . . . .	2

### APPENDICES

A OBLIQUE WHISTLER INSTABILITIES (44 pages) . . . . .	A-1
B CURRENT-LIMITED BEAM INJECTION (31 pages) . . . . .	B-1
C THREE-DIMENSIONAL ION SOUND TURBULENCES (51 pages) . . . . .	C-1
D THEORETICAL ASPECTS OF SOUNDER ANTENNA OPERATION (12 pages) . . . . .	D-1
E WHISTLER MODES IN BOW SHOCKS (7 pages) . . . . .	E-1

## GENERAL INTRODUCTION

This document represents the Final Report on technical work accomplished under Contract NASW-2953 for the period 1 July 1976 to 30 June 1977.

The organization of the Report is as follows. This General Introduction Section is followed by a brief section listing all of the oral presentations of work under the contract to scientific meetings, and of all technical papers either submitted to or accepted by technical journals.

The technical work accomplished is then presented in five Appendices, each in the format of a technical paper, and therefore almost self-contained. Each Appendix contains its own summary and/or conclusions section.

These Appendices are, in order, titled Oblique Whistler Instabilities, Current-Limited Electron Beam Injection, Three-Dimensional Ion Sound Turbulence, Theoretical Aspects of Sounder Antenna Operation, and Whistler Modes in Bow Shock Structures.

The first three Appendices represent experimental work performed in TRW's LAMPS facility under the direction of Dr. Reiner L. Stenzel. The final two Appendices are theoretical work. The work on sounder antenna theory was done by Dr. R.W. Fredricks, while the work on whistler modes in bow shocks was performed by E.W. Greenstadt. All work reported here was performed under the supervision of Dr. R.W. Fredricks, the Principal Investigator.

ORAL PRESENTATIONS AND PUBLICATIONS

The following oral presentations of work under this contract were made by the person whose name is underlined:

1. R.W. Fredricks and R.L. Stenzel: "Observations of Return-Current-Driven Ion Acoustic Instabilities in a Beam-Plasma System," paper SM-34, Annual Fall Meeting, American Geophysical Union, San Francisco, December 1976.
2. R.L. Stenzel and R.W. Fredricks: "Observation of Beam-Generated VLF Hiss in a Large Laboratory Plasma," paper SM-35, Annual Fall Meeting, American Geophysical Union, San Francisco, December 1976.
3. R.W. Fredricks: "Laboratory Experiments of Interest to Space Plasma Physics," paper SM-49C, Annual Spring Meeting, American Geophysical Union, Washington, D.C., June 1977.

The following technical papers have been accepted for publication in the journals listed:

1. R.L. Stenzel: "Observation of Beam-Generated VLF Hiss in a Large Laboratory Plasma," accepted by Journal of Geophysical Research-Space Physics, 1977.
2. R.L. Stenzel, "Experiments on Current-Driven Three-Dimensional Ion Sound Turbulence, Part I. Return-Current-Limited Electron Beam Injection," accepted by Physics of Fluids, 1977.
3. R.L. Stenzel, "Experiments on Current-Driven Three-Dimensional Ion Sound Turbulence, Part II. Wave Dynamics," accepted by Physics of Fluids, 1977.

N77-27259

APPENDIX A

OBLIQUE WHISTLER INSTABILITIES

Principal Contributor: R.L. Stenzel

OBSERVATION OF BEAM GENERATED VLF HISS IN A LARGE LABORATORY PLASMA

R.L. Stenzel\*

TRW Systems, Redondo Beach, CA 90278

ABSTRACT

The predicted instability of obliquely propagating whistler waves in a plasma penetrated by an electron beam is verified in a laboratory experiment. The observations support the model for the generation of auroral hiss and compare favorably with ground and satellite observations of VLF hiss. In contrast to the conventional small-diameter laboratory beam-plasma systems the present device is large compared to the characteristic whistler wavelength ( $\lambda = 2-4$  cm, beam and plasma diameter 45 cm, length 250 cm, resp.). Unstable whistlers can therefore, propagate and grow oblique to the beam over many wavelengths before encountering the plasma boundaries. When a cold (1eV), energetic (40 eV), low density ( $n_b = 10^8$  cm<sup>-3</sup>) electron beam is injected along the magnetic field ( $B_0 = 75$  G) into an initially cold ( $kT_e = 1/4$  eV), dense ( $n_e = 10^{10}$  cm<sup>-3</sup>) background plasma the spontaneous emission of broadband rf noise ranging from the lower hybrid frequency  $\omega_{lh}$  to the electron cyclotron frequency  $\omega_c$  is observed. Performing narrowband two-dimensional cross-correlation measurements between two small antennas the rf noise is identified from its dispersion characteristics  $\omega(\vec{k})$  as whistler waves propagating near the oblique resonance angle,  $\theta = \arccos(\omega/\omega_c)$ . The parallel phase velocity is close to the beam velocity ( $\omega/k_{||} \leq v_b$ ). Although the instability amplitude is far above the thermal noise level, it is not large enough to give rise to significant nonlinear effects. The instability saturates when the higher frequency short wavelength electrostatic instability near the electron plasma

frequency ( $\omega_p^2 \gg \omega_c^2$ ) forms a plateau in the beam distribution. Time and space resolved electron pitch-angle distribution function measurements are performed. The propagation of the whistlers out of the instability region and refraction into electromagnetic whistlers is observed. Finally, in the unstable system, coherent whistler waves are launched from a small antenna. In the direction opposing the beam the wave energy diverges along the resonance cone of angle  $\theta_c = \arcsin(\omega/\omega_c)$  just as in a stable plasma. But in the direction of the beam, an unstable oblique whistler wave with a well-defined wave number is excited. The wave normal is at an angle  $\theta = \pm \arccos(\omega/\omega_c)$  with respect to  $\vec{B}_0$ , and the amplitude increases away from the source at the complementary angle. Thus out of the broad  $\vec{k}$ -vector spectrum excited by a point source the most unstable mode of the system predominates. These observations are relevant to the radiation characteristics of satellite antennas in regions of electron precipitation.

## 1. INTRODUCTION

The phenomenon of auroral hiss has received considerable attention. The present model for the generation of VLF hiss is that of a collective interaction of an electron beam with a dense background plasma [Swift and Kan, 1975; Maggs, 1976]. An electrostatic instability arises when the beam velocity matches the parallel phase velocity of an oblique whistler wave [Brinca, 1972] which can be very small when the wave propagates near the oblique resonance. Many observations from ground, rockets and satellites are consistent with the above model [Helliwell, 1965; Laaspere et al., 1971; Gurnett and Frank, 1972; James, 1973]. The measurements usually consist of noise frequency spectra and electron pitch angle distribution functions. There are fundamental limitations of measuring wave normals or rays from a single observation point. These essential aspects of the instability are usually inferred so that a conclusive proof of the mechanism cannot be given. It is suggested that a carefully designed laboratory experiment can supply this and other complementary information and thereby contribute to the understanding of the VLF hiss phenomenon.

This paper describes a laboratory experiment on a beam-plasma instability under conditions for which the theory of VLF hiss is applicable. An energetic electron beam is injected into a cold, dense, almost collisionless magnetoplasma. Beam and plasma dimensions are so large that oblique whistler wave propagation and growth are readily observable. In this aspect the present experiment fundamentally differs from most previous laboratory experiments with small diameter beam-plasma systems which are restricted to one-dimensional wave propagation [Malmberg and Wharton, 1969; Bollinger et al., 1974; Gentle and Lohr, 1973]. The present situation models in many aspects the conditions inside an auroral arc. It does not apply to the wave propagation and refraction effects outside the arc since beam and

plasma diameters are identical. Whistler wave propagation in the absence of the beam have been reported earlier [Stenze], 1976 a, b, c].

The observations show that the beam generates broadband rf noise ( $\omega_{ih} < \omega < \omega_c$ ). By analyzing the frequency and wavenumber spectrum, i.e. the dispersion  $\omega(\vec{k})$ , the noise is identified as whistler waves propagating near the oblique resonance cone with parallel phase velocity slightly less than beam velocity. This is a direct confirmation of the essential prediction from the instability theory.

The dynamics of the beam and background plasma are investigated. It is concluded that the simultaneously occurring short wavelength electrostatic instability near the electron plasma frequency ( $\omega_p > \omega_c$ ) is responsible for the scattering of the beam and the saturation of the oblique whistler instability.

Finally, wave propagation experiments are performed by launching coherent "test" waves from a small antenna in the unstable region. In the direction opposing the beam the point source excites at a given frequency a broad wave number spectrum,  $k(\theta)$ , which interferes to give the familiar resonance cone pattern [Fisher and Gould, 1971; Kuehl, 1962]. But in the direction with the beam the most unstable mode with  $k_{||} \geq \omega/v_b$  and  $k_{\perp}/k_{||} = \tan\theta = (\omega_c^2/\omega^2 - 1)^{1/2}$  dominates, i.e. a single oblique whistler mode is excited whose wave normal angle is close to that for oblique resonance and whose amplitude grows in the ray direction at nearly the complementary angle.

The connection and relevance of the laboratory results on observations in space are discussed in the last section.

## II. EXPERIMENTAL SET-UP AND MEASUREMENT TECHNIQUES

The experiment is performed in a laboratory plasma source designed to produce a large diameter uniform collisionless magnetoplasma. The device which has previously been described in more detail [Stenzel, 1976 a, c] consists briefly of a dc discharge between a solid oxide-coated cathode of approx. 1/2 m diam. and adjacent grid anode [Fig. 1(a)]. The plasma is confined by a uniform axial magnetic field ( $B_0 = 75$  G) and terminated after 2.5 m by a floating end wall. As shown in Fig. 1(b), the discharge is pulsed repetitively. The first pulse produces an afterglow background plasma which is cold ( $kT_e = kT_i = 0.25$  eV), dense ( $10^9 < n_e < 10^{11}$  cm<sup>-3</sup>,  $1 < \omega_p/\omega_c < 10$ ), weakly collisional (electron-neutral collisions  $\nu_{en}/\omega_c \approx 10^{-4}$ , coulomb collisions  $\nu_{ei}/\omega_c \approx 10^{-3}$ ) and free of low or high frequency instabilities. At a desired afterglow time a second voltage pulse is applied to the cathode whereby a beam of fast electrons is injected along  $\vec{B}_0$  into the afterglow plasma. Beam and background plasma parameters are determined from plane Langmuir probes which can be positioned radially and axially. Independently, the density is determined from dispersion measurements of whistler waves, Langmuir waves and Bernstein waves, and from resonance cone measurements. High frequency signals are detected and/or excited with two identical short wire rf probes (5 mm long exposed center wire of 50  $\Omega$  semirigid coax cables) one of which is movable along and across  $\vec{B}_0$ . Due to the pulsed nature of the experiment all data are sampled and averaged over many highly reproducible events. By varying the sampling time and probe position time and space resolved data are obtained so that one can follow the evolution of the beam plasma interaction from turn-on to steady state.

### III. PLASMA AND BEAM PROPERTIES

First, the background plasma properties are presented. Fig. 2 shows the density decay of the afterglow plasma. The density is measured by different independent techniques which, in general, show good agreement. The plasma decay is due to ambipolar diffusion where the dominant loss is due to surface recombination on the cathode, anode and axial end wall. Radially, the plasma is separated from the chamber wall by a 20 cm wide gap in which the density is negligibly small.

The electron temperature during the active discharge is approximately  $kT_e \approx 2\text{eV}$ . In the afterglow, at  $t_a \geq 10$  msec, the temperature has decreased  $kT_e = kT_i = 0.25$  eV. The electron temperature is determined from Langmuir probe measurements and, independently, from the dispersion of ion acoustic waves. Landau damping of ion sound waves yields the estimate of the ion temperature. Other important parameters of the background plasma are listed in Table 1.

The electron beam is injected into the background plasma whose density is determined by the afterglow time  $t_a$ . Beam and background plasma strongly interact and change their initial properties to new steady-state values. Figure 3 shows the electron distribution function sampled at different times  $t_s$  after the step-like turn on of the beam voltage  $V_b$  at an afterglow time  $t_a = 15$  msec. The distribution function is obtained by differentiating the current-voltage characteristics [ $f_e(V) \propto di/dV$ ] of a one-sided plane Langmuir probe located at a distance  $z = 7$  cm from the anode with its surface normal pointing toward the beam source. One can see that initially ( $0 < t_s < 30$   $\mu\text{sec}$ ) a cold electron beam is injected into a cold background plasma ( $kT_b < kT_e \ll eV_b$ ). This system is highly unstable to electrostatic instabilities. With increasing time the beam

broadens ( $t_s \approx 40 \mu\text{sec}$ ), forms a plateau ( $t_s \approx 50 \mu\text{sec}$ ), and finally ( $t_s \geq 60 \mu\text{sec}$ ) becomes the tail of a distribution with continuously decreasing slope,  $\partial f_e / \partial v_z < 0$ . On the same time scale, the background electrons are strongly heated such that both distributions finally merge. One also observes that beam electrons are accelerated to energies larger than their initial injection energy. This fact as well as the short penetration length of the beam compared to the electron mean free path indicate that the beam is scattered by electrostatic instabilities rather than by collisional processes.

On a longer time scale, however, the beam electrons undergo collisions with the low pressure background gas. When the beam energy exceeds the ionization potential ( $E_i \approx 14 \text{ eV}$  in krypton), the plasma density increases. Ionization phenomena become noticeable for  $t_s \geq 50 \mu\text{sec}$ . When a 40 eV beam pulse is applied for approx. 500  $\mu\text{sec}$ , which are the typical conditions of the discharge pulse, the density rises to the value at  $t_s=0$  ( $n_e = 2 \times 10^{11} \text{ cm}^{-3}$ ). For the purpose of the present experiment, however, the initial period ( $0 < t_s \leq 50 \mu\text{sec}$ ) of the beam injection is of particular interest since unstable distribution functions are clearly observable and collective processes dominate. This period is long compared to the time scale of the rf instabilities.

The spatial properties of beam and plasma distributions at a given time  $t_s = 10 \mu\text{sec}$  are shown in Fig. 4. With increasing distance  $z$  from the injection point the beam broadens and the background electron temperature and density build up. Unstable beam distributions only persist up to distances  $z \leq 20 \text{ cm}$  from the cathode. The penetration depth depends on beam speed and density but not on neutral pressure.

Typical radial and axial density profiles in the vicinity of the cathode where the oblique whistler instability is investigated are shown in Fig. 5. The density variations appear small enough to consider the medium as uniform. The magnetic field is spatially uniform to within  $\pm 0.5\%$  and temporally constant to within  $0.1\%$ .

The probe measurements presented so far give only information about the parallel electron distribution function. By rotating the one-sided plane Langmuir probe, as sketched in Fig. 8, the pitch angle distribution can be estimated. Figure 6(a) shows the distribution function at different angles  $\phi$  between the surface normal and the magnetic field. The measurements are taken near the cathode ( $z = 7$  cm). At  $\phi = 0$  the probe faces the beam and a large beam current  $I_b$  is collected when  $|V_p| < V_b$ . With increasing angle  $\phi$  the peak of the beam distribution shifts to smaller retarding potentials  $|V_p|$  and the beam current decreases until no beam is detected when the probe surface is parallel to  $\vec{B}_0$ . This behavior identifies the beam as being cold and parallel to  $\vec{B}_0$ . The beam temperature  $kT_b$  can be estimated from the energy spread  $\Delta V_p$  near onset,  $kT_b \approx (1/4)eV_b (\Delta V_p/V_b)^2 \approx 0.5$  eV. When the probe is inclined at an angle  $\phi$ , the normal beam velocity component is  $v_b \cos\phi$  and beam particles are detected at probe voltages  $|V_p| < V_b \cos^2\phi$ . The collected current decreases as  $\cos^2\phi$  [see Fig. 6(b)] because both the normal beam flux and the probe area projected along  $\vec{B}_0$  decrease as  $\cos\phi$ . The background plasma, however, exhibits a relatively isotropic distribution.

Figure 7 shows a similar measurement as Fig. 6, but it is taken in the center of the plasma device ( $z = 125$  cm) where the beam has been modified by electrostatic instabilities. The probe current increases exponentially indicating that the beam has been thermalized ( $kT_b \approx 8$  eV). The angular variation shows a continuous decrease in energetic particle current with increasing angle  $\phi$  but little change in the energy spread.

For  $\phi = 90^\circ$  the flux at a given voltage is more than an order of magnitude smaller than for  $\phi = 0$ , and for  $\phi = 180^\circ$ , particles at the incident beam velocity cannot be detected within experimental accuracy. These observations indicate that the beam is not scattered isotropically but mainly broadened along  $\vec{B}_0$  in the direction of injection. Some angular spread occurs since a small energetic perpendicular flux is observed. The distribution function is stable against high frequency electrostatic instabilities and exhibits no perpendicular temperature anisotropy.

While Fig. 7 shows only the energetic particle distribution, Fig. 8 includes the behavior of the background plasma. The bulk electron temperature is approximately  $kT_e = 3$  eV. However, due to the thermalized beam, the parallel distribution function is asymmetric. Since the electron saturation current is identical in both directions, the plasma is current free which is consistent with the fact that the discharge current flows only in the 1 cm wide gap between cathode and anode. The injected beam current passing through the mesh anode (70% transparent) is exactly balanced by a return current to the anode. This current consists of background electrons drifting toward the anode. The drift velocity is smaller than the beam velocity by the ratio of beam to background electron density ( $n_b/n_e = 10^{-2}$ ). This small drift ( $m_e v_d^2 / 2 < 1$  eV) which is not even noticeable in Fig. 8 has no direct effect on the high frequency instabilities. However, since  $v_d \gg c_s = (kT_e/m_i)^{1/2}$  ion acoustic waves are driven unstable [Mikhailovski, 1974] and the resultant strong turbulence [Kadomtsev, 1965] scatters high frequency waves. The observations on ion sound turbulence driven by the return current are beyond the scope of the present paper and will be discussed elsewhere [Stenzel, 1977].

#### IV. INSTABILITY ANALYSIS

The onset of an instability upon beam injection becomes apparent through the large rf noise level detected with electric or magnetic antennas inside the plasma. Fig. 9(a) shows the coincidence between rf noise and electron beam. The top trace is the rf potential fluctuation which, for purpose of display, has been heterodyned with a local oscillator at  $f = 100$  MHz ( $\omega / \omega_c = 0.47$ ). The bottom trace shows the beam current pulse applied at  $t_a = 10$  msec in the afterglow of the main discharge. After an initial transient, the current is constant during the first 50  $\mu$ sec and then rises as the density builds up. As outlined earlier, the beam current is balanced by the return current to the anode which is limited by the electron saturation current of the background plasma. The comparison between the two traces clearly shows that the rf is generated only in the presence of the electron beam. This coincidence holds for a wide range of frequencies extending from the regime of ion acoustic waves to that of electron plasma waves.

The high frequency signals are applied to a spectrum analyzer with fast output response (300 kHz bandwidth). Figure 9(b) shows the frequency spectrum in the whistler wave regime sampled at  $t_s = 100$   $\mu$ sec after turn-on of the beam pulse. The top trace is the rf potential from a short-wire antenna near the region of beam injection, the bottom trace is the magnetic loop signal detected in the middle of the device at  $z = 125$  cm from the cathode. The broadband character of the instability is apparent. The rf magnetic field spectrum is cut off beyond  $\omega / \omega_c = 0.85$  which appears to be the result of refraction and damping of whistlers propagating from the beam injection region to the center of the device where the distribution is stable.

Although, in general, the shape of the whistler wave spectrum depends on beam and plasma parameters there is no particular structure noticeable near the characteristic frequencies, the lower hybrid ( $\omega_{lh}^{-2} = \omega_{pi}^{-2} + \omega_{ce}^{-1} \omega_{ci}^{-1}$ ;  $\omega_{lh}/2\pi = 1$  MHz) and the electron cyclotron frequency ( $\omega_{ce}/2\pi = 210$  MHz). Figure 10 shows a comparison of frequency spectra at two widely different densities [ $\omega_p^2/\omega_c^2 = 2.8$  in (a),  $\omega_p^2/\omega_c^2 = 36$  in (b)]. In the low density case, the frequency scan is extended beyond the whistler wave regime to show the presence of strong high frequency electrostatic instabilities near the electron plasma frequency.

In order to identify the rf noise signals as waves, the spatial properties have been investigated with correlation techniques. Two identical movable antennas are used whose noise signals are passed through narrowband amplifiers, multiplied, time averaged on the high frequency time scale and then sampled and averaged on the longer time scale of the beam pulse. A typical cross correlation signal is plotted vs. axial position in Fig. 11(a). One can see that the noise correlates for a few wavelengths along the beam direction. By measuring the wavelengths for different frequency components, the dispersion  $\omega(k_{||})$  is found. Figure 11(b) shows that the parallel phase velocity is slightly below but close to the beam velocity. This is characteristic for a Cherenkov type beam-plasma instability.

The direction of wave propagation is determined from the measurement shown in Fig. 12. A delay line is inserted in one channel of the correlator [Fig. 12(a)] and the spatial correlation function is plotted at different delay times  $\tau$  [Fig. 12(b)]. From the time-position diagram of stationary phase points of the correlation signal [Fig. 12(c)] one concludes that the waves propagate in the direction of the electron beam at a slightly smaller phase velocity than the beam velocity.

So far, only the component  $k_{||}$  of the wave vector has been determined. The perpendicular wave number  $k_{\perp}$  is found by performing two-dimensional cross correlation measurements. Figure 13 (a) shows a map of the location of minima and maxima of the correlation signal in the r-z plane. One finds that the phase fronts are inclined with respect to the magnetic field. The wavenormal or  $\vec{k}$  makes an angle  $\theta$  with respect to  $\vec{B}_0$  which is close to but below the angle for oblique resonance,  $\theta = \arccos(\omega/\omega_c)$ . According to cold plasma theory [Helliwell, 1965] the dispersion for oblique whistlers is given by

$$\frac{k_{\perp}^2 c^2}{\omega^2} = 1 + \frac{\omega_p^2}{\omega(\omega_c \cos \theta - \omega)} \quad (1)$$

With the experimental parameters  $\omega$ ,  $\omega_p$ ,  $\omega_c$  given in Fig. 13 and the measured oblique wavelength  $\lambda = 2.2$  cm the calculated angle  $\theta$  is found to be  $\theta = 38.9^\circ$  which is in good agreement with the measured value  $\theta = 38.7^\circ$ . The angle for oblique resonance is  $\theta = 40.5^\circ$ .

By measuring various phase front maps at different frequencies one finds that the propagation angle changes with frequency as shown in Fig. 13(b). Over a wide range of frequencies the rf noise is thus identified as oblique whistler waves propagating near the oblique phase velocity resonance cone. Two further observations are worth pointing out. First, the sign of  $\theta$  is found to vary arbitrarily. At some frequencies the waves propagate from the interior of the plasma outward, at other frequencies they propagate inward. Thus, there is no constraint on the direction of wave propagation which is characteristic for an unbounded medium. Second, the amplitude pattern of the cross correlation signal shows a systematic frequency dependence. At lower frequencies ( $\omega/\omega_c \leq 0.5$ ) the correlation length along  $\vec{B}_0$  is larger than across  $\vec{B}_0$ , at higher frequencies ( $\omega/\omega_c \rightarrow 1$ ) the opposite is observed. This behavior is consistent with the fact that group and phase

velocity vectors are essentially perpendicular to one another near the resonance cone. The correlation amplitude is large within the group velocity cone which narrows toward lower frequencies.

A measurement of the absolute value of the instability amplitude involves the knowledge of the coupling properties between antenna and wave. These are difficult to determine theoretically but can be estimated experimentally. For example, as described in the next section, a resonance cone is excited by applying a known small amplitude rf signal to one of the two identical short wire antennas. With the second movable antenna the absolute received signal along the resonance cone is measured. The coupling loss between the two antennas, extrapolated to vanishing probe separation, can be considered as twice the wave-antenna coupling factor for a single antenna (typically -22dB). Similar techniques have previously been used for absolute measurements of electron plasma waves [Malmberg and Wharton, 1967]. With this calibration procedure the absolute rf potential fluctuations are determined to be  $|\phi_{rf}| \approx 8 \text{ mV}$  or  $e|\phi_{rf}|/kT_e \approx 5 \times 10^{-3}$ . At these amplitudes nonlinear wave effects are not considered important.

A second independent measurement of the wave amplitude has been performed in the middle of the plasma device. The oblique whistlers from the instability region near the cathode refract into nearly transverse whistlers which propagate along the entire plasma device and can be observed with electric and magnetic dipole antennas. The absolute wave magnetic field is measured with a shielded loop antenna whose response has been calibrated [Stenzel, 1976 c]. Typical magnetic field strengths  $|B_{rf}| \approx 10^{-3}$  Gauss or  $|B_{rf}|/B_0 \approx 10^{-5}$  are observed which again shows that the wave remains in the linear regime.

## V. TEST WAVE PROPAGATION

The propagation of small amplitude phase coherent waves from antennas does not only provide a conclusive test whether the rf noise is due to incoherent Cherenkov radiation or due to a beam-plasma instability but also provides further information on group and phase velocity directions, growth rates and saturation levels.

When an rf signal ( $\omega_{lh} < \omega < \omega_c < \omega_p$ ) is applied to a small antenna in a Maxwellian plasma, the radiation pattern assumes the shape of two symmetric cones. The origin is at the point source, the axis is along  $\vec{B}_0$  and the half angle is the group velocity resonance cone angle  $\theta_c = \arcsin(\omega/\omega_c)$ . This predicted pattern [Kuehl, 1962] has been observed both in the near zone [Fisher and Gould, 1971] and in the far-zone [Boswell and Gonfalone, 1975; Stenzel, 1976]. The field distribution results from the interference of the wide range of oblique eigenmodes  $k(\theta)$  excited by an oscillating point source.

In the beam-plasma system the radiation pattern shown in Figure 14 is found to be asymmetric along  $\vec{B}_0$ . In the direction against the beam a resonance cone is excited just as in the absence of the beam. Figure 14(a) shows a single localized field maximum when the receiver probe is scanned axially at a fixed radial distance from the cone axis. A two-dimensional scan in the r-z plane [Fig. 14 (b)] shows that the field maxima diverge along two straight lines which, due to azimuthal symmetry represent a cut through a conical radiation pattern. The observed cone angle  $\theta_c = 45^\circ$  agrees with the expected value  $\theta_c = \arcsin(\omega/\omega_c) = 45.2^\circ$ . Since the wave energy flows along the cone through an increasing cross section, the wave amplitude rapidly decreases with distance from the exciter. Contour maps of equal relative rf potential  $|\phi_{rf}(r,z)|$  are shown in Fig. 14(e).

In the direction with the beam the interferometer trace, Fig. 14(b), reveals a well defined wave. Its amplitude grows with increasing distance from the exciter, its parallel phase velocity ( $f\lambda_{||} = 3.7 \times 10^8$  cm/sec) is close the beam velocity. The phase fronts shown in Fig. 14(d) are oblique with respect to  $B_0^{\rightarrow}$  and the wave normal makes an angle  $\theta = 90 - \theta_c = \pm 45^\circ$  with respect to  $B_0^{\rightarrow}$ . Thus, just as is the spontaneous noise emission, the test wave is an oblique whistler wave propagating near the resonance cone. The amplitude distribution shown in Fig. 14(f) indicates that the direction of maximum growth, i.e. the group velocity direction is also oblique to  $B_0^{\rightarrow}$  and is nearly perpendicular to the phase velocity direction. These observations directly confirm the predicted oblique whistler instability in a beam-plasma system.

The test waves are propagated in the presence of the background noise. Since phase coherent detection is employed and test wave amplitudes above the noise level are chosen, the excited waves are readily distinguished from the background. The fact that the test wave grows indicates that the instability is not yet saturated which is consistent with the relatively small noise amplitudes measured previously. Although the instability shows a broad spectrum of incoherent waves, it cannot be considered as a turbulent system in the sense that strong wave-wave or wave-particle interactions would take place. For the test wave, Fig. 14(f) gives an oblique e-folding growth length  $k_i^{-1} = 3.5$  cm and Fig. 14(d) gives the oblique wavelength  $\lambda = 2\pi/k_r = 1.8$  cm. Because of the conical field distribution the measured normalized growth rate,  $k_i/k_r = 8 \times 10^{-2}$ , is smaller than that for a plane wave so that a comparison with theory cannot be easily given. Nevertheless, one can estimate that a whistler at  $\theta = \theta_c = 45^\circ$  grows by at least 8 e-folding

lengths ( $\sim 70$ dB) after propagating obliquely through half the column of 20cm radius. Further convective growth is limited by the fact that the higher frequency instabilities ( $\omega \approx \omega_p$ ) nonlinearly modify the beam.

A continuous transition from a resonance cone pattern to a growing wave due to a variation in beam voltage is shown in Fig. 15. The probe arrangement is the same as in Fig. 14(b). At low beam voltages there is a mixed pattern between cones and waves. The wavelengths can be as short as the half-width of the unperturbed cone; the refractive index for these oblique whistlers is  $n \approx 150$  whereas  $n \approx 4$  for a parallel propagating whistler. Warm plasma modes [Fisher and Gould, 1971; Kuehl, 1973] are not observed. As the beam voltage is increased, the cone structure vanishes, the parallel wavelength and the growth rate increase. The latter may be due to an increase in the ratio of beam to background density with beam voltage.

The importance of the simultaneously occurring electrostatic instabilities near the plasma frequency has been stressed and their presence indicated in Figure 10(a). Figure 16 shows the behavior of a high frequency test wave near the most unstable upper frequency component of the noise spectrum. Figure 16(a) indicates that for a constant applied signal to the antenna large amplitude waves are only excited in the presence and direction of the beam. Although the waves are excited from a point source, the wave fronts shown in Fig. 16(b) are essentially plane and propagation is parallel to the beam. Due to the long interaction length with the beam, these waves exchange energy with the beam most efficiently, which leads to beam broadening and quenching of the instability. The temporal growth rate for the hydrodynamic beam plasma instability is given by [Mikhailovskii, 1974]

$$\gamma = \omega_p \frac{\sqrt{3}}{2^{4/3}} \left( \frac{n_b}{n_e} \right)^{1/3} . \quad (2)$$

Spatial and temporal growth rates are related by  $k_{\parallel} = \gamma/v_g$  where the group velocity is approximately given by the beam velocity. For  $n_b/n_e = 10^{-2}$  one finds  $k_{\parallel}^{-1} = 1$  cm which is much shorter than the whistler wave growth length component along  $B_0^+$ .

The hydrodynamic instability corresponds to the case of a cold beam with  $a_b/v_b < (n_b/n_e)^{1/3}$  where  $a_b$ ,  $v_b$  are thermal and directed beam velocities, respectively. For a typical beam density  $n_b/n_e = 1\%$  the beam energy spread is restricted to  $\Delta v_b/v_b = 2a_b/v_b < 0.43$ . Figures 3 and 4 show that this condition is satisfied in time up to  $\sim 40$   $\mu$ sec after beam injection and in space up to  $\sim 15$  cm from the beam source. Due to the injection of a cold beam the largest amplitude mode near  $f = 350$  MHz in the high frequency spectrum of Fig. 10(a) can be associated with the plasma frequency rather than the upper hybrid mode. The latter would imply highly oblique propagation which, according to Fig. 16(a) is not observed. The structures in the frequency range  $f_c < f < f_p$  in Fig. 10(a) are not associated with characteristic frequencies of the plasma and are simply unstable modes on the beam with real frequency given by  $\omega = kv_b$ .

## VI. DISCUSSION

The laboratory observations show many similarities with phenomena observed on natural VLF hiss in space. The basic agreement is that VLF hiss is associated with the presence of an electron beam passing through a background plasma. A wide range of beam velocities gives rise to the instability. A broad band of frequencies is excited which shows little structure when the observer is inside the beam plasma system. The frequency spectra observed by James [1973] on Isis-1, which passed through regions of electron precipitation, are very similar to the spectra measured in the

laboratory. The various characteristic shapes of the frequency-time plots such as saucers and inverted v's shown by Gurnett and Frank [1972] are due to propagation effects between the instability region and the moving observer outside the arc. Likewise, observations from ground are strongly affected by wave reflection and refraction processes. The laboratory experiment cannot model such propagation effects involving magnetic field and density gradients and long propagation distances. It does, however, provide much more insight into the generation mechanism of VLF hiss than spacecraft or ground observations. The theoretically predicted coherent Cherenkov-type instability of oblique whistlers is clearly identified through direct measurements of wavenumber spectra, group and phase velocities, growth rates, instability amplitudes and electron distributions. The observations also show that the Cherenkov type instability is dominant over other beam-plasma instabilities, for example the cyclotron-type instability associated with the anomalous Doppler effect,  $\omega = k_{\parallel} v_b - \omega_c$ , [Mikhailovski, 1974]. No evidence is found for this instability, presumably due to its smaller growth rate. Various authors [Hashimoto and Matsumoto, 1976; Matsumoto and Yasuda, 1976; Cuperman et al., 1976] consider only wave propagation parallel to  $B_0^{\rightarrow}$  which is too restrictive for an unbounded medium.

The present experiment also provides insight into the evolution of the beam-plasma system. The electrostatic instabilities of a cold beam plasma system are so strong that the beam rapidly spreads in velocity space. Most observations of the electron pitch-angle distribution in auroral arcs [Reasoner and Chappell, 1973; Frank and Ackerson, 1971] show beams with significant energy spread. Although the mechanism for beam generation is not fully understood, it is possible that the energy spread is the result of electrostatic instabilities as observed in the laboratory.

The finite spatial extent of the beam limits the convective amplitude growth of the oblique whistlers both in the laboratory and in space. However, wave propagation near the resonance cone is slow and the wave amplitude can grow well above the level of incoherent Cherenkov radiation. For very low energy electron beams when the wavelength is within the resonance cone width, the instability in the laboratory vanishes. In space, Gurnett and Frank [1972] also observe a threshold electron energy level below which VLF hiss is not observed.

The test wave propagation experiments which give useful information on the instability in the laboratory could also be performed in space. James [1975] has observed propagation near the resonance cone in intersatellite radio transmissions between two of the Alouette-Issis spacecraft. If such "mother-daughter" type wave propagation experiments are performed in regions of electron precipitation, the transmission would be non-reciprocal exhibiting one-way amplification.

## VII. SUMMARY AND CONCLUSION

The present paper describes an experimental investigation of a beam-plasma instability which is assumed to be the mechanism for generating auroral VLF hiss. The experiment is performed in a laboratory plasma of characteristic dimensions large compared to the growth length of the instability. The plasma parameters are appropriate for modeling the electrostatic instability of an oblique whistler wave driven resonantly by a parallel electron beam. The observations of frequency and wavenumber spectra, growth rate and instability level are consistent with theory and satellite observations in regions of electron precipitation. Due to the variety of diagnostic tools, a scaled laboratory experiment provides information not available from observations in space, and may thereby contribute to the understanding of the physics of VLF hiss.

#### ACKNOWLEDGEMENTS

The author wishes to express thanks to Drs. R.W. Fredricks and J. Maggs for many useful discussions. The expert technical assistance by Mr. W.F. Daley is gratefully acknowledged. This work was supported in part by a NASA contract NASW-2953 and in part by TRW Independent Research and Development Funds.

#### REFERENCES

\*Present address: Dept. of Physics, University of California, Los Angeles, California 90024.

Bollinger, L.D., W. Carr, H. Liu, and M. Seidl, Beam-Plasma Instability in an Inhomogeneous Plasma, Phys. Fluids 17, 2142-2143, 1974.

Boswell, R.W., and A. Gonfalone, Interference Structure in the Far-Field of the Resonance Cone, Physics Letters 51A, 485-486, 1975.

Brinca, A.L., On the Stability of Obliquely Propagating Whistlers, J. Geophys. Res. 77, 3495-3507, 1972.

Cuperman, S., I. Roth, and W. Bernstein, Theory and Computer Simulation of Electron-Beam Plasma Interactions in Unbounded Systems, J. Plasma Phys. 15, 309-324, 1976.

Fisher, R.K., and R.W. Gould, Resonance Cones in the Field Pattern of Radio Frequency Probe in a Warm Anisotropic Plasma; Phys. Fluids 14, 857-867, 1971.

Frank, L.A., and K.L. Ackerson, Observations of Charged Particle Precipitation Into the Auroral Zone, J. Geophys. Res. 76, 3612-3643, 1971.

Gentle, K.W., and J. Lohr, Experimental Determination of the Nonlinear Interaction in a One-Dimensional Beam-Plasma System, Phys. Fluids 16, 1464-1471, 1973.

Gurnett, D.A., and L.A. Frank, VLF hiss and related plasma observations in the polar magnetosphere, J. Geophys. Res. 77, 172-190, 1972.

- Hashimoto, K., and H. Matsumoto, Temperature Anisotropy and Beam Type Whistler Instabilities, *Phys. Fluids* 19, 1507-1512, 1976.
- Helliwell, R.A., Whistlers and Related Ionospheric Phenomena, p. 288, Stanford University Press, Palo Alto, California, 1965.
- James, H.G., Whistler-mode hiss at low and medium frequencies in the dayside-cusp ionosphere, *J. Geophys. Res.* 78, 4578-4599, 1973.
- James, H.G., private communication, 1975.
- Kuehl, H.H., Interference structure near the resonance cone, *Phys. Fluids* 16, 1311-1320, 1973.
- Kuehl, H.H., Electromagnetic radiation from an electric dipole in a cold anisotropic plasma, *Phys. Fluids* 5, 1095-1104, 1962.
- Laaspere, T., W.C. Johnson, and L.C. Temprebon, Observations of Auroral hiss, LHR noise, and other phenomena in the frequency range 20 Hz to 540 kHz on Ogo 6, *J. Geophys. Res.* 76, 4477, 1971.
- Malmberg, H.H., and C.B. Wharton, Collisionless damping of large-amplitude plasma waves, *Phys. Rev. Lett.* 19, 775-778, 1967.
- Malmberg, H.H., and C.B. Wharton, Spatial growth of waves in a beam-plasma system, *Phys. Fluids* 12, 2600-2606, 1969.
- Maggs, J.R., Coherent generation of VLF hiss, *J. Geophys. Res.* 81, 1707-1724, 1976.
- Matsumoto, H., and Y. Yusada, Computer simulation of nonlinear interaction between a monochromatic whistler wave and an electron beam, *Phys. Fluids* 19, 1513-1522, 1976.
- Mikhailovskii, A.B., Theory of Plasma Instabilities, vol. 1, p. 219-223, Consultants Bureau, New York, 1974.
- Kadomtsev, B.B., Plasma Turbulence, p. 68-73, Academic, New York, 1965.
- Reasoner, D.L., and C.R. Chappell, Twin payload observations of incident and backscattered auroral electrons, *J. Geophys. Res.* 78, 2176-2286, 1973.

Swift, D.W., and J.R. Kan, A theory of auroral hiss and implications on the origin of Auroral Electrons, J. Geophys. Res. 80, 785-992, 1975.

Stenzel, R.L., Whistler wave propagation in a large magnetoplasma, Phys. Fluids 19, 857-864, 1976 a.

Stenzel, R.L., Filamentation instability of a large amplitude whistler wave, Phys. Fluids 19, 865-871, 1976 b.

Stenzel, R.L. Antenna radiation patterns in the whistler wave regime measured in a large laboratory plasma, Radio Science 11, 1045-1056, 1976 c.

Stenzel, R.L., Experiments on strong three-dimensional current-driven ion sound turbulence, to appear in Phys. Fluids, 1977.

FIGURE CAPTIONS

- Fig. 1 (a) Schematic diagram of plasma device.  
(b) Typical time sequence during one period (25 msec) of the pulsed beam injection experiment.
- Fig. 2 Density decay of the afterglow plasma measured by independent techniques.  $B_0 = 75$  Gauss.
- Fig. 3 Electron distribution function  $||\vec{B}_0$  sampled at different times  $t_s$  after the turn-on of the beam pulse. The figure demonstrates the broadening of the beam and heating of the background plasma in time at a fixed distance  $z$  from the anode.  $t_a = 15$  msec.
- Fig. 4 Electron distribution function  $||\vec{B}_0$  sampled at different distances  $z$  from the cathode for a fixed time  $t_s$  after beam injection. The figure shows that beam and background heating occur over distances short compared to the electron mean free path ( $l_e \approx 90$  cm).  $t_a = 24$  msec.
- Fig. 5 (a) Radial density profile of beam and background plasma:  
 $n_b = 5 \times 10^7 \text{ cm}^{-3}$ ,  $n_0 = 2 \times 10^9 \text{ cm}^{-3}$ ,  $z = 7$  cm,  $t_a = 24$  msec,  
 $B_0 = 75$  G.  
(b) Axial density profile with and without beam.  $r = 0$ ,  $t_a = 24$  msec.  
The figure shows that the beam-plasma system is reasonably uniform in the beam injection region where the instability is investigated.
- Fig. 6 (a) Differentiated current-voltage characteristics of a plane one-sided Langmuir probe at different angles  $\phi$  between surface normal and magnetic field (see sketch in Fig. 8). Beam retardation voltage and beam current [see part (b)] vanish as  $\phi \rightarrow 90^\circ$  whereas the background electron current is rather

insensitive to probe orientation. The electron pitch angle distribution in the beam injection region ( $z = 7$  cm) is that of an energetic, cold electron beam passing along  $\vec{B}_0$  through an isotropic background plasma.  $t_a = 24$  msec,  $B_0 = 75$  G.

Fig. 7 Plane, one-sided Langmuir probe characteristics in the electron retardation region,  $\log I_p$  vs.  $V_p$ , for different probe angles  $\phi$  at a large distance from the cathode ( $z = 125$  cm). The beam has been mainly broadened in the direction of beam injection ( $kT_b = 8$  eV) although some side scattering is observable. The beam shows no temperature anisotropy.

Fig. 8 Langmuir probe traces in the middle of the plasma device ( $z = 125$  cm) for the probe facing the beam ( $\phi = 0$ ) and opposing it ( $\phi = 180^\circ$ ). The plasma is free of a net current implying that the beam current is balanced by a return current consisting of slowly drifting background electrons ( $c_s \ll v_d < v_e$ ).

Fig. 9 (a) Rf noise at  $\omega/\omega_c = 0.47$  (top trace) and beam current pulse (bottom trace) vs. time, showing the cause-effect relationship between beam and rf emission.  $t_a = 15$  msec.

(b) Frequency spectrum of the spontaneous emission sampled at  $t_s = 100$   $\mu$ sec after beam injection.  $\phi_{rf}$  is the electrostatic signal detected in the instability region ( $e|\phi_{rf}|/kT_e = 5 \times 10^{-3}$ ) and  $B_{rf}$  is the wave magnetic field of whistlers detected 100 cm away from the excitation region.

$$|B_{rf}|/B_0 = 10^{-5}, B_0 = 75 \text{ G}, \omega_p/\omega_c = 5.$$

Fig. 10 Comparison of the instability frequency spectra at low densities

$[\omega_p^2/\omega_c^2 = 2.8$  in (a)] and high densities  $[\omega_p^2/\omega_c^2 = 36$  in (b)].

The high frequency instabilities ( $\omega_c < \omega < \omega_p$ ) are also shown in (a).

The observed spectra have the frequency response of the antenna folded in.

- Fig. 11 (a) Cross correlation signal between two narrowband noise signals obtained from a fixed reference antenna and an identical antenna movable along  $\vec{B}_0$ . The parallel wavelength ( $\lambda_{||} = 1.75\text{cm}$ ) is much shorter than that of a whistler propagating along  $\vec{B}_0$  ( $\lambda_w = 7.9\text{cm}$ ).  $\omega/\omega_c = 0.9$ ,  $\omega_p/\omega_c = 6$ ,  $z = 10\text{cm}$ .
- (b) Dispersion  $\omega$  vs.  $k_{||}$  of the spontaneous noise emission. The parallel phase velocity  $\omega/k_{||}$  is close to, but below the beam velocity.

- Fig. 12 (a) Schematic arrangement to measure the direction of wave propagation of the noise emission.
- (b) Correlation signals vs. position along the beam at different delay times  $\tau$ .
- (c) Time - position diagram for stationary phase points (circles = maxima, squares = minima) of the correlation signal. The figure shows that the parallel phase velocity points in the direction of the beam with magnitude  $|v_p| \approx (2eV_b/m_e)^{1/2}$ .

- Fig. 13 (a) Phase fronts of the spontaneously excited waves in the  $r$ - $z$  plane obtained from two-dimensional narrowband cross correlation measurements. The wave normal makes an angle  $\theta$  with respect to  $\vec{B}_0$  which is close to the oblique phase velocity resonance cone angle,  $\theta = \arccos(\omega/\omega_c)$ .
- (b) Propagation angle  $\theta$  at different frequency components  $\omega/\omega_c$ . The measurement shows that the broadband noise consists of whistlers near the oblique resonance.  $V_b = 50\text{V}$ ,  $t_s = 30\mu\text{sec}$ ,  $z = 8\text{cm}$ .

Fig. 14 Properties of small amplitude test waves excited from a point source in a beam-plasma system. An axial interferometer trace (a,b) shows a highly localized field for propagation against the beam but growing waves for propagation with the beam. A two-dimensional phase front map shows a resonance cone pattern against the beam (c) and oblique waves with the beam (d). A contour map of constant rf amplitudes (arbitrary units) shows amplitude decay along the diverging cone opposing the beam (e) but oblique amplitude growth with the beam (f). Note that for the unstable mode  $\omega/k_{||} \lesssim v_b$  and  $\vec{v}_g \sim \perp \vec{v}_p$ . Parameters:  $\omega_p/\omega_c = 3$ ,  $t_s = 10 \mu\text{sec}$ ,  $t_a = 20 \text{msec}$ ,  $V_b = 38\text{V}$ .

Fig. 15 Axial test wave interferometer traces at a fixed radial distance  $\Delta r$  from the exciter antenna at different beam energies  $eV_b$ . A continuous transition from a resonance cone pattern ( $V_b = 0$ ) to a growing single whistler mode is observed.  $t_a = 24 \text{msec}$ ,  $t_s = 30\mu\text{sec}$ .

Fig. 16 Test wave propagation near the electron plasma frequency. (a) Interferometer signal  $\phi_{rf}(z) \cos(k_{||}z)$  vs.  $z$ , showing that strong waves are only excited in the presence and direction of the beam. (b) Two-dimensional phase front map (maxima of interferometer signals). Although the exciter is a point source plane waves along the beam are excited which are the most unstable modes of the beam-plasma system leading to beam and background plasma heating.

Gas, pressure	Krypton, $2.5 \times 10^{-4}$ Torr
Background plasma density	$n_e = 10^9$ to $10^{10}$ $\text{cm}^{-3}$
Electron temperature	$kT_e = 2$ eV
Magnetic Field	$B_0 = 75$ G
Ratio of plasma to cyclotron frequency	$1 < \omega_p / \omega_c < 6$
Electron - neutral collision frequency	
(i) Absolute	$\nu_{en} = 4 \times 10^5$ $\text{sec}^{-1}$
(ii) Normalized	$\nu_{en} / \omega_c = 3 \times 10^{-4}$
Electron mean free path	$\lambda_e = 200$ cm
Electron beam energy	$eV_b = 0$ to $50$ eV
Normalized beam density	$n_b / n_e = 1\%$
Beam temperature	$kT_b = 0.5$ to $8$ eV
Beam electron mean free path for	
(i) elastic collisions	$\lambda_b = 90$ cm
(ii) ionizing collisions	$\lambda_b^i = 300$ cm

Table 1 Basic parameters of beam and background plasma.

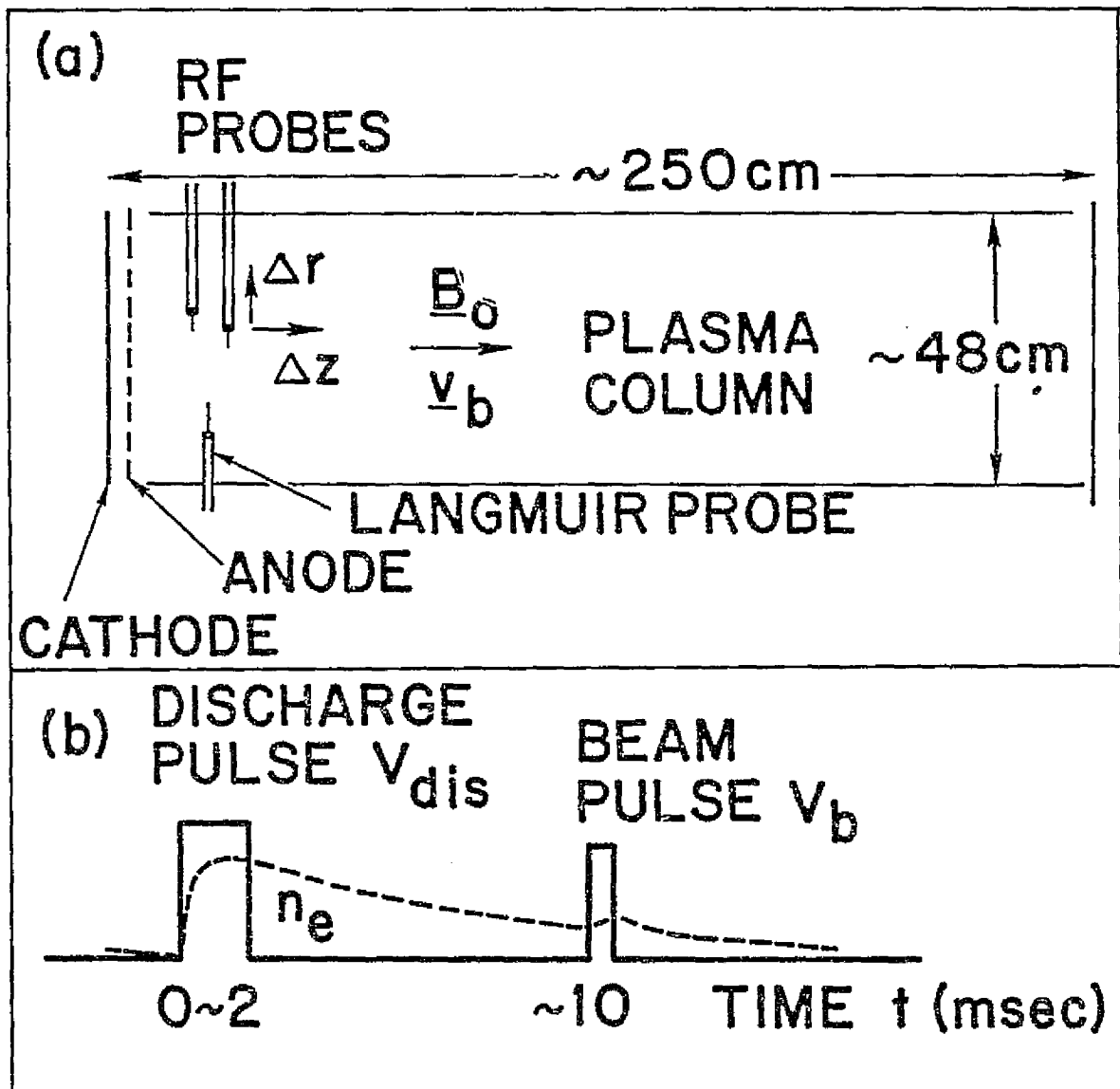


Figure 1

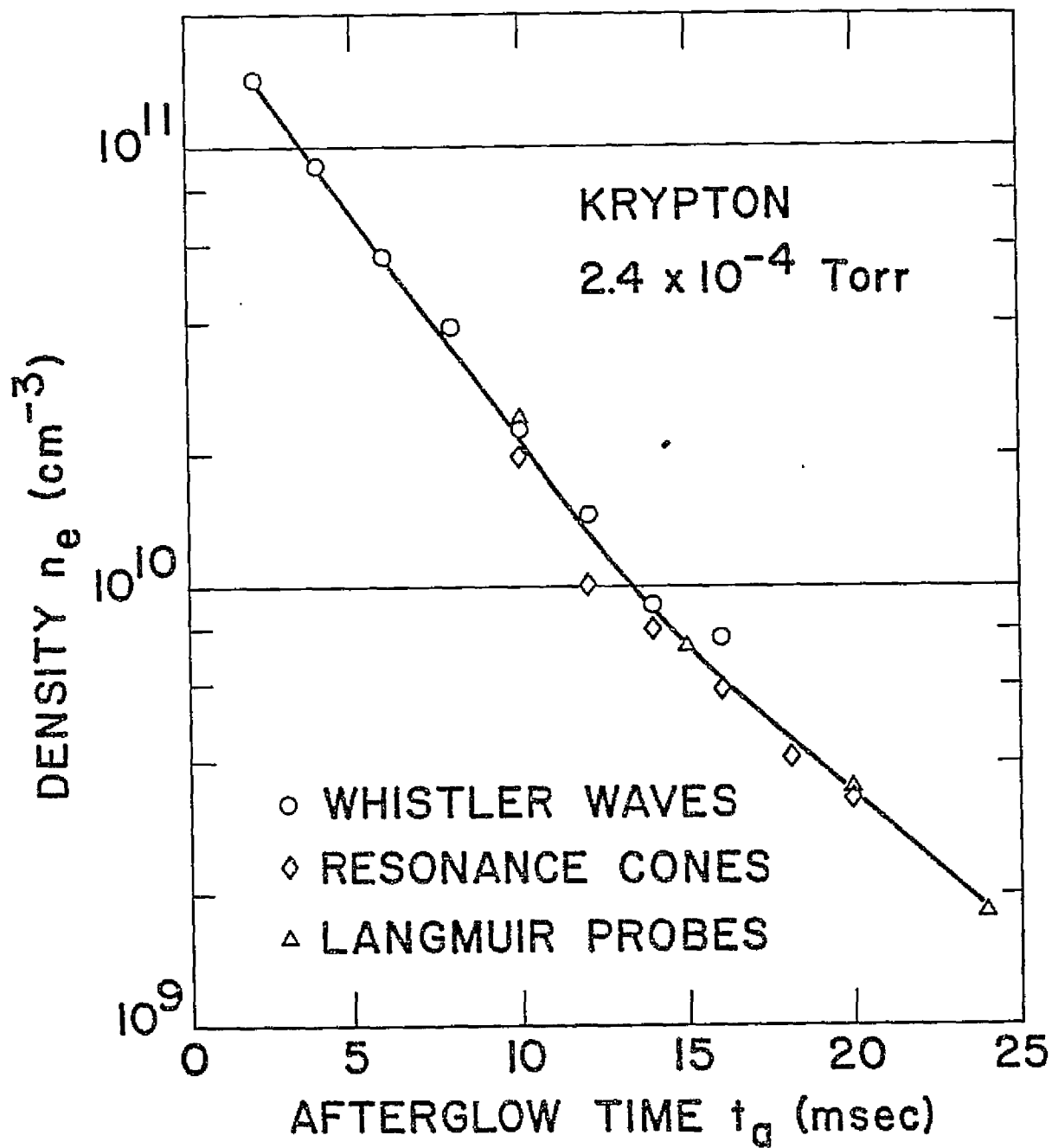


Figure 2

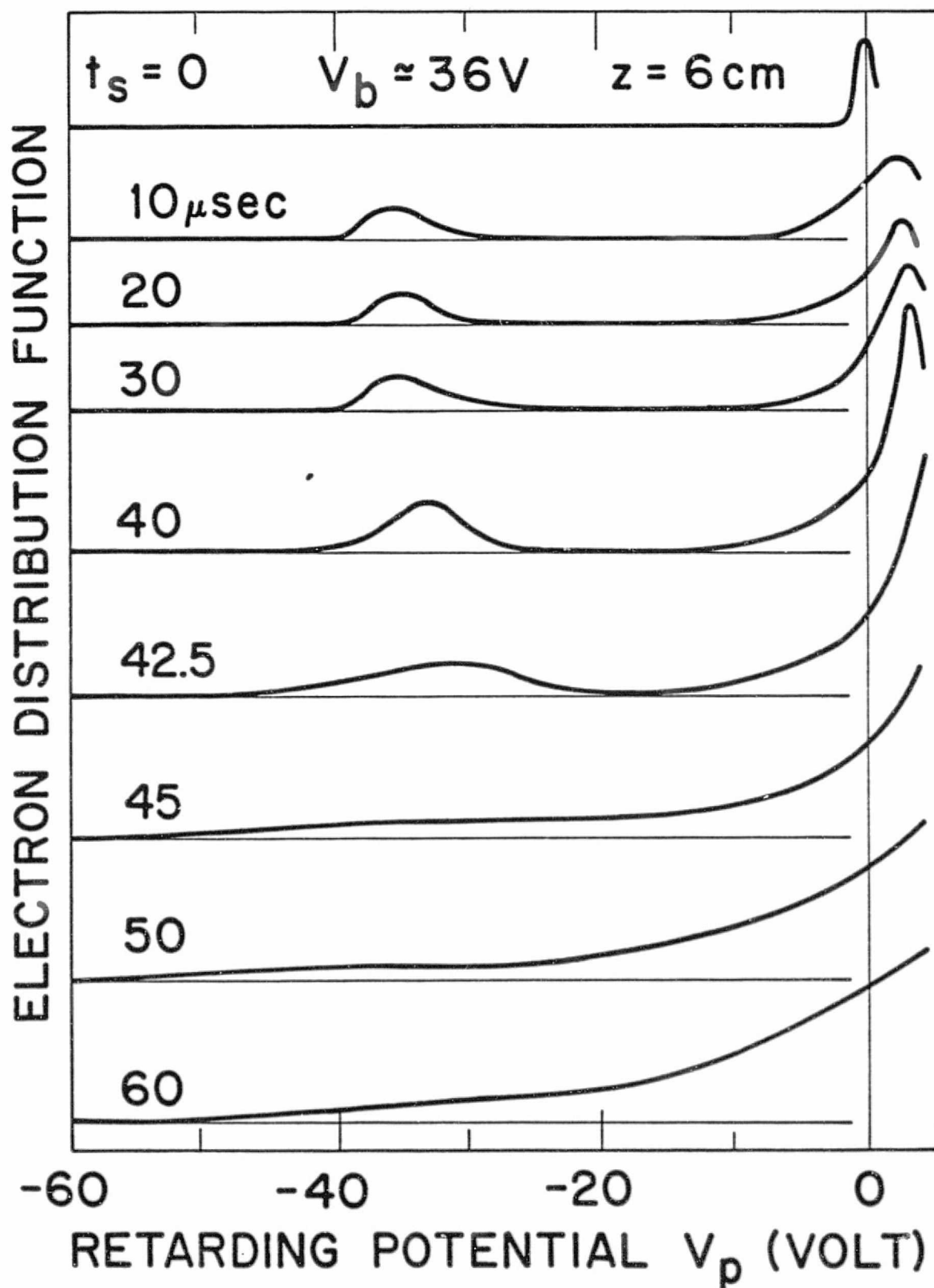


FIGURE 3

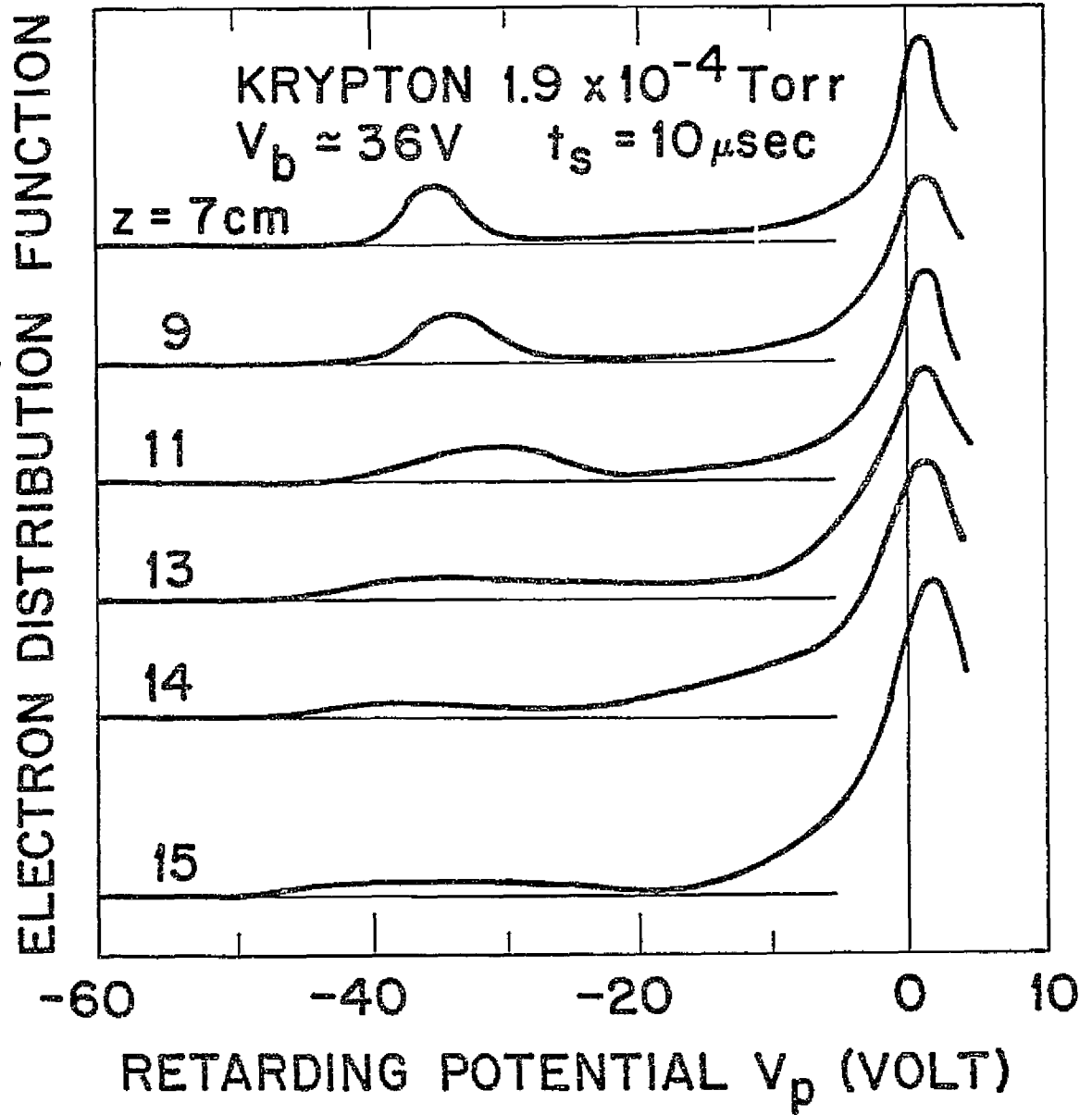


FIGURE 4

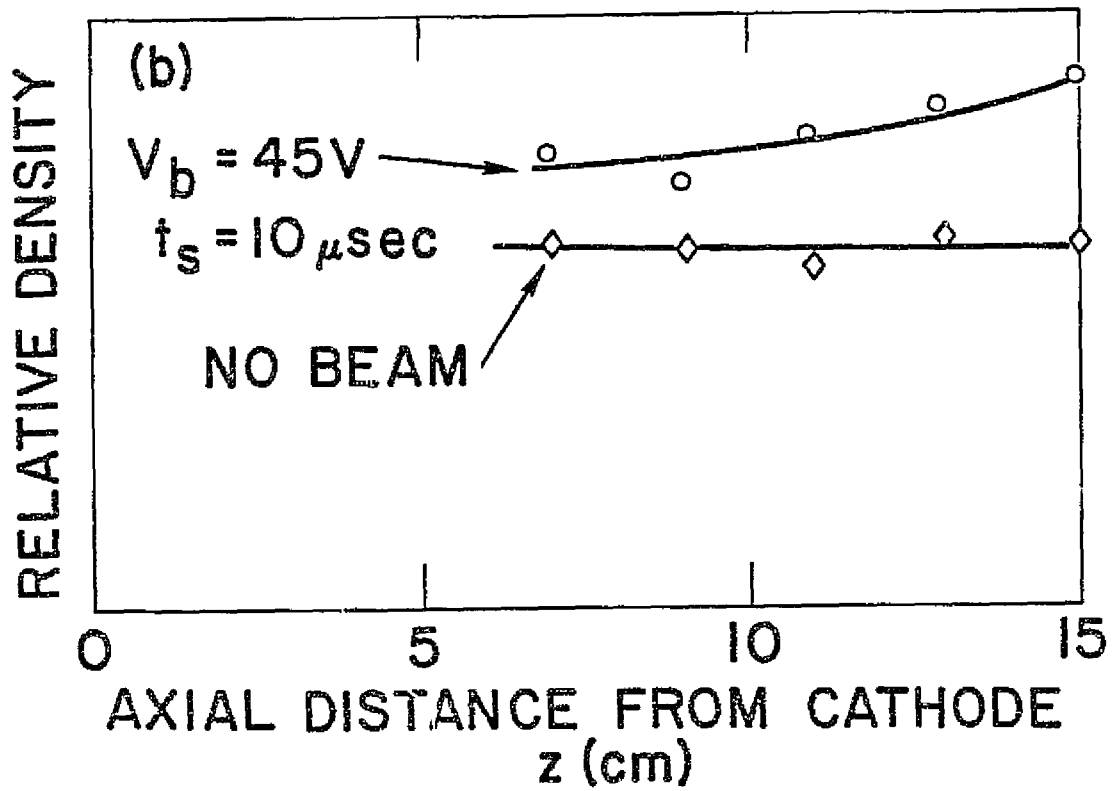
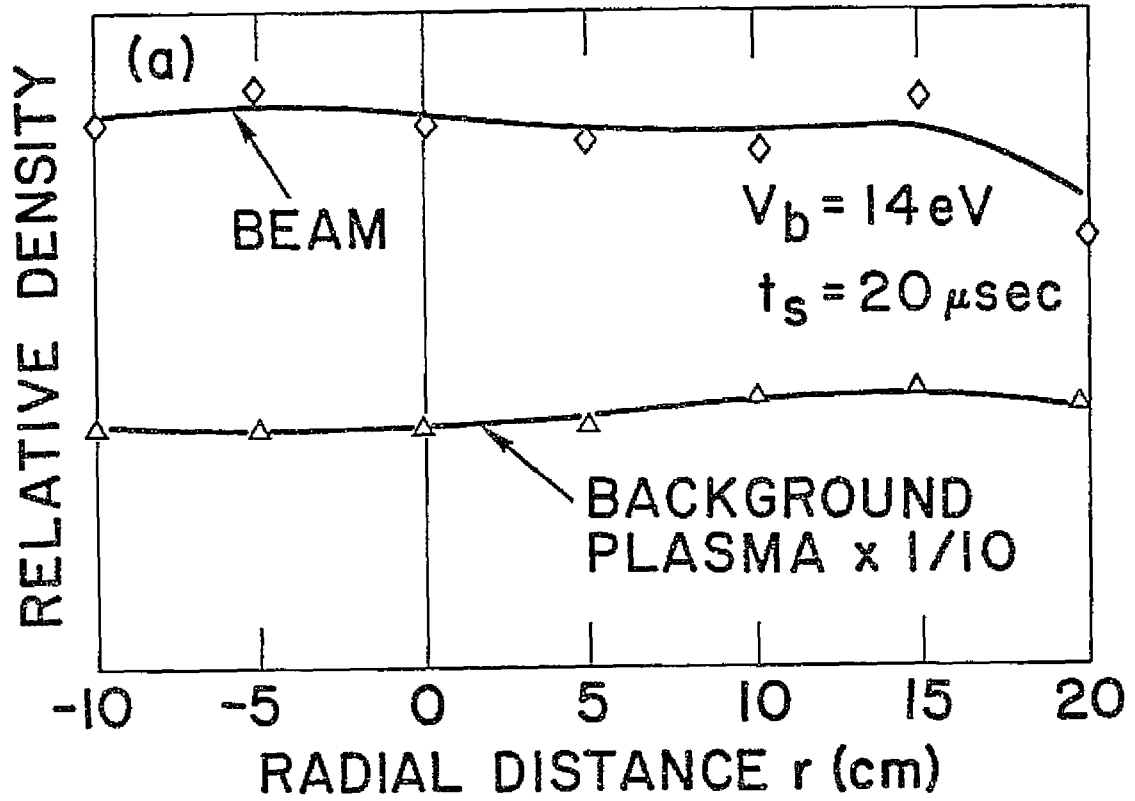


Figure 5

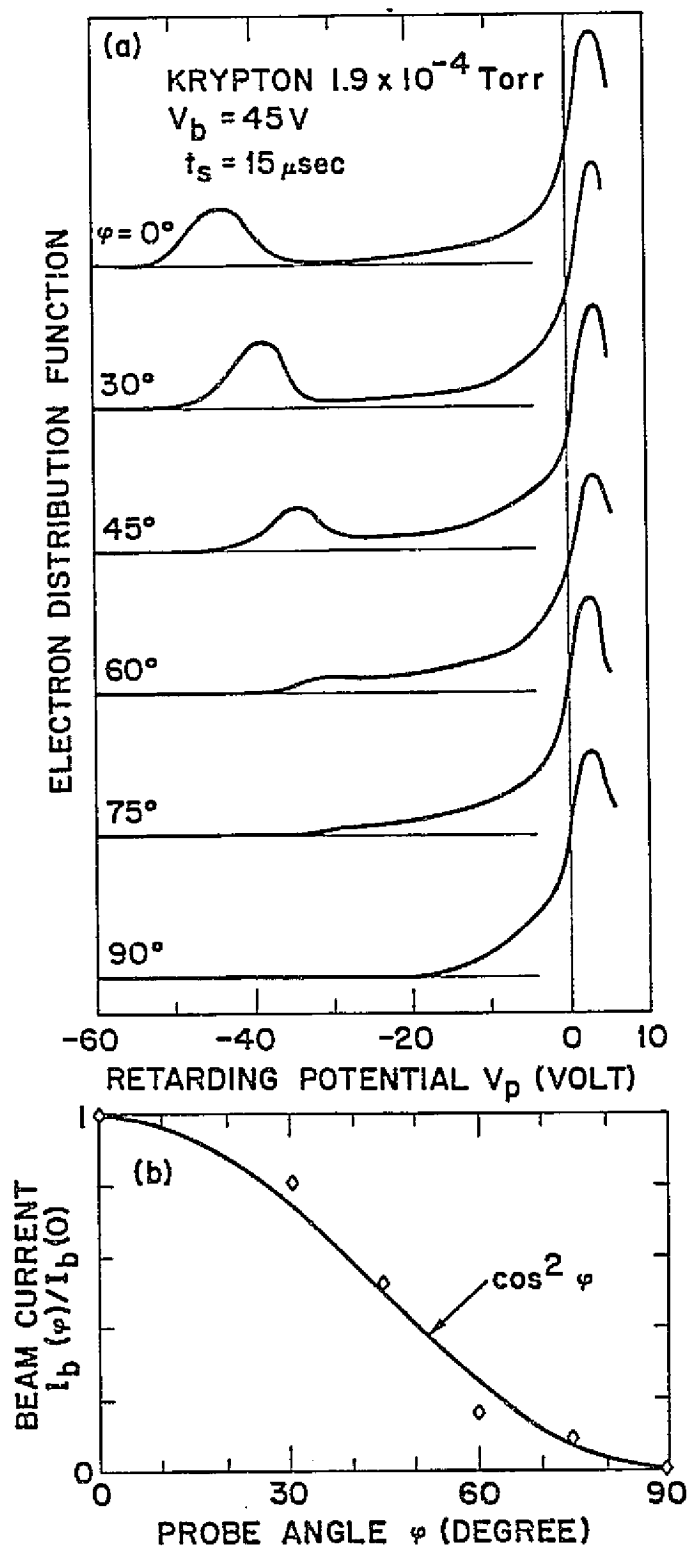


FIGURE 6

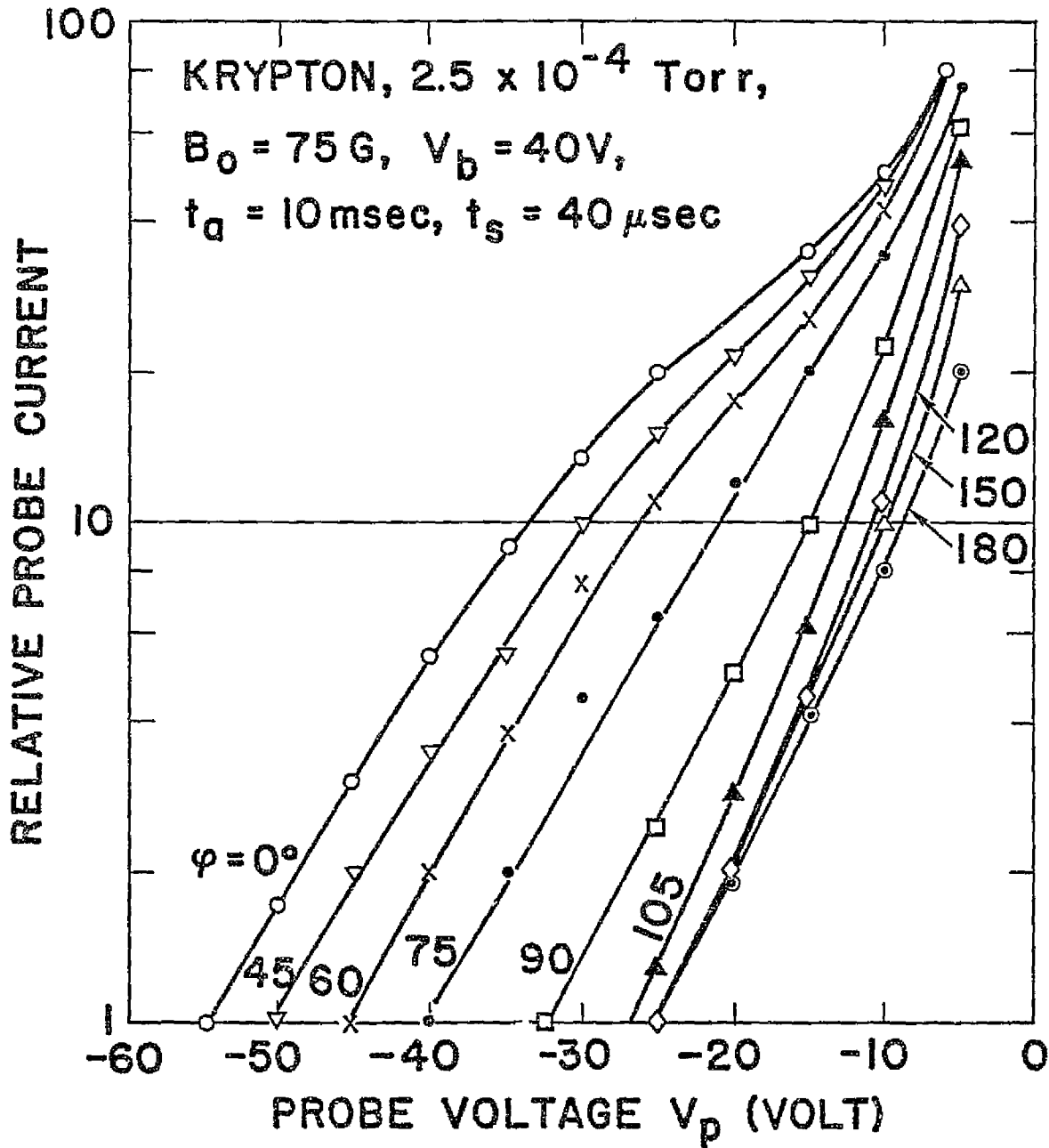


Figure 7

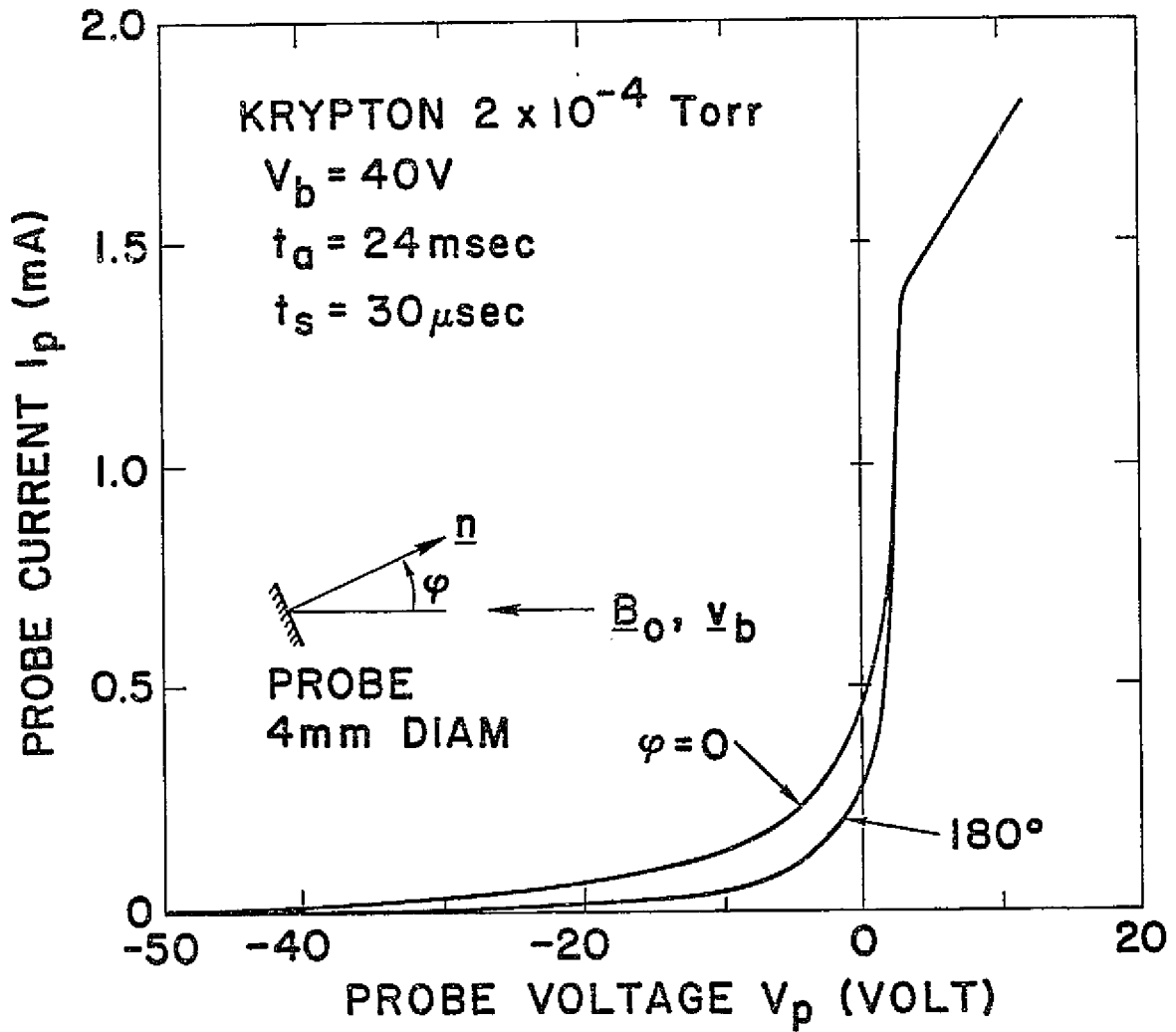


FIGURE 8

ORIGINAL PAGE IS  
OF POOR QUALITY

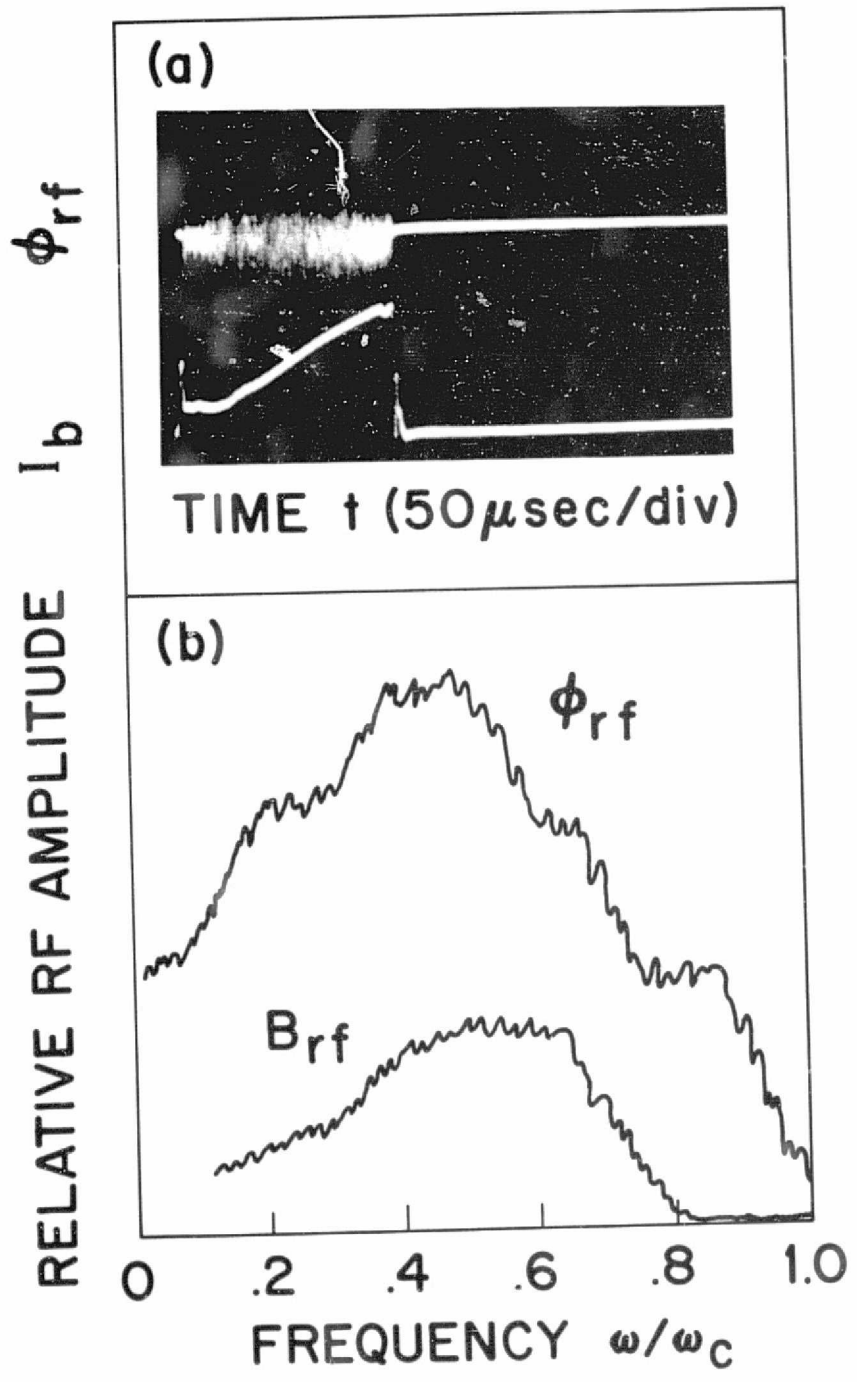


Figure 9

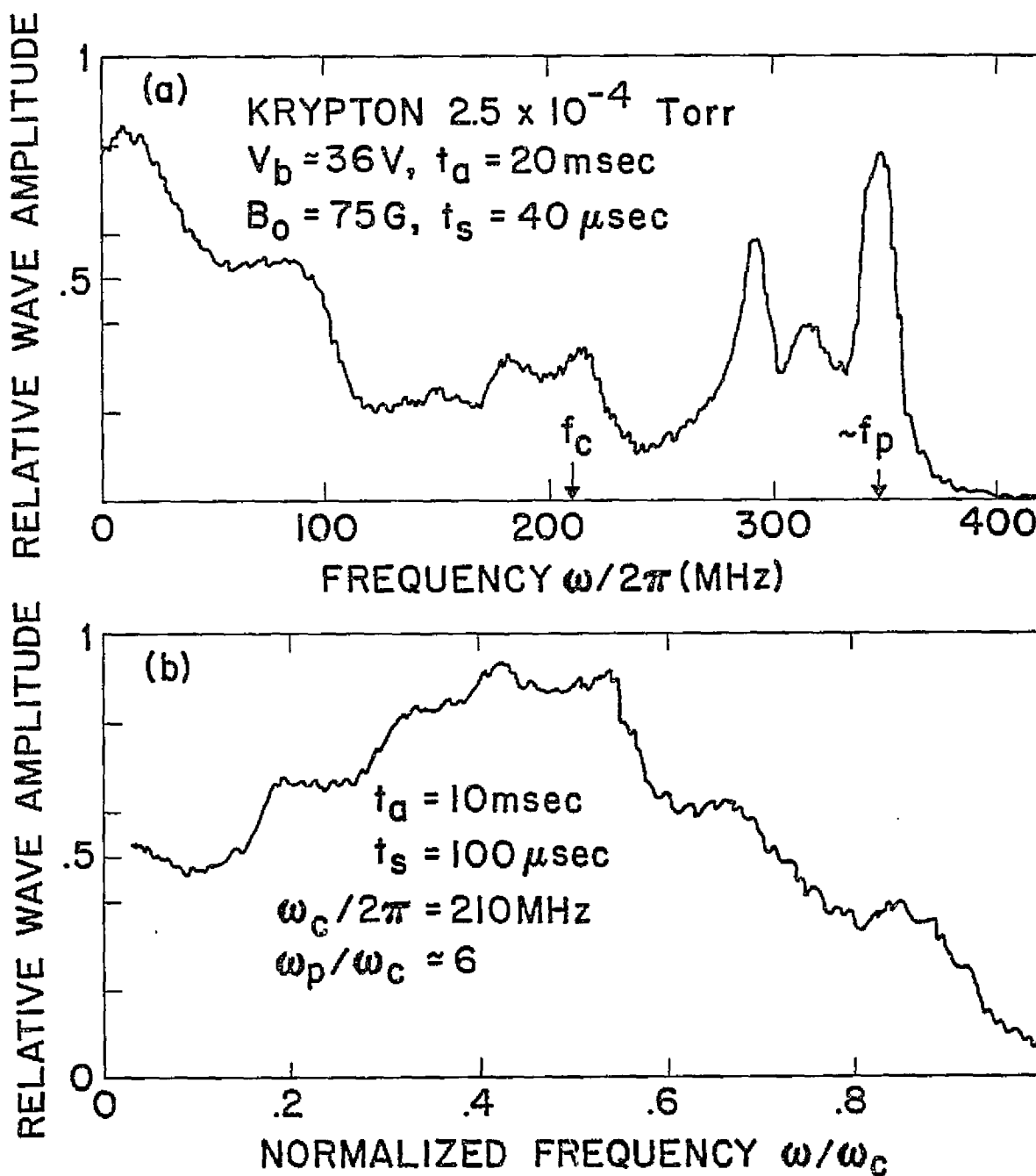


Figure 10

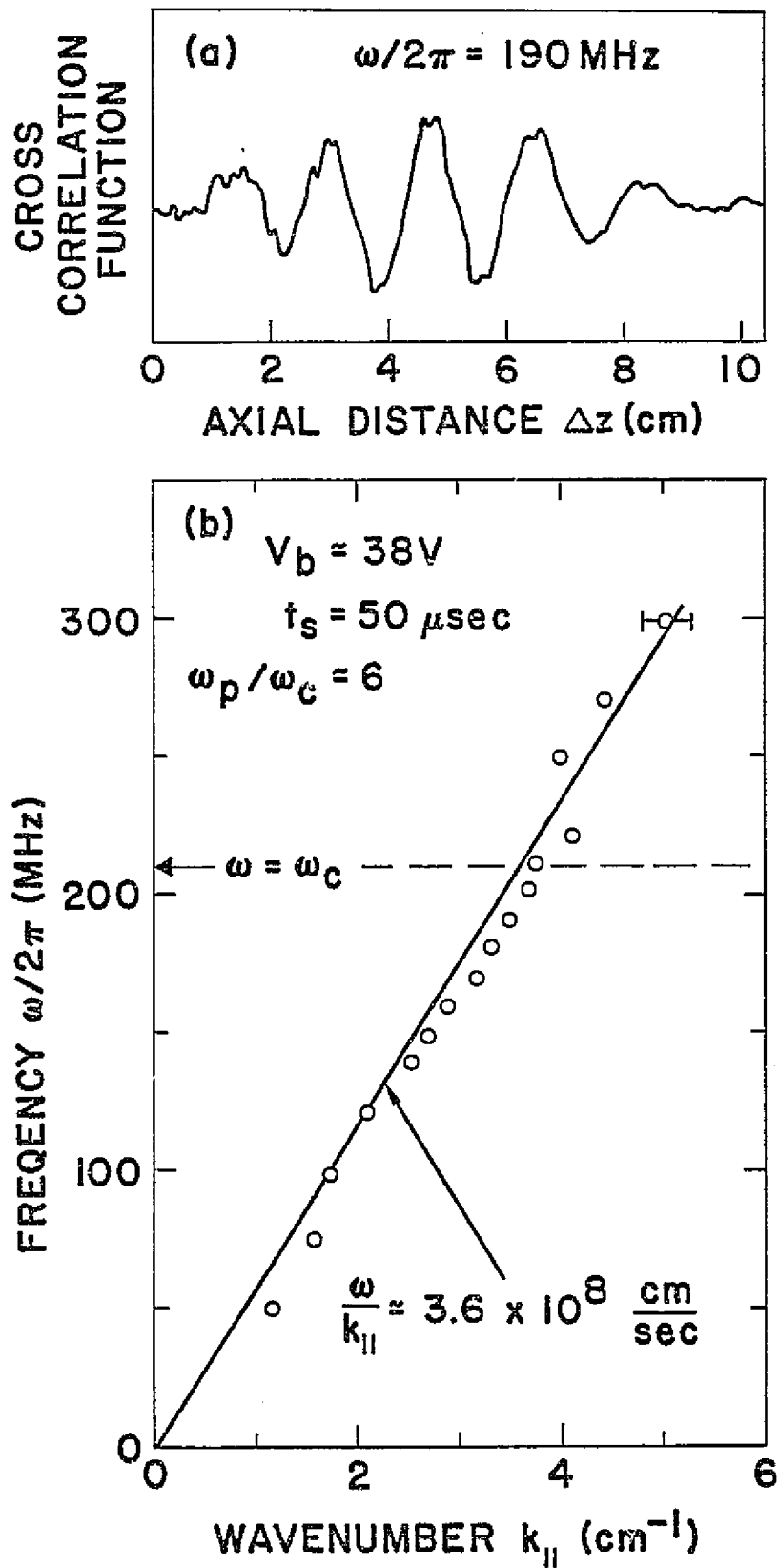


Figure 11

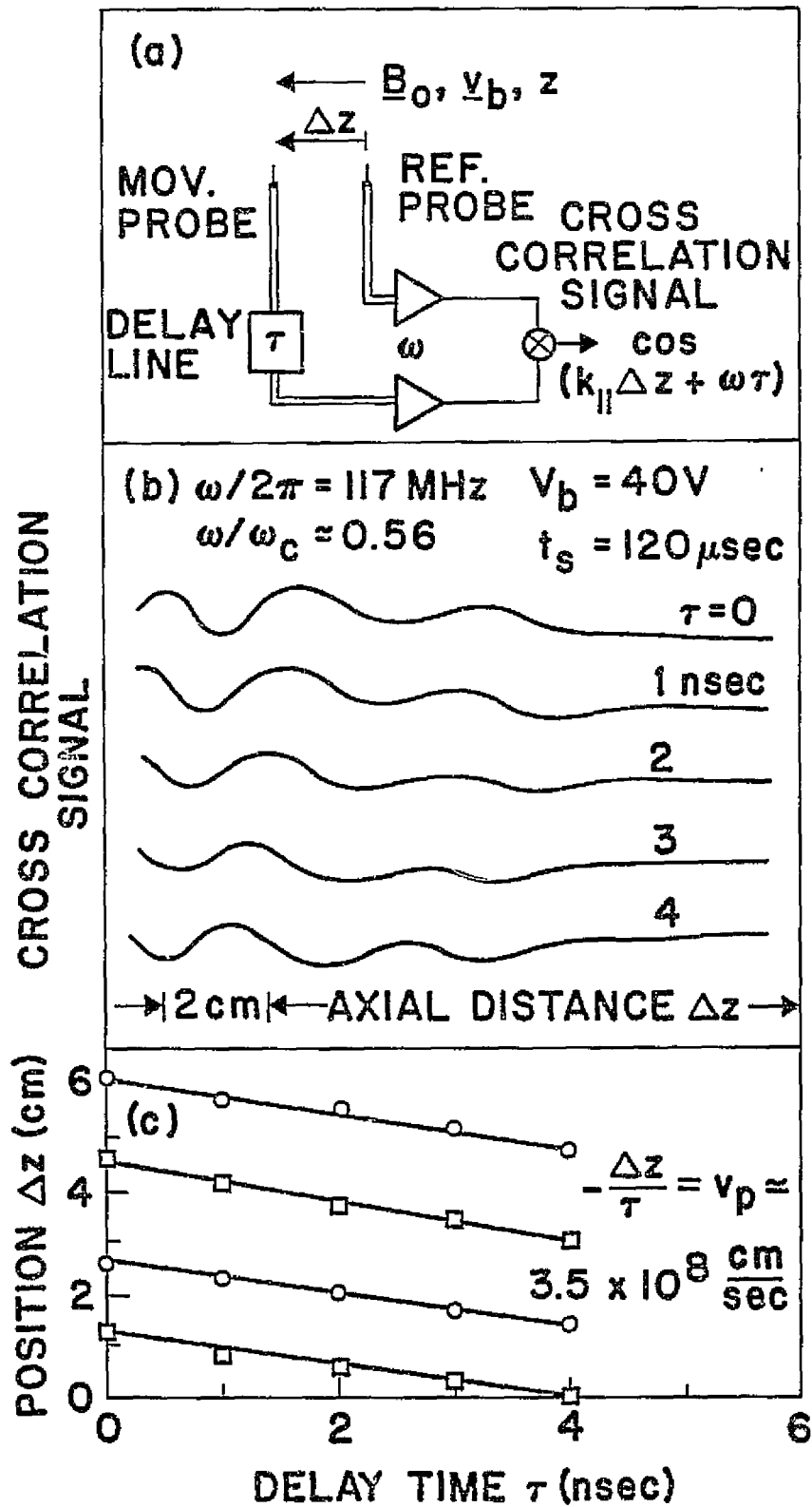


Figure 12

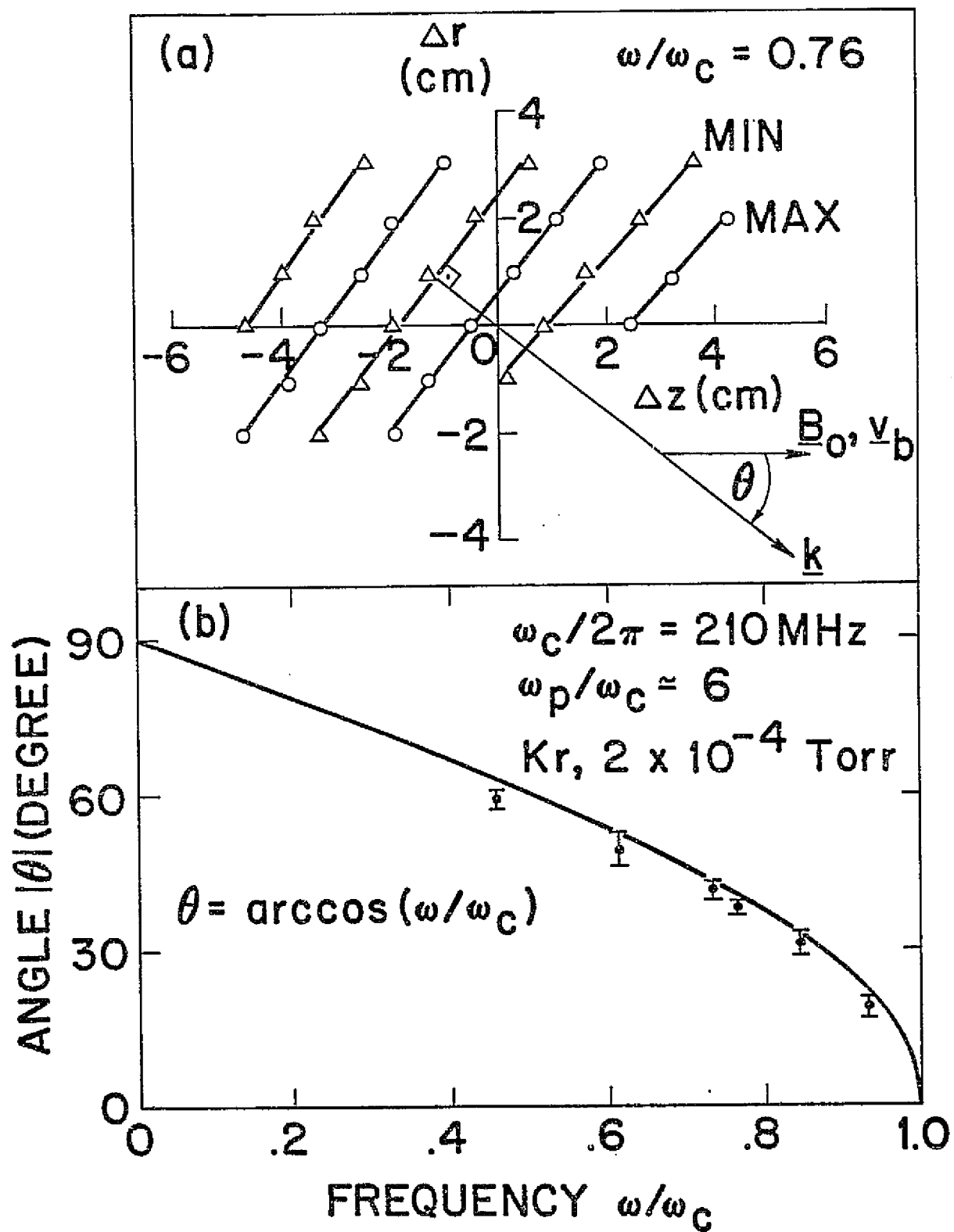


Figure 13

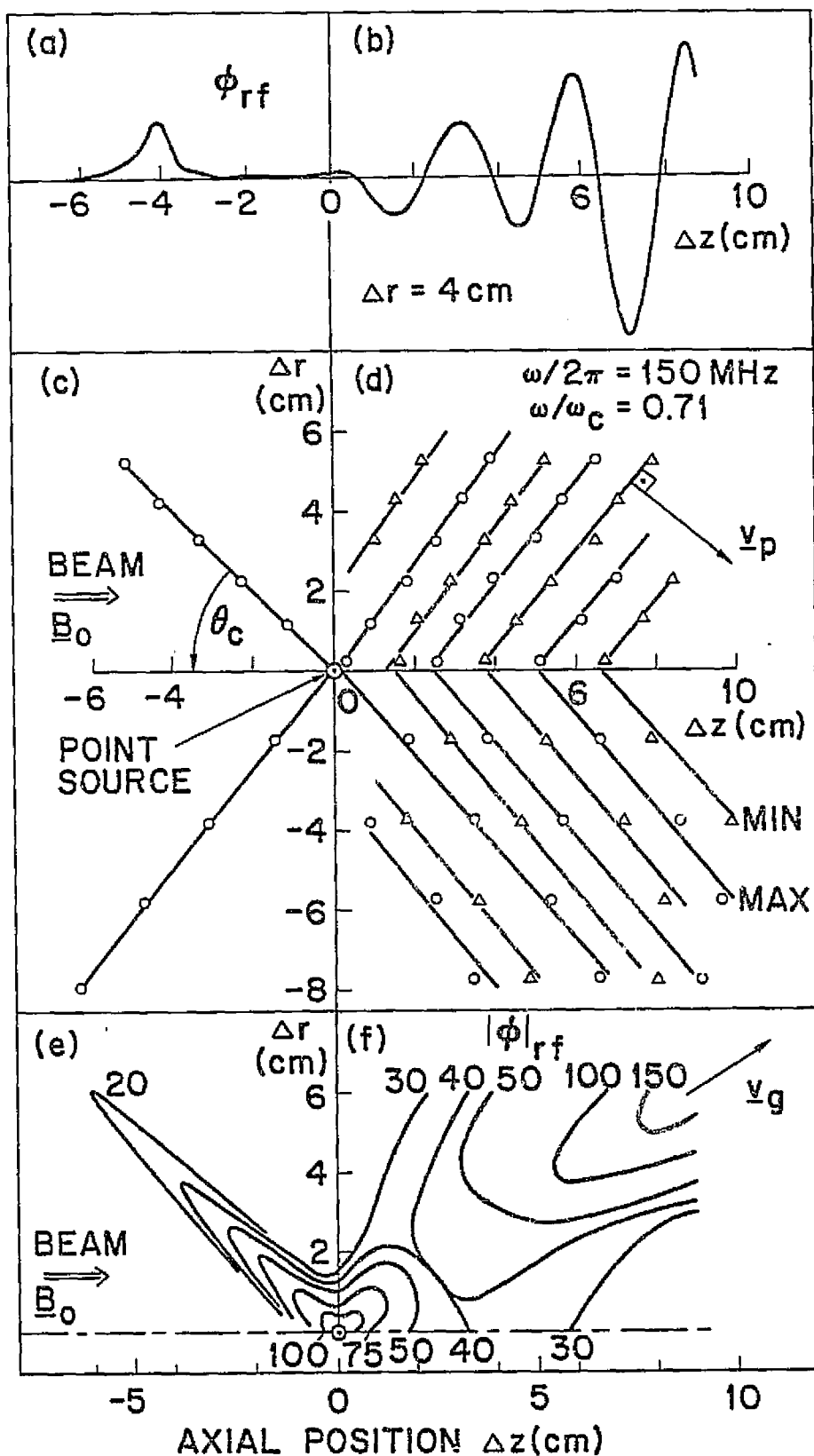


Figure 14

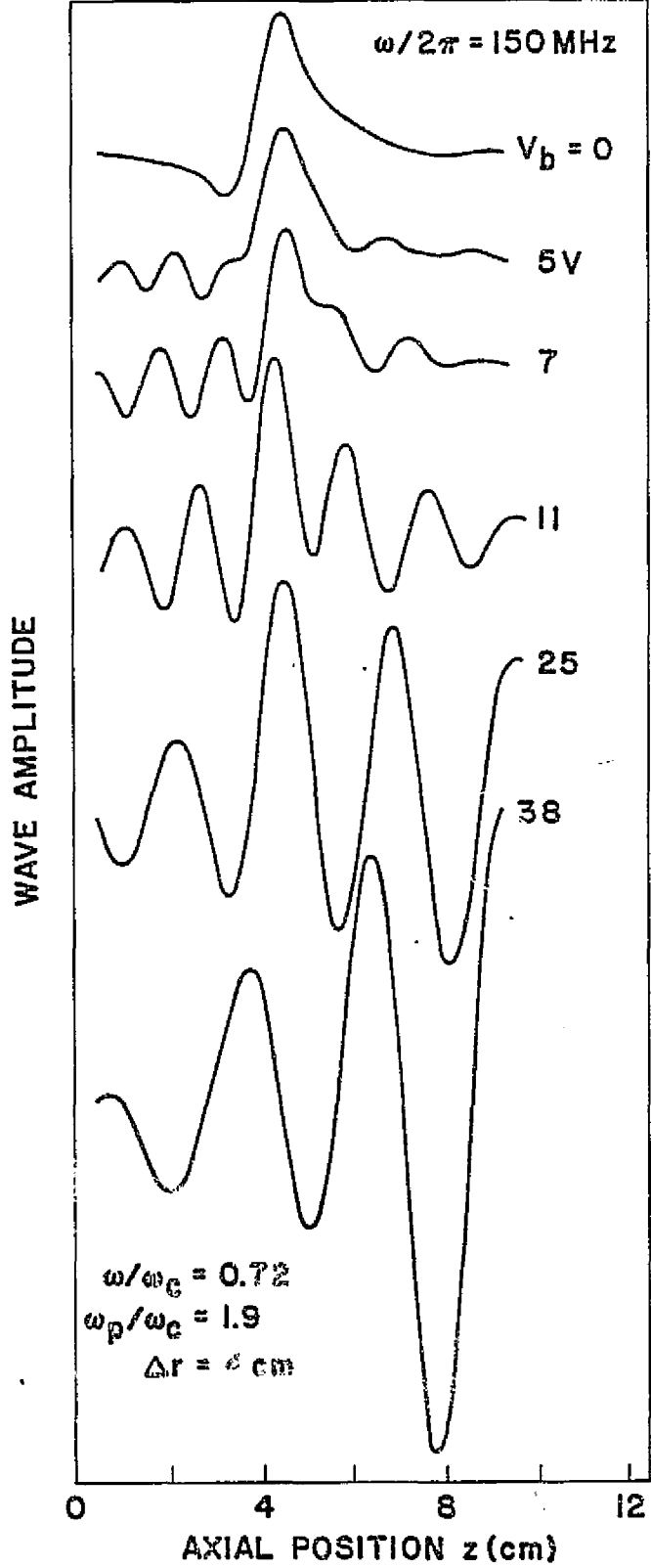


Figure 15

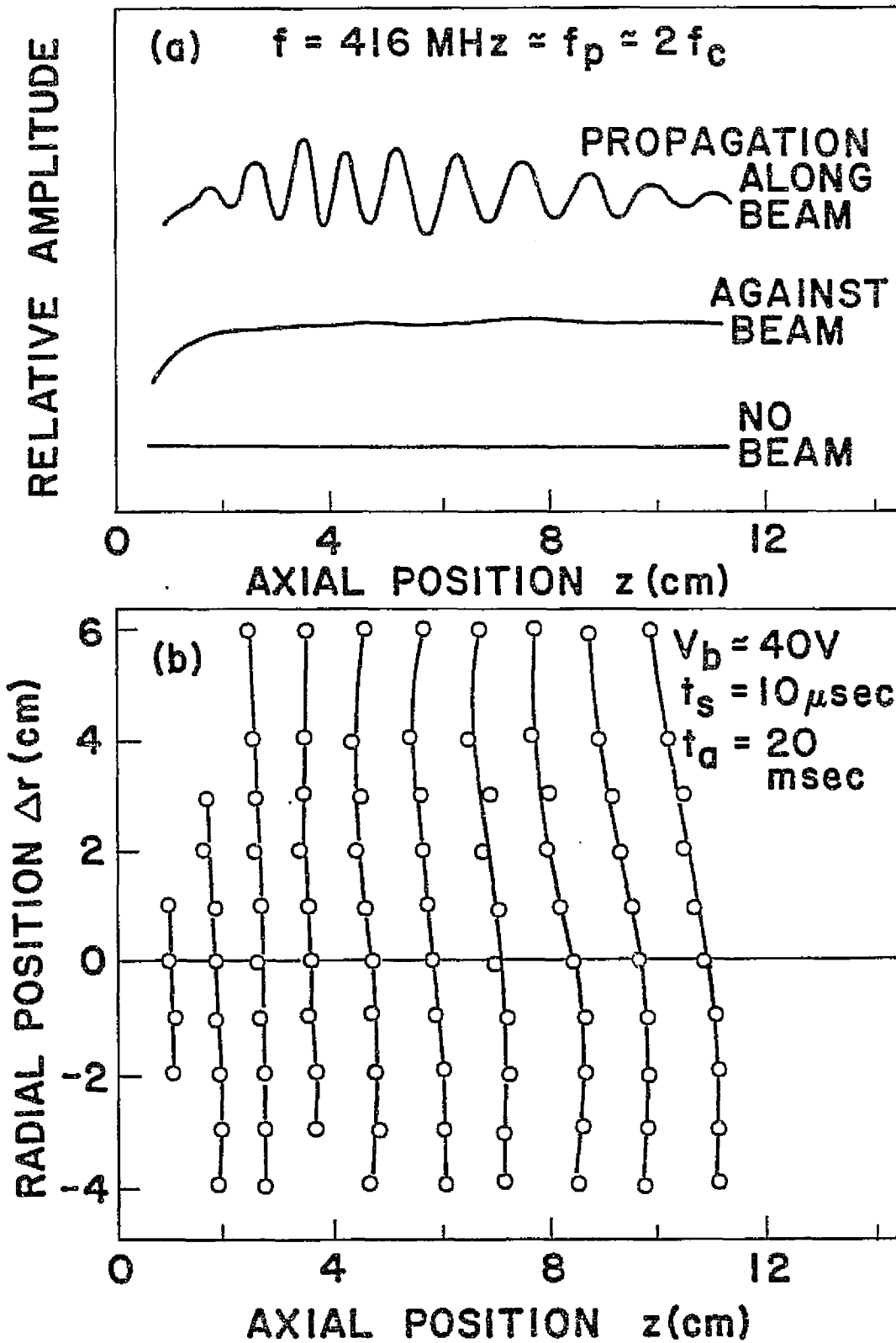


Figure 16

N77-27260

## EXPERIMENTS ON CURRENT-DRIVEN THREE-DIMENSIONAL ION SOUND TURBULENCE

## PART I. RETURN-CURRENT LIMITED ELECTRON BEAM INJECTION

R.L. Stenzel\*

TRW Systems, Redondo Beach, CA 90278

ABSTRACT

The injection of an electron beam into a weakly collisional, magnetized background plasma is investigated experimentally. The injected beam is energetic (40 eV) and cold ( $\leq 0.5$  eV), the background plasma ( $n_e \geq 10^9$  cm<sup>-3</sup>,  $\omega_p > \omega_c$ ) is initially isothermal ( $kT_e = kT_i = 0.2$  eV). Beam and plasma dimensions are so large ( $\sim 43$  cm diam, 250 cm length, Debye length  $\lambda_D \leq 0.02$  cm) that the system can be considered unbounded. The temporal and spatial evolution of the beam-plasma system is dominated by collective effects. High-frequency electrostatic instabilities ( $\omega = \omega_p$ ) rapidly thermalize the beam and heat the background electrons ( $kT_e \gg kT_i$ ). The injected beam current is balanced by a return current consisting of background electrons drifting toward the beam source. The drift between electrons and ions [ $(kT_e/m_i)^{1/2} \ll v_d < (kT_e/m_e)^{1/2}$ ] gives rise to an ion acoustic instability which develops into strong three-dimensional turbulence to be discussed in a companion paper. It is shown that the injected beam current is limited by the return current which is approximately given by the electron saturation current. Non-Maxwellian electron distribution functions are observed.

## I. INTRODUCTION

The injection of an electron beam into a stationary background plasma is a problem of general interest. Such situations arise, for example, in space plasmas (aurora), in laboratory plasmas (dc discharges) and in fusion type plasmas (relativistic E-beams). While collision dominated systems have been analyzed for many years in glow discharges<sup>1</sup> collisionless beam-plasma interactions are presently of main interest. Particular interest has been given to high frequency electrostatic beam-plasma instabilities near the electron plasma frequency  $\omega_p$  which are effective in randomizing an initially cold, energetic electron beam.<sup>2,3</sup> The current closure in such a system is an important problem which has been given less attention in small laboratory devices than in unbounded media.<sup>4</sup> However, with the development of larger laboratory plasmas the return current problem has to be considered as an integral part of beam injection experiments. In the present investigation, it will be shown that the return current gives rise to strong low frequency electrostatic instabilities at frequencies up to the ion plasma frequency  $\omega_{pi}$ . Ion sound turbulence is effective in scattering background electrons which carry the current. Thus, the instabilities provide resistance to both the injected beam current and the return current.

The present paper describes the properties of the electron beam and background plasma whereas the instability analysis and wave dynamics are given in a companion paper<sup>6</sup>. The experimental arrangement is kept as simple as possible so that the current flow can be readily accounted for. An electron beam is extracted from a uniformly emissive, large diameter (43 cm) cathode and closely spaced ( $\sim 1$  cm) highly transparent (71%) anode. The beam is injected along a uniform magnetic field ( $B_0 = 75G$ ) into a quiescent after-glow plasma of comparable diameter produced by the beam source previously.

The plasma is not in contact with the chamber walls except at the floating end section. Net current flows only between the closely spaced anode and cathode. The beam current injected through the gridded anode is balanced by a return current drawn from the background plasma. The incident beam is not reflected but scattered in velocity space even before reaching the end of the device. It is shown that the return current and thereby the injected beam current are essentially limited to the electron saturation current drawn by the anode from the heated background plasma. The strong current flow changes the electron distribution function. Skewed, shifted electron distributions are observed.

The first part of the paper gives a description of the experimental setup and techniques. In Section II, the beam and plasma properties are presented and discussed. A brief summary of the observations is given in Section III since further results are presented in Ref. 6.

## II. EXPERIMENTAL ARRANGEMENT AND MEASUREMENT TECHNIQUES

The experiment is performed in a large diameter, uniform, weakly collisional magnetoplasma. The device (Fig. 1) which has been described previously in connection with whistler wave experiments,<sup>7-9</sup> consists briefly of a low pressure ( $2 \times 10^{-4}$  Torr krypton) dc discharge between a solid, oxide-coated cathode of 43 cm in diameter and closely spaced ( $\sim 1$ cm), highly transparent (71%) mesh anode. The plasma is confined by a uniform axial magnetic field ( $B_0 = 75$ G) and terminated after 2.5 m by a floating permanent magnet end wall.<sup>10</sup> The plasma is not in contact with the side chamber walls. As shown in Fig. 2, the discharge is pulsed repetitively

( $t_r = 25$  msec). The first discharge pulse produces an afterglow background plasma ( $10^9 < n_e < 10^{11}$  cm<sup>-3</sup>,  $kT_e = kT_i = 0.25$  eV). At a desired afterglow time ( $t_a = 20$  msec) a second independent beam voltage pulse is applied to the cathode and the electron beam is formed by accelerating electrons in the cathode-plasma sheath of several Debye lengths in thickness ( $\leq 2$  mm). The highly transparent anode is well outside the sheath. The plasma potential is close to that of the grounded anode since the dominant electron loss is at the anode. All measurements are sampled so that one can observe the temporal evolution of the beam-plasma system. Spatial information is obtained from a variety of movable probes shown in Fig. 1. Plane, one-sided Langmuir probes are located at the anode (No. 1), at  $z = 7$  cm from the cathode (No. 2), in the middle of the device (No. 3) and on an axially movable shaft (No. 4). Two pairs of small cylindrical Langmuir probes (0.1 mm diam x 2.5 mm length) movable in orthogonal planes are used to detect and/or excite ion acoustic waves. An array probe<sup>6</sup> is employed for multichannel simultaneous fluctuation measurements. There are additional high-frequency probes (not shown in Fig. 1) which are used to excite whistler waves, electron Bernstein and Landau waves for diagnostic purpose.

### III. EXPERIMENTAL RESULTS

First, the background plasma properties are analyzed. Fig. 3 shows the density vs. afterglow time. At high densities ( $\omega_p \gg \omega_c$ ) the absolute value of  $n_e$  is reliably found from whistler wave dispersion measurements.<sup>8,11</sup> In the range  $\omega_p \approx \omega_c$  resonance cones are useful for density diagnostics.<sup>12,13</sup> Although cylindrical Langmuir probes are reliable for relative density measurements an absolute density determination from orbital motion theory<sup>14</sup>

leads to uncertainties since the ion temperature is not accurately known. The ion saturation current is thus "calibrated" by absolute density values derived from wave dispersion measurements for electron plasma waves [Fig. 4(a)] and electron cyclotron harmonic waves [Fig. 4(b)]. The observed density decay is due to ambipolar diffusion along  $\vec{B}_0$  and surface recombination at anode, cathode and floating end wall.

The electron temperature decays from  $kT_e = 2$  eV during the discharge to  $kT_e = 0.2$  eV in the late afterglow ( $t_a \geq 15$  msec). From the damping of ion acoustic waves the ion temperature is estimated to be  $kT_i \leq 0.2$  eV. Further parameters of the background plasma are summarized in Table 1.

The beam voltage pulse is applied at an afterglow time  $t_a$  which determines the desired background plasma density. After injection beam and background plasma strongly interact and change their initial properties to new steady-state values. Fig. 5 shows Langmuir probe (No. 2) traces prior to beam injection (top) and at  $t_s = 10$   $\mu$ sec after turn-on of the beam pulse (bottom). Prior to beam injection, there is essentially no difference in the traces with the probe normal pointing toward the cathode ( $\phi = 0$ ) or in the opposite direction. After injection, the energetic beam electrons ( $V_b \approx 46$ V) are observed for  $\phi = 0$  but not for  $\phi = 180^\circ$ , indicating that there are no reflected beam electrons. The background electron flux (total current minus beam current for  $\phi = 0$ ) is about twice as large toward the anode ( $\phi = 180^\circ$ ) than in the direction of beam injection where beam and background saturation currents are approximately equal. Thus the background plasma carries a return current equal to the injected current. The total saturation currents for  $\phi = 0$  and  $\phi = 180^\circ$  are equal, i.e. the plasma is free of a net current, consistent with the fact that the applied current flows only within the narrow cathode-anode gap.

A closer inspection of the traces reveals first that the saturation current ("knee") for  $\phi = 180^\circ$  occurs at a lower potential than for  $\phi = 0^\circ$  which is characteristic for a drift in the background plasma. Second, the electron "temperature" for  $\phi = 180^\circ$  is about twice as large as for  $\phi = 0^\circ$ , which indicates drift and possible asymmetry in the distribution function. By differentiating the plane probe characteristics and displaying  $dI_p/dV_p$  vs. velocity, the parallel electron distribution function is obtained (Fig. 6). It shows the cold fast beam and the skewed, slightly shifted background distribution.

The drift velocity measurement from Langmuir probe traces is unfortunately not very accurate. One can only estimate that the drift velocity exceeds sound speed ( $c_s = 2.3 \times 10^5$  cm/sec) by one to two orders of magnitude yet the drift is about one order of magnitude smaller than the electron thermal velocity ( $v_e = 1.4 \times 10^8$  cm/sec). Conventionally, the drift velocity is determined from the electron flux and density ( $j = nev_d$ ). The density is well known ( $n_e = 2 \times 10^9$  cm<sup>-3</sup> at  $t_a = 24$  msec), the electron flux ( $j = 3$  mA/cm<sup>2</sup>) is calculated from the measured cathode current (6A), surface area (1450 cm<sup>2</sup>) and anode transparency (71 %). The calculated drift velocity is  $v_d = 0.94 \times 10^7$  cm/sec ( $\approx 40 c_s = .08 v_e$ ). However, only if the distribution remains Maxwellian the drift corresponds to an actual shift in the distribution function. In the present case, the current is partly carried by the anisotropy in the distribution and partly by an actual displacement of the distribution function maximum relative to the essentially stationary ion distribution. Only the shift is relevant for the ion acoustic instability. Since  $v_d \gg c_s$  the threshold for the instability is well exceeded. The anisotropy could arise from the fact that the anode which draws electron saturation current (see Fig. 9) represents an absorbing boundary for electrons. Electrons heated by beam-plasma interactions in the interior of the plasma stream toward the anode and

only a fraction ( $\sim 50\%$ ) is reflected by the anode-cathode boundary. If the anode transparency were reduced, the distribution would approach a half-Maxwellian. The classical scale length for Maxwellization<sup>15</sup> ( $\lambda = v_e/v_{ee} \sim 3 \times 10^3$  cm) is large compared to the present distance of observation from the anode.

The spatial properties of beam and background plasma have been investigated. Across the magnetic field beam and plasma parameters are uniform to within 10% over a distance of approx. 35 cm.<sup>8,17</sup> Along  $B_0^z$ , the beam-plasma system changes on a scale length short compared to the collision mean free path. Fig. 7 shows Langmuir probe (No. 4;  $\phi = 0$ ) traces for different axial positions  $z$  from the cathode sampled at a fixed time  $t_s$  after beam injection. With increasing distance of propagation the beam broadens and the background electron temperature and density increase. This rapid scattering of the beam is well known to be caused by electrostatic instabilities.<sup>16</sup> Although in an unbounded system a wide range of oblique whistlers<sup>17</sup> and Bernstein waves are unstable, the mode with the shortest growth length is that near the electron plasma frequency. For a cold beam plasma interaction the predicted maximum spatial growth rate is given by<sup>18</sup>

$$\frac{k_i}{k_r} = \frac{3^{1/2}}{2} \left( \frac{n_b}{6 n_e} \right)^{1/3} \left( \frac{v_b}{v_e} \right)^{2/3}, \quad (1)$$

where  $n_b/n_e$  and  $v_b/v_e$  are the ratio of beam to background plasma density and directed beam velocity to background electron thermal velocity, respectively. With the experimental conditions ( $n_b/n_e = 5.8 \times 10^{-2}$ ,  $v_b/v_e = 3.2$ ,  $k_r = 6.3 \text{ cm}^{-1}$ ) the theoretical growth length is  $k_i^{-1} = 0.4$  cm. The beam distribution is observed to change after approx. 10 wavelengths or 25 e-folding lengths from the injection point. The beam broadens, forms a plateau and finally, for  $z \geq 20$  cm, forms a tail of a distribution with

continuously decreasing slope,  $\partial f_e / \partial v_{||} < 0$ . This stable distribution is evident in Fig. 8 which shows probe (No. 3) traces in the middle of the device ( $z = 125$  cm). Although the fast particle flux is still different for  $\phi = 0$  and  $\phi = 180^\circ$ , its magnitude is small compared to the background electron saturation current. The drift in the background distribution is not observable within measurement accuracy. The beam electrons have transferred most of their energy to plasma waves which, via Landau damping heat the background electrons. Since the anode is a strong energy sink, a steady-state temperature is established. At the far end of the device ( $z = 250$  cm), the asymmetry in the energetic electron flux amounts to only a few percent of the total electron flux. Reflections of energetic electrons thus play an insignificant role in the current balance. Corresponding to the axial gradient of the injected beam current there is a gradient in the return current. When the end plate instead of the grid is used as an anode, the discharge current is also limited to the background electron saturation current. However, this mode of operation is avoided because it exhibits two undesirable features. First, the discharge cannot be initiated at normal discharge voltages ( $V_d = 40$  V). Second, after the discharge has been triggered, the current exhibits large amplitude ( $\delta I/I \approx 75\%$ ) low frequency ( $f \sim 1$  kHz) fluctuations. The peak anode current is comparable to the value for the gridded anode which is free of fluctuations.

The temporal behavior of the beam-plasma system has been investigated next. Figure 9 shows Langmuir probe (No. 1) traces at different times before, during and after beam injection. The probe traces exhibit the background plasma properties at the anode ( $\phi = 180^\circ$ ,  $z = 0$ ). Prior to beam injection, the plasma potential has a small positive value consistent with the low temperature of the afterglow plasma. During beam injection,

the knee in the probe trace occurs at a negative potential with respect to the grounded anode. Thus, the anode draws a current in excess of the electron saturation current from the background plasma. A comparison between Figure 9 and Figures 5 or 7 indicates that the knee in the I-V characteristics shifts from  $V_p = -1.5V$  at  $z = 0$  to  $V_p = +2V$  at  $z = 7$  cm. This shift indicates that the background plasma drift increases toward the anode. It does not mean that the plasma potential decreases toward the anode which would imply an electric field ( $\langle \Delta V_p / \Delta z \rangle = 0.5$  V/cm) opposing the current. Langmuir probe data are not sufficiently accurate to measure the small dc electric fields in a collisionless plasma. In the present case, the theoretical electric field based on classical resistivity and a current equal to the electron saturation current is given by  $E = v_{en} v_e / (2\sqrt{\pi} e/m_e) = 8$  mV/cm. Although in the presence of strong ion sound turbulence the resistivity is expected to be much larger,<sup>19</sup> it appears unlikely to be directly measurable with Langmuir probes, especially in the presence of drift velocity gradients. Estimates of the electric field from variations in the local floating potential are subject to additional errors since the tail in the distribution function may vary with position.

After termination of the beam injection pulse at  $t_s = 200$   $\mu$ sec, the return current also vanished. The plasma potential becomes positive ( $V_p = +5$   $kT_e/e$ ) such that the electron current to the anode is reduced to the ion saturation current. Since high energy electrons are lost preferentially the electron temperature and plasma potential decrease in time.

The temporal behavior of the beam current and voltage are shown in Figure 10. Two time scales can be distinguished. (i) For  $t \leq 40$   $\mu$ sec (top traces) density changes due to ionization are negligibly small.

The beam current is essentially constant except for a turn-on transient pulse. The anode current is the sum of the background electron saturation current,  $I_e = A_a n_e e (kT_e / 2\pi m_e)^{1/2}$ , and a fraction  $(1-T)$  of the total beam or cathode current ( $T$  is the anode transparency). Since anode and cathode current are equal their value is given by  $I_d = I_e / T$ . For the present parameters ( $n_e = 7 \times 10^9 \text{ cm}^{-3}$ ,  $kT_e = 3 \text{ eV}$ , anode area  $A_a = 421 \text{ cm}^2$ ) the expected current is  $I_d = 19 \text{ A}$  which agrees with the observed value  $I_d = 20 \text{ A}$  from Figure 10. (ii) For  $t_s \geq 40 \text{ } \mu\text{sec}$  the density increases due to ionization. This allows the beam current to rise even though the beam voltage decays which is the result of discharging the supply capacitor ( $C = 2 \text{ mF}$ ).

The beam current increases due to both ionization and heating. The temporal behavior of electron density and temperature has been measured in two cases. Figure 11(a) shows the density increase after turn-on of a 40 V discharge voltage pulse. A high background plasma density is chosen so that reliable density data from propagation of whistler waves can be obtained. The initial density increase is exponential with a time constant  $\tau_e = 150 \text{ } \mu\text{sec}$ . With an ionization rate  $\nu_i = 1.2 \times 10^6 \text{ sec}^{-1}$  (Table 1) the relative concentration of ionizing beam electrons in the center of the device is  $n_b/n_e = (\tau_e \nu_i)^{-1} = 0.6\%$  which is about an order of magnitude smaller than in the beam injection region. The beam electrons lose their energy much faster by collective effects than by collision phenomena. After the initial rise the density approaches a steady-state value, i.e. particle production and loss by diffusion balance. During beam injection, the loss rate is higher than in the low temperature quiescent afterglow. Figure 11(b) shows the electron temperature dependence during beam injection

at a lower background density ( $n_e = 2 \times 10^9 \text{ cm}^{-3}$ ). The temperature is derived from the measured sound speed of test ion acoustic waves.<sup>6</sup> During the first 50  $\mu\text{sec}$ , the test wave damping is very strong hence the measurement accuracy is low. However, from Langmuir probe data it is known that there is a fast ( $\sim 10 \mu\text{sec}$ ) initial temperature rise ( $\Delta kT_e \geq 1 \text{ eV}$ ). The initial heating process is due to resonant wave-particle interactions with the electrostatic instabilities since collisional interactions between beam and background electrons occur on a slower time scale (see Table 1). Collisional heating may explain the subsequent slow temperature rise which in turn is limited by heat losses to the anode.

Ionization phenomena can, of course, be avoided when the beam energy is kept below the ionization energy of the background gas (14 eV). Figure 12 shows Langmuir probe (No. 2,  $\phi = 0^0$ ) traces at different beam voltages both below and above ionization potential. For beam voltages  $V_b \leq 20\text{V}$  [Fig. 12(a)] beam and background flux are almost independent of beam energy whereas for higher voltages [Fig. 12(b)] the currents rise with beam energy. The beam flux is always linked to the background flux and it is not possible to raise the relative beam current by increasing the beam voltage.

The current-voltage characteristics of the beam-plasma system are summarized in Fig. 13. The characteristics depend on time since, in general, background temperature and density are affected by the beam. Steady-state conditions are approximately achieved at  $t_s \geq 0.5 \text{ msec}$ . The characteristics are, of course, functions of initial density, magnetic field, gas, pressure and geometry, too. The present beam currents are far below the emission capabilities of the cathode. At higher pressures discharge currents of  $I_d = 500\text{A}$  are readily obtained, and on smaller similar cathodes in strong magnetic fields current densities of  $j_d = 1 \text{ A/cm}^2$  are commonly observed.

#### IV. SUMMARY AND CONCLUSIONS

Time and space resolved measurements of the basic parameters in a pulsed electron beam injection experiment have been presented. It is shown that in the essentially unbounded, uniform beam-plasma system the current of the injected beam closes via a field-aligned return current of background electrons. The maximum beam current which can be injected does not significantly exceed the background electron saturation current. High frequency electrostatic instabilities inhibit the penetration of the electron beam; the beam is scattered in velocity space on a distance short compared to the collisional mean free path. Low frequency instabilities limit the drift of the background plasma to a value small compared to the electron thermal speed. The analysis of the high frequency instabilities has been presented earlier,<sup>17</sup> the low frequency instabilities will be discussed in a subsequent paper.<sup>6</sup>

#### ACKNOWLEDGEMENTS

The author wishes to thank Drs. R.W. Fredricks, W. Geikelman and W. DiVergilio for many helpful discussions. The expert technical assistance by Mr. W. Daley is also acknowledged.

This work was supported in part by TRW Independent Research and Development Funds and in part by NASA under contract NASW-2953.

\*Present address: Dept. of Physics, University of California,  
Los Angeles, CA 90024.

REFERENCES

1. G.F. Francis, in Handbuch der Physik, edited by S. Flügge (Springer Verlag, Berlin, 1956). Vol. 22, pp. 53-208.
2. R.J. Briggs, Electron-Stream Interactions with Plasmas (MIT Press, Cambridge, Mass., 1964).
3. A.B. Mikhailovskii, Theory of Plasma Instabilities (Consultants Bureau, New York, 1974) vol. 1.
4. R.W. McEntire, R.A. Henderson, and J.R. Winckler, J. Geophys. Res. 79, 2343 (1974).
5. B.B. Kadomtsev, Plasma Turbulence (Academic Press, New York, 1965).
6. R.L. Stenzel, Phys. Fluids (Submitted).
7. R.L. Stenzel, Phys. Rev. Lett. (Submitted).
8. R.L. Stenzel, Phys. Fluids 19, 857, 865 (1976).
9. R.L. Stenzel, Radio Science, to appear in December 1976.
10. R. Limpacher and K.R. MacKenzie, Rev. Sci. Instrum. 44, 726 (1973).
11. R.L. Stenzel, Rev. Sci. Instrum. 47, 603 (1976).
12. R.K. Fisher and R.W. Gould, Phys. Fluids 14, 857 (1971).
13. G. Ickovic, R. L. Stenzel and W. Geckelman, Rev. Sci. Instrum. (submitted).
14. F.F. Chen, in Plasma Diagnostic Techniques, edited by R.H. Huddlestone and S.L. Leonard (Academic, New York, 1965), pp. 113-200.
15. L. Spitzer, Jr., Physics of Fully Ionized Gases (Interscience, New York, 1962).
16. V.D. Shapiro, Zh. Eksperim. i. Teor. Fiz. 44, 613 (1963) [Engl. Trans: Sov. Phys. JETP 17, 416 (1963)].
17. R.L. Stenzel, J. Geophys. Res. (submitted).

References (Cont.)

18. S.A. Self, M.M. Shoucri, and F.W. Crawford, J. Appl. Phys. 42, 704 (1971).
19. R.Z. Sagdeev and A.A. Galeev, Nonlinear Plasma Theory (Benjamin, New York, 1969)
20. S.C. Brown, Basic Data of Plasma Physics (John Wiley, New York, 1959).

TABLE 1: BASIC PLASMA PARAMETERS

Gas, pressure	Krypton, $2.5 \times 10^{-4}$ Torr
Density ( $t_a = 24$ msec)	$n_e = 2 \times 10^9$ cm <sup>-3</sup>
Electron Temperature	$kT_e = 2$ eV
Ion Temperature	$kT_i = 0.2$ eV
Magnetic Field	$B_0 = 75$ G
Plasma frequency	$f_{pe} = 402$ MHz
	$f_{pi} = 1.05$ MHz
Cyclotron frequency	$f_{ce} = 210$ MHz
	$f_{ci} = 1.43$ KHz
Debye length	$\lambda_D = 0.23$ mm
Cyclotron radius	$r_{ce} = 0.64$ mm
	$r_{ci} = 7.7$ cm
Electron collision frequency with	
neutrals <sup>20</sup>	$\nu_{en} = 4.2 \times 10^5$ sec <sup>-1</sup>
ions <sup>15</sup>	$\nu_{ei} = 81$ sec <sup>-1</sup>
electrons <sup>15</sup>	$\nu_{ee} = 3.1 \times 10^4$ sec <sup>-1</sup>
Electron mean free path	$\lambda_e = 200$ cm
Ion-neutral charge exchange	
collision frequency <sup>20</sup>	$\nu_{in} = 5 \times 10^3$ sec <sup>-1</sup>
Ion mean free path	$\lambda_i = 13$ cm
Beam electron mean free path	
( $V_b = 40V$ ) for	
elastic collisions <sup>20</sup>	$\lambda_e = 90$ cm
ionizing collisions <sup>20</sup>	$\lambda_e' = 320$ cm
Ionization energy <sup>20</sup>	$E_i = 14$ eV

FIGURE CAPTIONS

- Fig. 1. Schematic diagram of the plasma device and diagnostic tools.
- Fig. 2. Typical time sequence of the repetitively pulsed beam injection experiment ( $t_r = 25$  msec) the first discharge pulse creates an afterglow plasma into which the beam is injected at  $t_a$ . Sampling measurements show the temporal evolution of the beam-plasma interaction.
- Fig. 3. Density decay of the afterglow plasma measured by independent techniques.  $B_0 = 75$  Gauss.
- Fig. 4. (a) Dispersion measurements of test electron plasma waves propagating along  $\vec{B}_0$  yield the density in the presence of a beam. (b) Dispersion measurements of electron cyclotron harmonic waves in the absence of beams are used for independent density diagnostics.
- Fig. 5. Langmuir probe traces in the absence (top 2 traces) and presence (bottom) of the injected beam. The one-sided plane probe faces the beam source at  $\phi = 0^\circ$  (see insert sketch) and the background plasma at  $\phi = 180^\circ$ .  $z = 7$  cm,  $V_b = 46$  V,  $B_0 = 75$  G,  $n_e = 2 \times 10^9$  cm $^{-3}$ .
- Fig. 6. Parallel electron distribution function derived by differentiating the bottom traces in Fig. 5.
- Fig. 7. Plane Langmuir probe traces sampled at a fixed time at different distances  $z$  from the cathode. The traces show that beam and background heating occur over distances short compared to the electron mean free path ( $\lambda_e = 90$  cm).  $t_a = 24$  msec,  $B_0 = 75$  G.
- Fig. 8. Langmuir probe traces in the middle of the plasma device ( $z = 125$  cm) for the probe facing the beam ( $\phi = 0$ ) and opposing it ( $\phi = 180^\circ$ ). As a result of electrostatic instabilities the beam has been broadened and lost most of its energy on a scale length short compared to the ionization mean free path ( $\lambda_e = 300$  cm).

- Fig. 9. Plane Langmuir probe traces sampled at different times before, during and after the beam injection pulse. The probe is located at the anode ( $z = 0$ ) and faces the background plasma ( $\phi = 180^\circ$ ). During beam injection the grounded anode draws currents in excess of the electron saturation current; in the absence of the beam the anode is at the floating potential.  $V_b = 45V$ ,  $t_a = 24$  msec,  $B_0 = 75$  G, Kr  $2 \times 10^{-4}$  Torr.
- Fig. 10. Cathode current and voltage vs. time on different scales ( $\phi =$  common zero line). At early times ( $t \leq 40$   $\mu$ sec) the beam current is constant. It is limited by the return current carried by the background plasma whose density increases on the longer time scale due to ionization.
- Fig. 11. (a) Density increase during injection of an ionizing electron beam into a dense partially ionized background plasma. The density is determined from the dispersion of whistler waves.  
(b) Electron temperature vs. time during beam injection into a low density background plasma. The temperature is obtained from ion sound speed measurements; the dashed initial rapid rise is inferred from probe measurements.
- Fig. 12. Langmuir probe traces at a fixed sampling time  $t_s$  and position ( $z = 7$  cm,  $\phi = 0^\circ$ ) for different beam voltages below (a) and above (b) ionization potential (14 eV). The beam current does not increase with voltage unless the background electron density and temperature are raised.
- Fig. 13. Current-voltage characteristics of the beam source. Since the injected beam current is limited by the return current the characteristics depend on initial background plasma parameters and subsequent temperature and density changes due to the beam-plasma interaction.

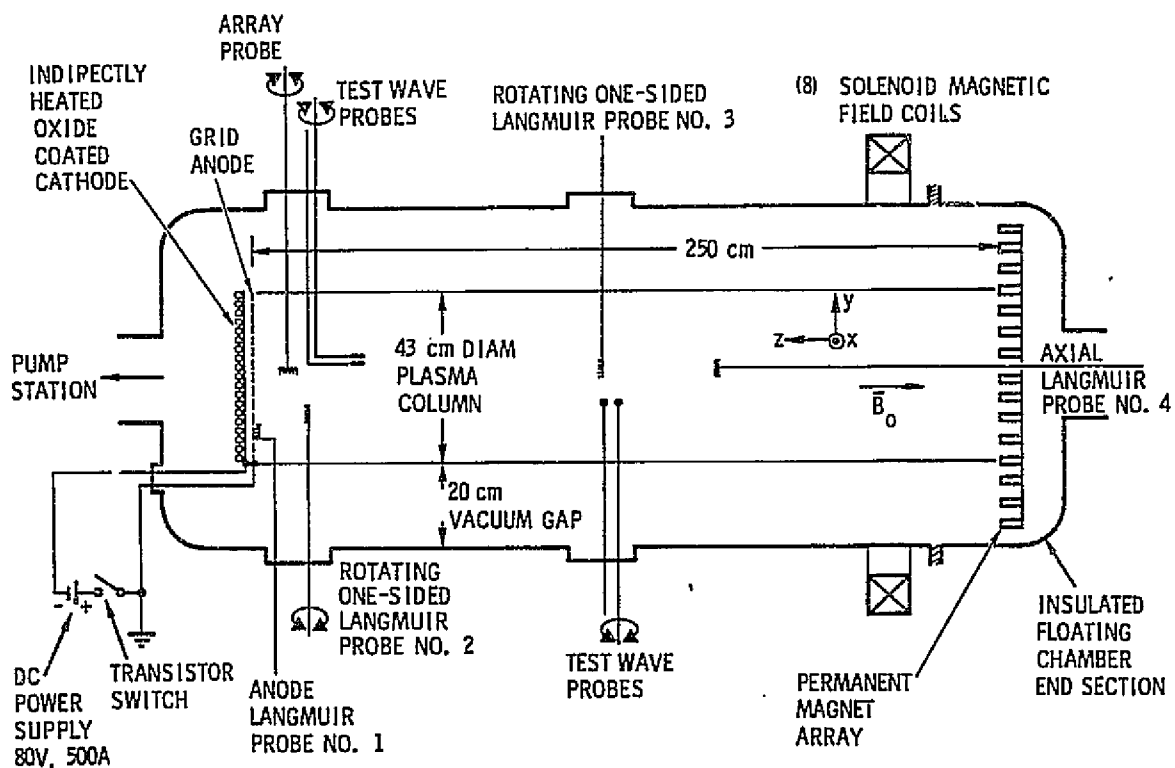


FIGURE 1

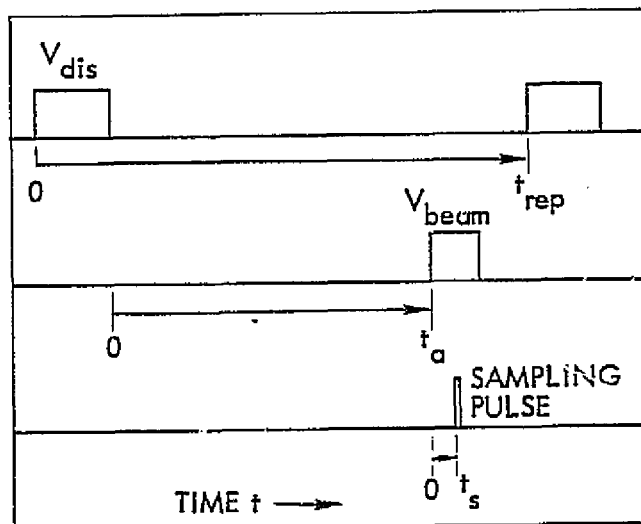


FIGURE 2

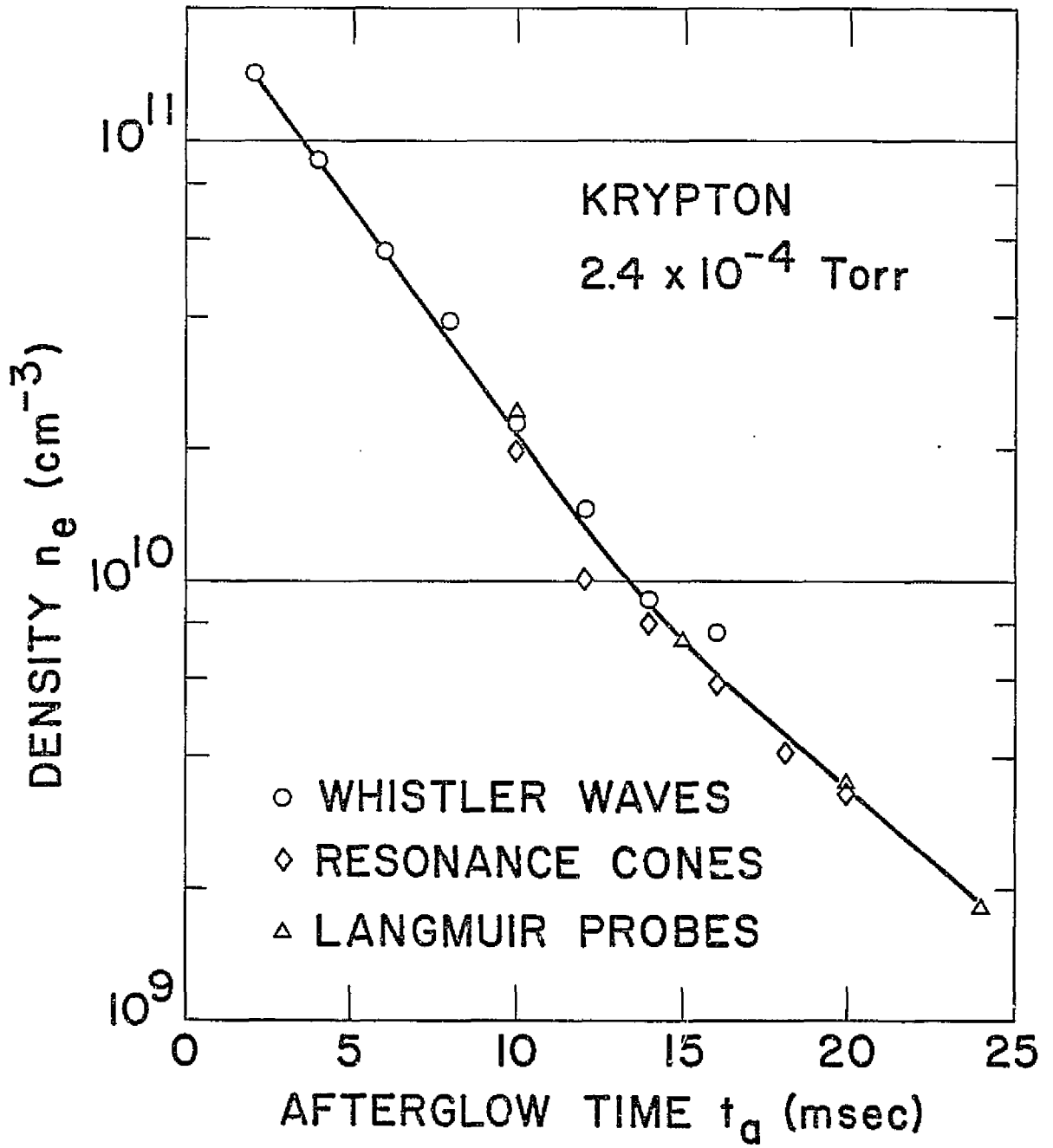


FIGURE 3

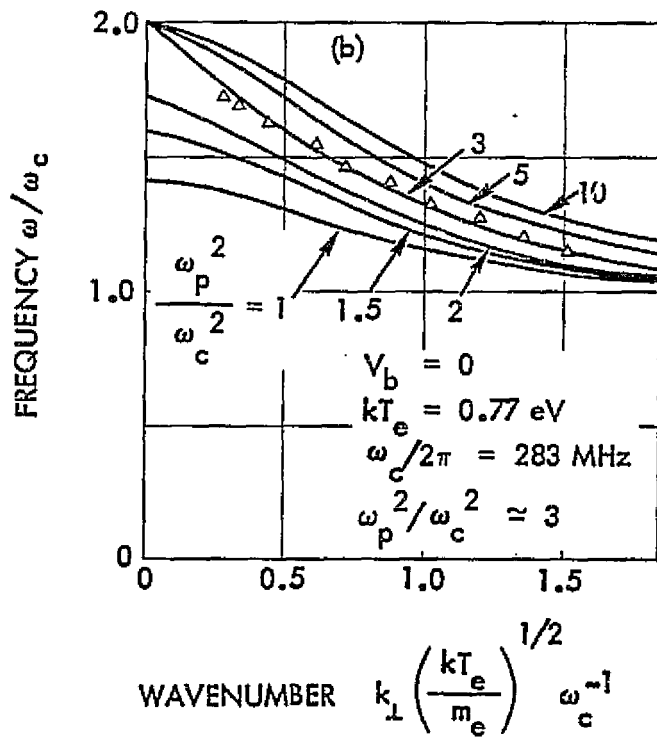
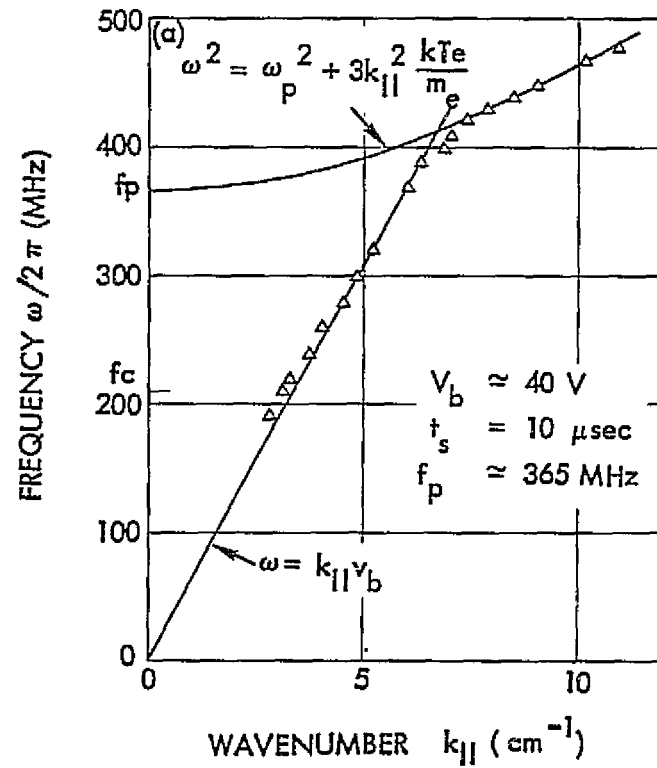


FIGURE 4

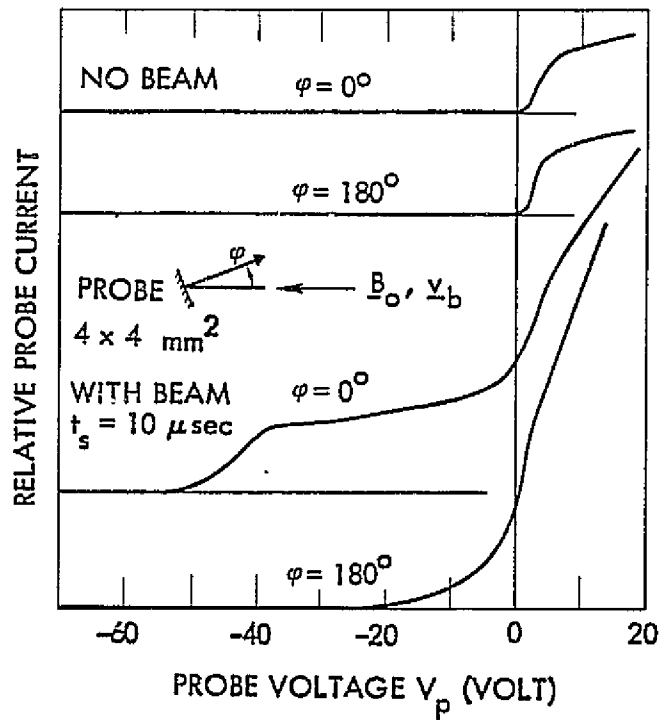


FIGURE 5

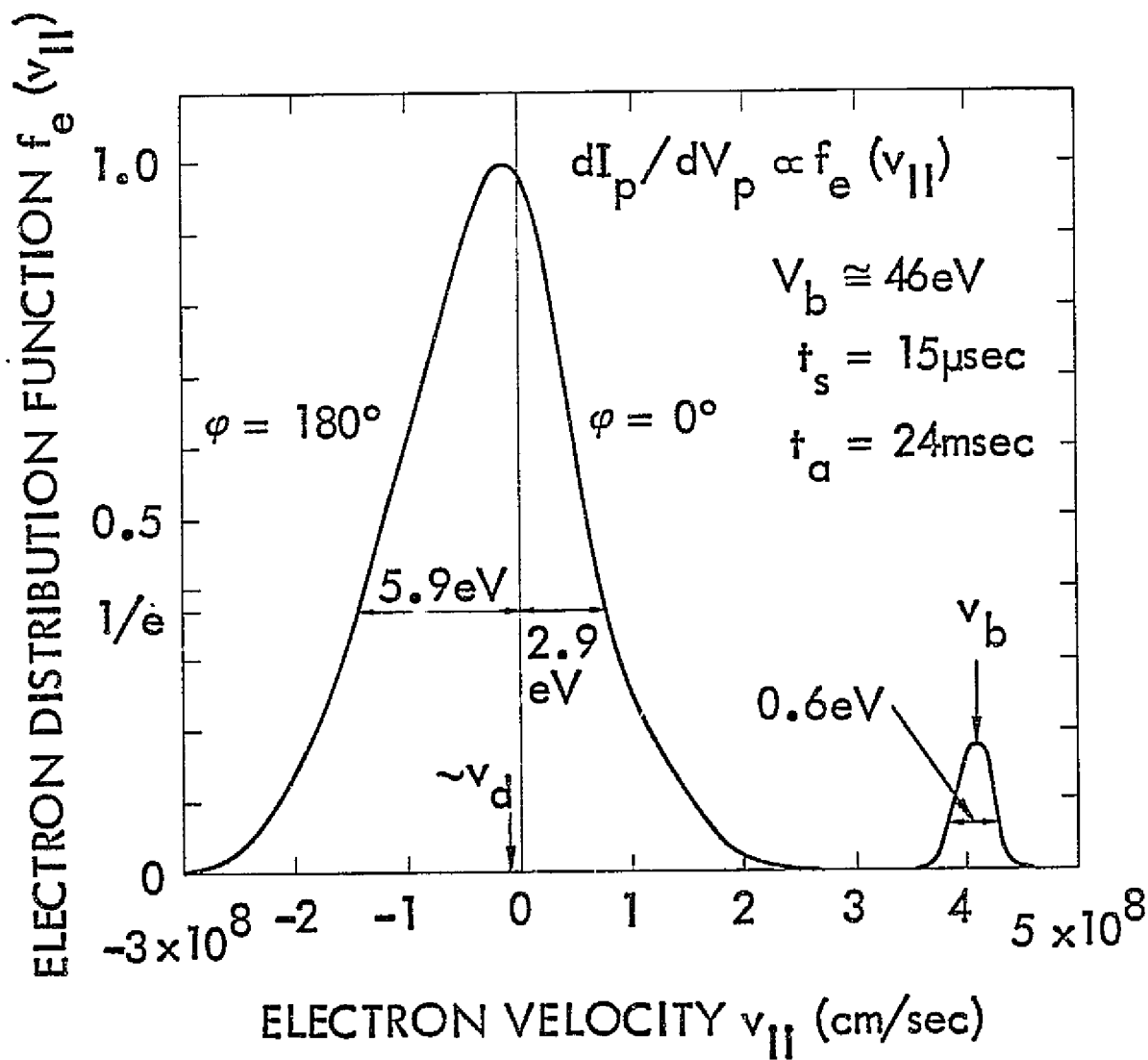


FIGURE 6

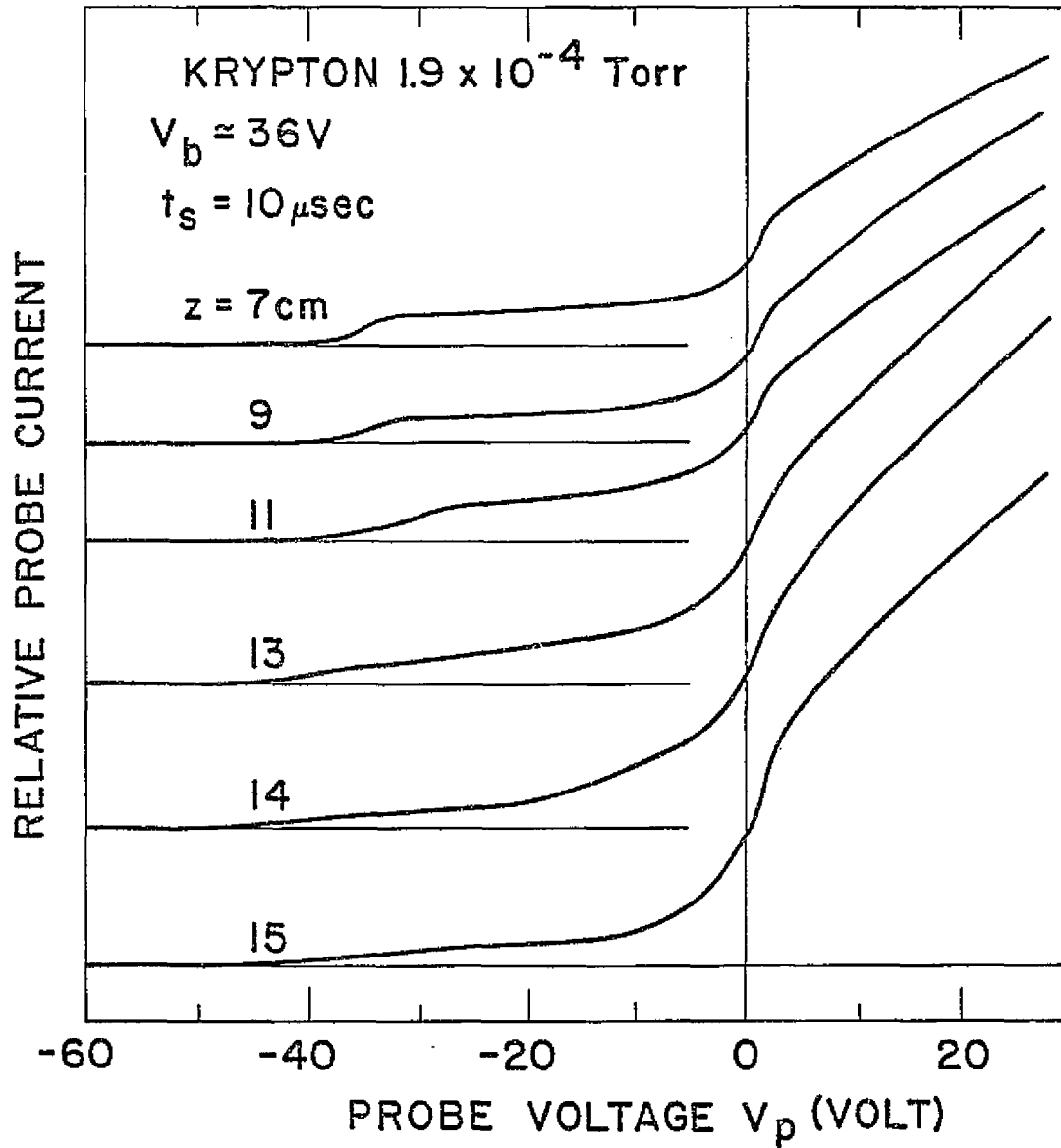


FIGURE 7

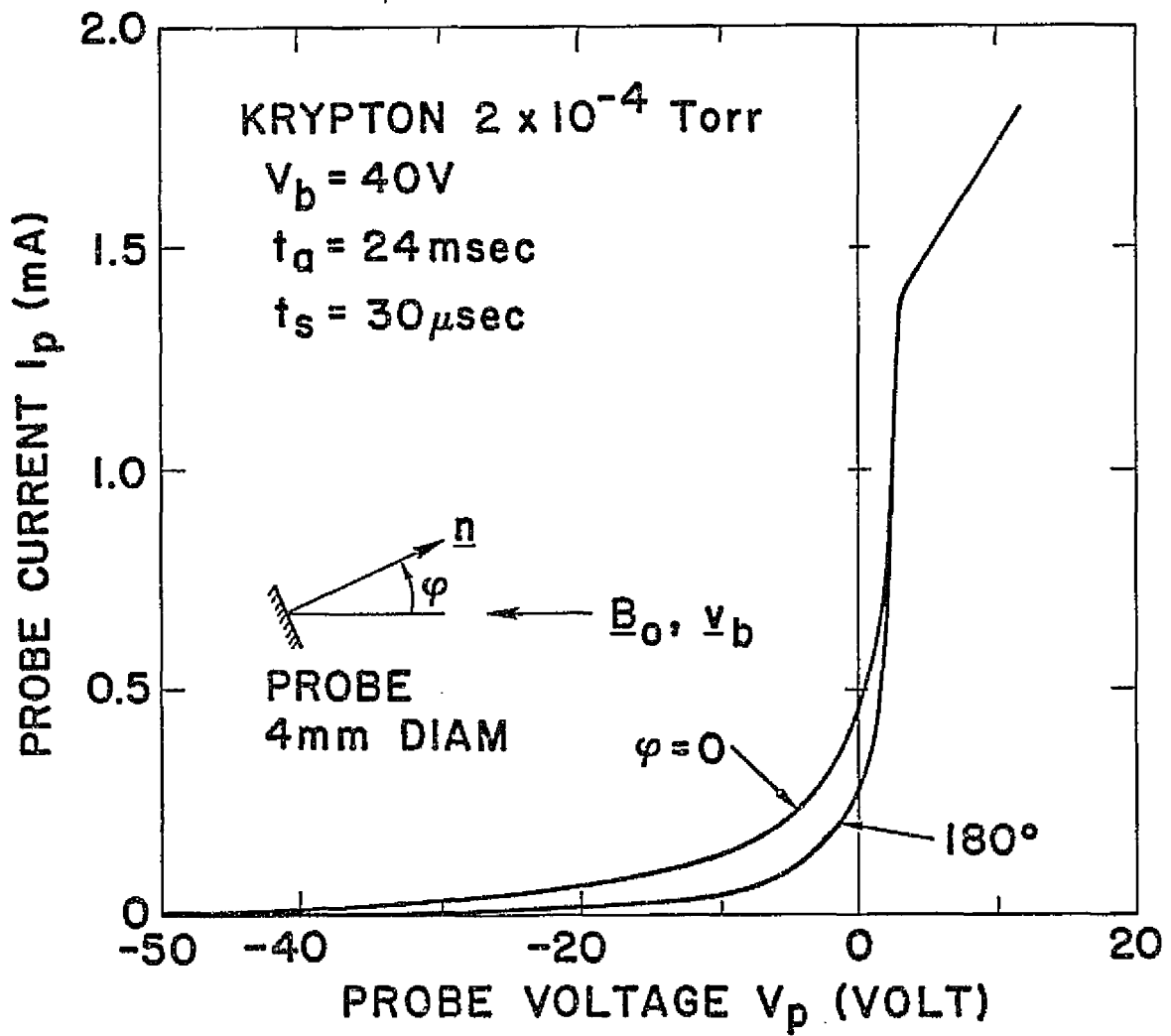


Figure 8

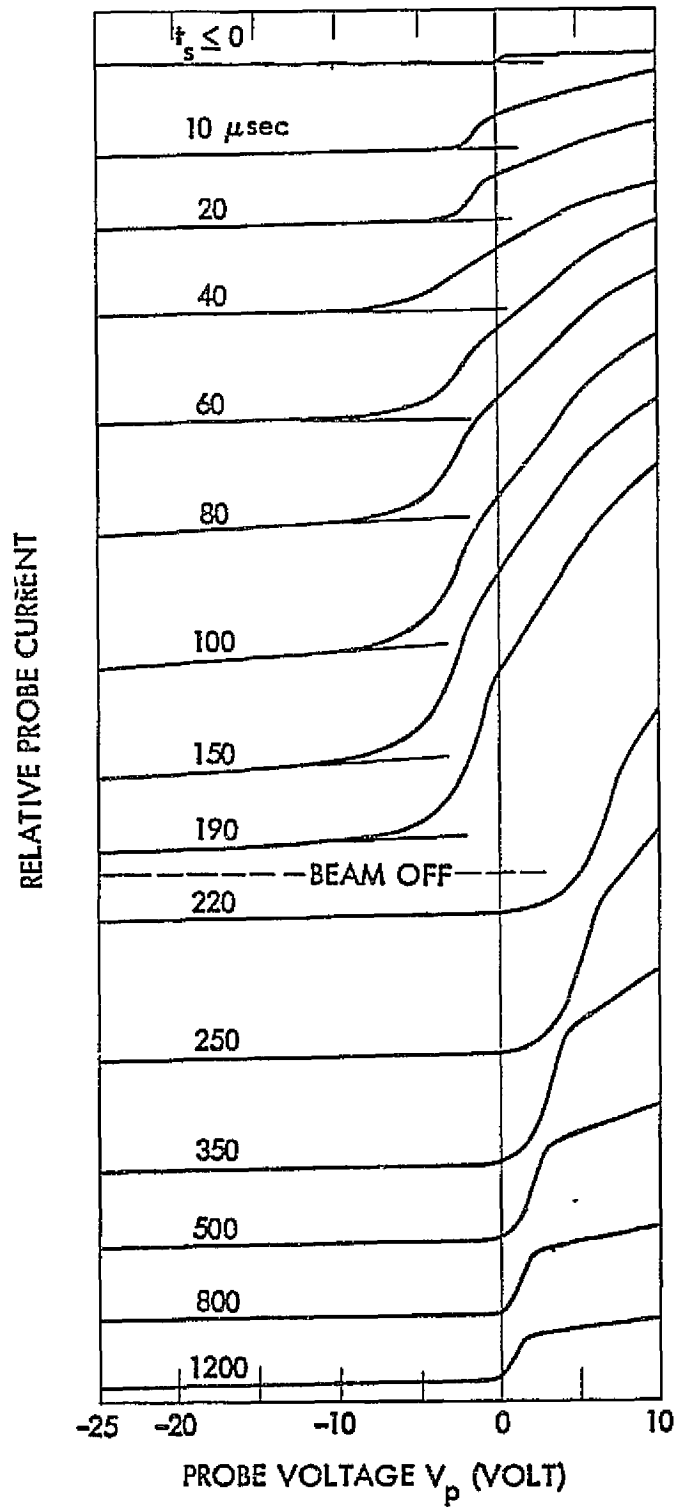


FIGURE 9

ORIGINAL PAGE IS  
OF POOR QUALITY

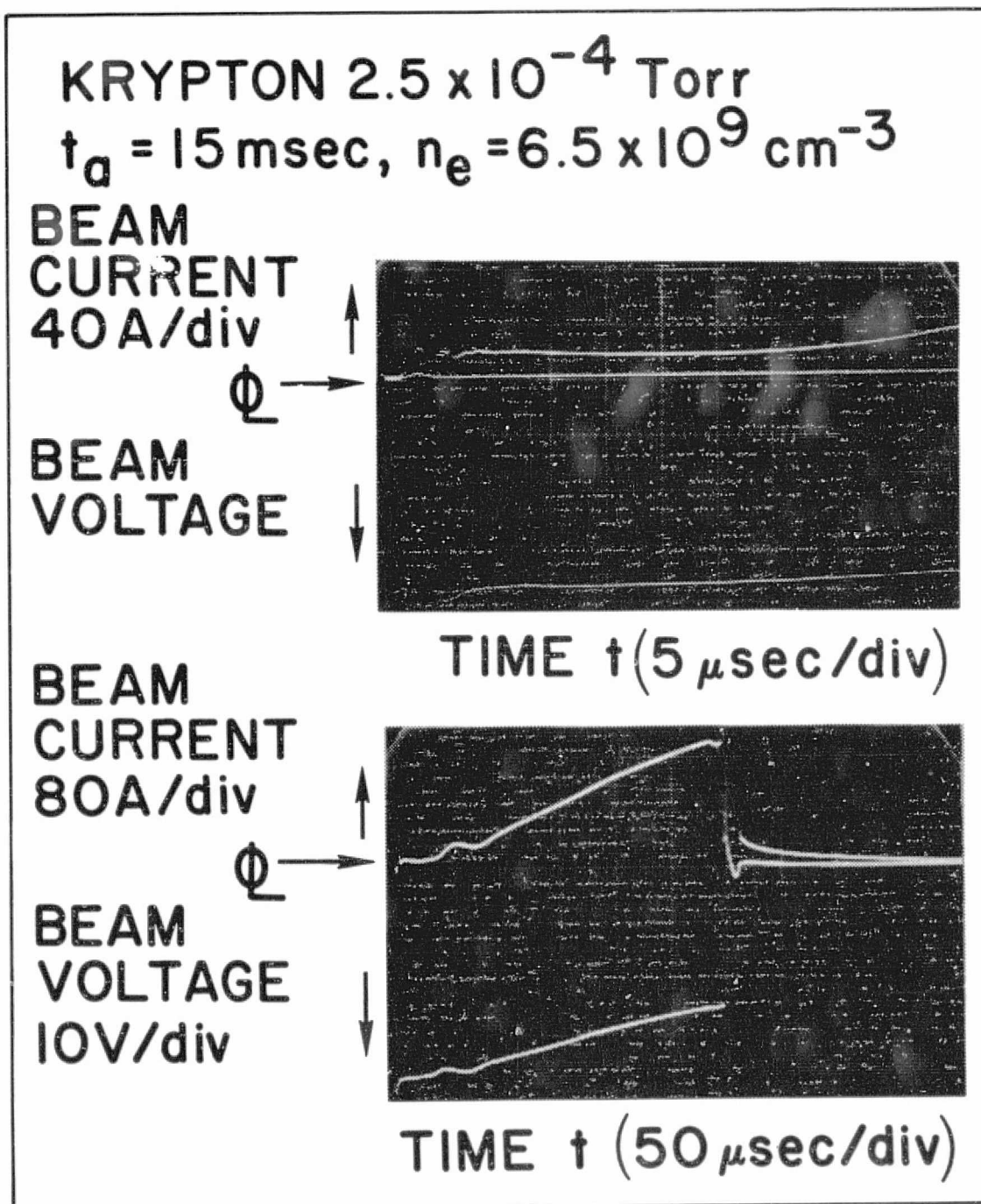


FIGURE 10

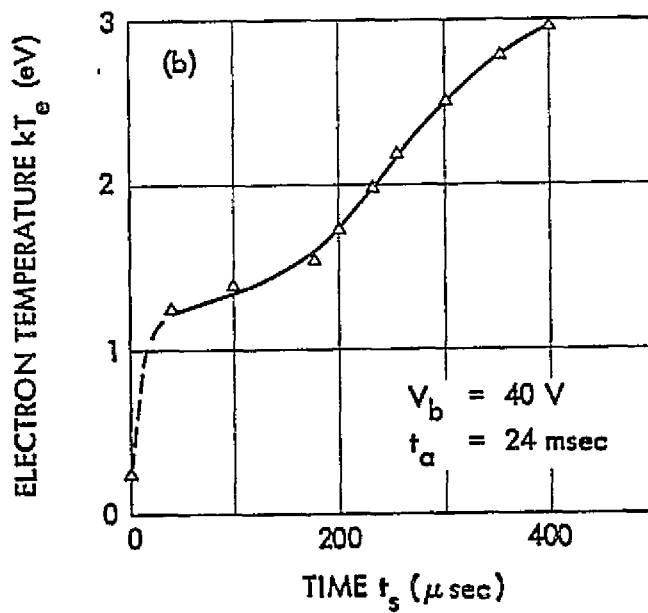
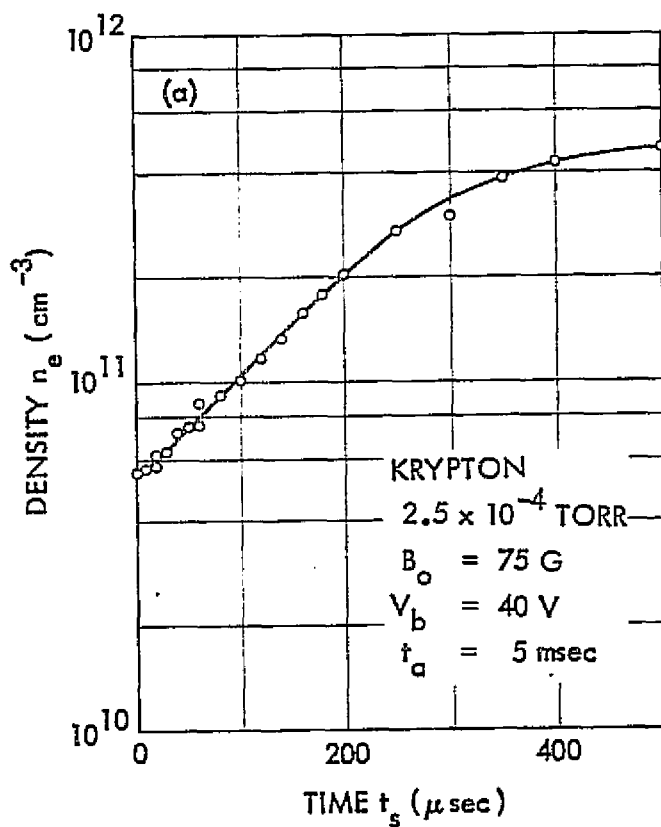


FIGURE 11

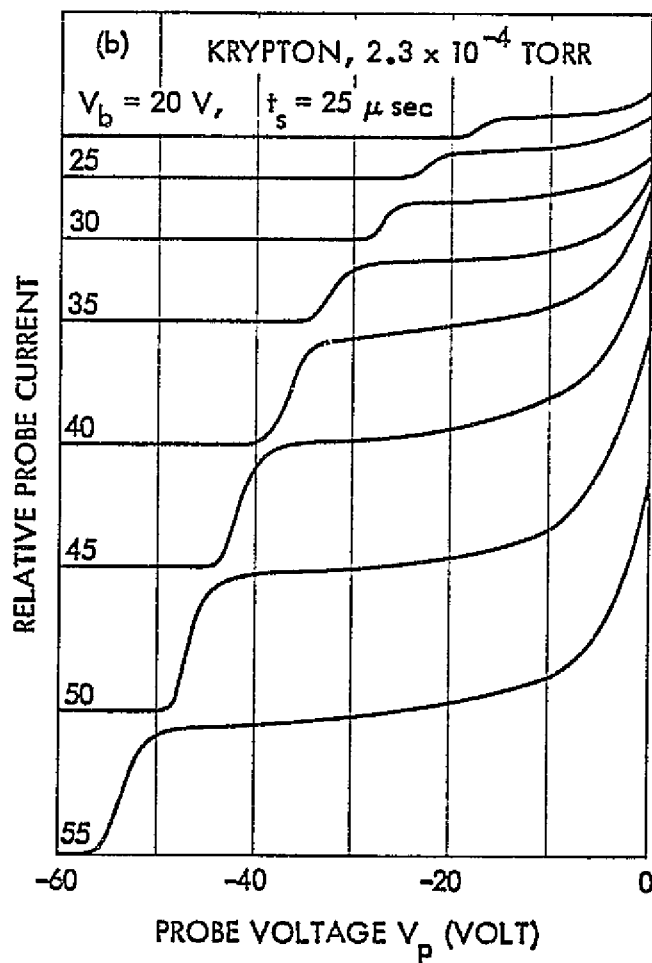
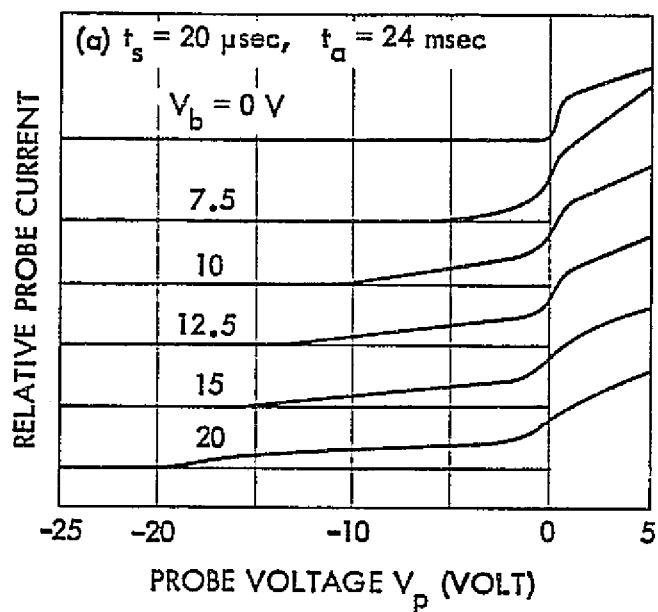


FIGURE 12

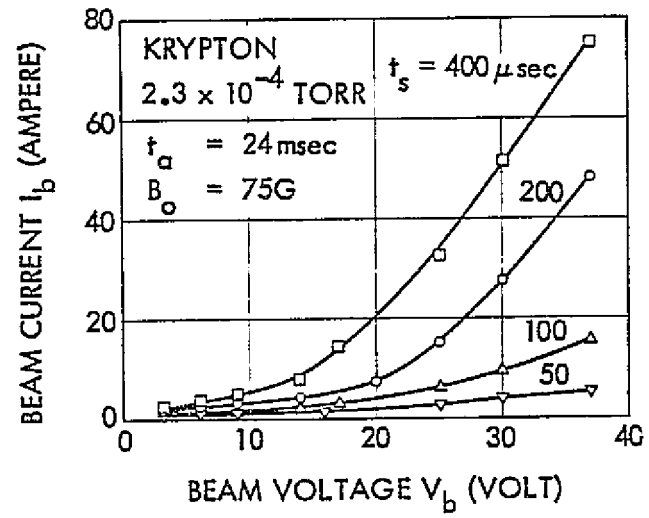


FIGURE 13

N77-27261

APPENDIX C

THREE-DIMENSIONAL ION SOUND TURBULENCE

Principal Contributor: R.L. Stenzel

EXPERIMENTS ON CURRENT-DRIVEN THREE-DIMENSIONAL ION SOUND TURBULENCE

PART II. WAVE DYNAMICS

R. L. Stenzel\*

TRW Systems, Redondo Beach, California 90278

ABSTRACT

A fast (40 eV), cold ( $< 1$  eV), large diameter (43 cm) electron beam is injected along  $\vec{B}_0$  (75 G) into a uniform background plasma ( $10^9 < n_e < 10^{10}$  cm $^{-3}$ ,  $kT_e = 10$  kT $_i = 2$  eV). The injected beam current is balanced by a field-aligned return current which gives rise to an ion acoustic instability ( $c_s \ll v_d < v_e$ , where  $c_s$ ,  $v_d$ ,  $v_e$  are sound, drift and electron thermal velocity, resp.). The plasma is essentially unbounded (characteristic dimensions  $10^3$  Debye lengths) and collisionless on the time scale of the pulsed experiment ( $v_{in}/\omega_{pi} = 5 \times 10^{-3}$ ). The fluctuations are analyzed by probe techniques in real time and space as well as in the frequency and wavenumber domains. Strong density fluctuations are observed in the entire ion acoustic spectrum reaching peak amplitudes ( $\delta n_e/n_e = 20\%$ ) at the low frequency end ( $\omega/\omega_{pi} = 0.2$ ). The shape of the frequency spectrum is close to that predicted by renormalized plasma turbulence theory. The current is pulsed and the development of the instability from linear growth to saturation is observed. Spatial correlation measurements indicate that the turbulent wave vector spectrum extends in magnitude to  $k\lambda_D \gtrsim 1$  and in angle up to  $\pm 90^\circ$  with respect to the electron drift direction. The propagation of phase coherent test

---

\* Also at Department of Physics, University of California, Los Angeles, California 90024.

waves in the current carrying plasma is investigated. For the highly turbulent regime strong damping is observed while at lower drift velocities well defined wave propagation within a half space centered around the drift velocity direction is observed. Phase and amplitude contours of test waves in orthogonal planes are presented. Oblique propagation of two strong test waves at different frequencies indicate the role of nonlinear ion Landau damping in absorption of wave energy.

## I. INTRODUCTION

The current-driven ion acoustic instability is a well known phenomenon which has been analyzed in theory<sup>1-6</sup>, computer simulations<sup>7,8</sup>, and many experiments.<sup>9-18</sup> While the linear properties are understood the non-linear saturation which may involve strong turbulence remains to be explained. Experimentally, the instability is produced either by driving a toroidal current with an induced electric field<sup>11</sup> or by drawing a current between two electrodes. The latter approach has been thoroughly studied in positive columns<sup>9,14,17,18</sup>, i.e. collisional, bounded and unmagnetized plasmas. Some work has been done in weakly collisional plasmas<sup>10,12,13,15,16</sup> few of which can be considered free of boundary effects.

In the present experiment a current driven ion sound instability is observed in an essentially collisionless and unbounded plasma immersed in a uniform magnetic field. The current corresponds to the field-aligned return current associated with the injection of a fast electron beam into a magnetized background plasma as described in the companion paper.<sup>19</sup> The current is pulsed and the evolution of the instability is observed. The instability saturates within approximately 15 ion plasma periods at a level of strong turbulence ( $W/n_e kT_e \approx 5\%$ , where  $W$ ,  $n_e kT_e$  are wave energy and kinetic particle energy, respectively). Distribution function measurements<sup>19</sup> show that the drift velocity is much larger than sound speed although it remains well below the electron thermal velocity ( $v_d \lesssim 0.1 v_e$ ). The distribution function is not Maxwellian. Analysis of the unstable waves indicates that the propagation is, in general, three dimensional. The correlation lengths are approximately  $50\lambda_D$  ( $\lambda_D$  = Debye length) in the highly turbulent state. Simultaneous observations of density fluctuations

in time at different locations with an array probe show the microscopic properties of turbulence, i.e. growth, propagation and decay of perturbations.

The propagation of test ion acoustic waves in the current carrying plasma gives additional insight into the instability properties. While previous investigations<sup>15</sup> were restricted to one-dimensional propagation along the electron drift the present experiments show the three-dimensional propagation characteristics. At lower turbulence levels weakly damped test wave propagation is observed in an angular half space centered about the direction of the drift velocity. Propagation of two oblique test waves of large amplitudes results in an off-resonant beat mode which is strongly Landau damped when the phase velocity is near the ion thermal speed. Non-linear ion Landau damping has been proposed<sup>3</sup> as an important mechanism for energy absorption and transfer among different modes.

Since the experimental setup and techniques have been described earlier<sup>19</sup> the present paper starts with the measurement results. The characteristics of the instability are given in Section II and the test wave experiments are presented in Section III. The results are discussed and summarized in the final Section IV.

## II. INSTABILITY ANALYSIS

The presence of a low frequency instability is readily inferred from the large fluctuation level in the Langmuir probe saturation current. While the previously shown probe traces<sup>19</sup> represented time-averaged values Fig. 1 displays a fast sweep of the probe characteristics during the pulsed beam injection. The probe voltage (top trace) varies linearly in time; the probe current (bottom trace) is recorded for three single shot exposures. One can see large amplitude ( $\delta n_e/n_e = 25\%$ ), low frequency ( $f = 200$  kHz)

fluctuations in the electron saturation current which are uncorrelated from pulse to pulse. The current fluctuations are not due to fluctuations in the plasma potential but represent density fluctuations. When a high impedance probe circuit is used the fluctuations are also observed in the ion saturation current. However, the frequency response is found to be much better in the electron saturation regime than for ion collection.

The presence of strong density fluctuations is confirmed by probe independent diagnostics. A resonance cone is excited with a short-wire antenna at a frequency  $\omega < \omega_c < \omega_p$ .<sup>20,21</sup> Since the cone angle is a function of density low frequency density fluctuations scatter the cone angle. When the rf field is detected with a second antenna the received signal is amplitude and phase modulated as a result of the spatial deflection of the cone with respect to the fixed antenna.<sup>22</sup> Fig. 2 shows the frequency spectrum of a small amplitude resonance cone signal in the presence of the return current. The lower sideband indicates the presence of broadband density fluctuations. The shape of the modulation spectrum varies with probe location across the cone. The sideband vanishes in the absence of the return current. Although this observation is rather qualitative it nevertheless confirms that the density perturbations detected with Langmuir probes are real and not caused by probe perturbations on the plasma.

Due to the pulsed nature of the experiment growth and saturation of the instability can be observed. Fig. 3 shows on the top trace the pulsed beam voltage ( $V_b = 35$  V) vs time and on the bottom trace the electron saturation current to a small cylindrical Langmuir probe (0.13 mm diam., 2.5 mm length). Several traces are superimposed so as to indicate the transition from coherence to turbulence. The instability grows coherently for approximately two periods of oscillations at  $f = 400$  kHz and then goes

over into turbulence which is fully developed and saturated ( $\delta I_e/I_e =$  constant) after 10 to 15 ion plasma periods ( $f_{pi} = 1$  MHz). The increase in the average electron saturation current is due to heating of background and beam electrons and the associated change in the saturation characteristics of small probes.<sup>19</sup> The observed growth characteristics are essentially independent of probe position, thus the instability starts throughout the plasma volume. Since the coherent growth time is short the subsequent observations will apply to the saturated state.

The frequency spectrum of the saturated instability is shown in Fig. 4. The noise extends through the entire ion acoustic frequency range but exhibits a pronounced maximum ( $\delta n_e/n_e = 20\%$ ) at the low frequency end ( $\omega/\omega_{pi} = 0.2$ ). The low frequency peak in the spectrum is not the result of collisions ( $v_{in}/\omega_{pi} = 0.005$ ), ion cyclotron modes ( $\omega_{ci}/\omega_{pi} = 0.001$ ) or boundary effects ( $c_s/D = 5$  kHz,  $D$  is the plasma diameter) but is a characteristic property of the stationary turbulence spectrum. According to renormalized turbulence theory<sup>6</sup> which considers both scattering of ions and electrons by the waves the long wavelength Landau resonance is destroyed by electron scattering while the short wavelength intensity fall-off is the result of nonlinear ion Landau damping.<sup>3</sup> The observed spectrum has the same characteristic shape as that predicted by Horton et al. (See Figure 2 in Ref. 6). The spectrum may be considered stationary since its shape does not significantly vary in time provided the slowly rising value of  $\omega_{pi}$  is taken into account. The wave energy normalized to the particle energy density is  $W/n_e kT_e = (\delta n_e/n_e)^2 = 5 \times 10^{-2}$ . This is a large value; for example, the wave electric field at the peak noise frequency  $f = 200$  kHz ( $\lambda = 5$  mm) is  $|\delta E| = k\delta\phi = 2.5$  V/cm. Although  $\delta\phi$  decreases with increasing  $\omega$  the electric field remains large as  $\omega \rightarrow \omega_{pi}$ .

The wavenumber spectrum is determined by correlation techniques. The broadband signals (frequency range 0.05 - 5 MHz) of two identical, movable, cylindrical Langmuir probes (0.13 mm diam, 2.5 mm length, 1 mm diam shield) are multiplied, sampled and time-averaged. Either probe signal  $\phi_1$ ,  $\phi_2$  can be delayed by a broadband delay line. For three-dimensional wave propagation the measured unnormalized cross correlation function  $C_{12}(\Delta\vec{r}, \tau) = \int \phi_1(\vec{r}, t) \phi_2(\vec{r} + \Delta\vec{r}, t + \tau) dt$  is a function of three spatial coordinates  $\Delta\vec{r} = (\Delta x, \Delta y, \Delta z)$  and delay time  $\tau$ . First, in Fig. 5(a), the correlation signal is displayed vs one variable, the coordinate  $\Delta z$  along the electron drift. The half width of the correlation signal,  $\Delta z = 1$  mm, gives a measure for the spread in the magnitude of the wavenumber  $k_{||}$ . It does, however, not indicate the spread in the angular k-vector spectrum. Fig. 5(b) displays the cross correlation function vs two coordinates along and across  $\vec{B}_0$ . The value of  $C_{12}(0, \Delta y, \Delta z, 0)$  is indicated by contours of constant relative amplitude. The observed elliptical shape of the correlation surface indicates a strong angular spread in wave propagation with respect to the drift direction along  $\vec{B}_0$ .

The direction and velocity of wave propagation is determined by displaying  $C_{12}$  as a function of delay time  $\tau$  and position variables. Fig. 6 shows the propagation characteristics along  $\vec{B}_0$ . With increasing delay ( $\tau > 0$ ) of the movable probe signal (No. 2) the peak of the correlation signal shifts to negative values of  $\Delta z$ , and vice versa for delay ( $\tau < 0$ ) in the stationary probe signal (No. 1, located at  $\Delta z = 0$ ). Thus, the wave propagation points in the direction of the electron drift. From the diagram of Fig. 6(b) the parallel phase velocity is found to be  $v_e = 1.9 \times 10^5$  cm/sec which corresponds to sound speed in Krypton at  $kT_e = 3$  eV. Further useful information can be obtained from the spatial amplitude decay of the cross correlation signal. The e-folding decay length which

is a measure of the coherence length of the waves is found to be

$$\Delta z_c = 4 \text{ mm} = 50\lambda_d.$$

The two-dimensional cross correlation function shown in Fig. 5(b) does not completely describe the oblique propagation characteristics. The frequent assumption of propagation symmetry in the plane normal to the drift direction is not supported by the present observations. Fig. 7 shows cross correlation measurements in a plane normal to  $\vec{B}_0$ . The correlation signal along the coordinate  $\Delta x$  normal to the plane of Fig. 5(b) is shown in the upper part of the figure. By taking a number of such traces at different positions  $\Delta y$ , except for  $\Delta y = 0$  where probe shafts interfered, the map of Fig. 7(b) is obtained. Although no gradients in the bulk plasma properties have been noticed there are preferred directions of wave propagation normal to the major axes of the elliptical contours. Whether this asymmetry is the localized wave propagation in  $\vec{k}$ -space proposed by Kadomtsev<sup>3</sup> or is a result of minor gradients in the electron drift direction is difficult to assess. The minimum half widths of the correlation peaks are comparable to the values of the axial correlation function. Thus, in different planes ( $\Delta \vec{r}, \Delta z$ ) one can find varying degrees of angular spread around  $\vec{v}_d$  ranging from  $\theta = \arcsin(v_d/c_s) = 90^\circ$  to nearly zero.

The direction and speed of wave propagation in the perpendicular plane are indicated in Fig. 8. In contrast to Fig. 6(a), the correlation function does not shift with increasing delay in a unique direction but splits and moves in opposing directions. Thus, there are waves propagating both to the right and to the left along the axis  $\Delta x$ . The propagation speed ( $v_p = 2.2 \times 10^5$  cm/sec) is larger than sound speed indicating that the waves are again oblique to the chosen coordinate. Clearly, for a complete description

of the wave properties the full cross correlation function depending on all 4 variables has to be measured. In principle, this can be done with the present techniques but, in practice, this formidable task requires the aid of a computer for data handling which was, unfortunately, not available.

A different approach to characterize turbulence is the direct display of the fluctuations in real time and space. This is done with an array probe and a multi-channel data display as shown in Fig. 9. The signals from six identical, radially displaced, cylindrical Langmuir probes are displayed simultaneously on three dual beam oscilloscopes. A single shot exposure of the fluctuations vs time at different points in space is shown in Fig. 10. The figure displays the microscopic properties of turbulence: There are density perturbations which grow (a) or decay (b) in the direction along the array. From the time delay and probe spacing one concludes that these are waves propagating close to sound speed ( $v_p = 1.4 \times 10^5 \frac{\text{cm}}{\text{sec}}$ ) in the direction from probe No. 6 to No. 1 essentially perpendicular to the electron drift. The amplitude growth and decay thus reflect the coherence properties rather than oblique propagation effects. The typical "lifetime" of a density perturbation is 7  $\mu\text{sec}$  during which it propagates about 10 mm. There are also waves which propagate oblique to the array (c,d) as indicated by higher phase velocity components ( $v_p = 2.5 \times 10^5 \frac{\text{cm}}{\text{sec}}$ ) and smaller amplitude variations following more along the crest of the waves. By expanding the array to two or three coordinates one can, in principle, determine the propagation direction, velocity and amplitude behavior of individual density fluctuations.

### III. TEST WAVE PROPAGATION

By launching small amplitude monochromatic test ion acoustic waves from a well defined source useful information about the growth rate and saturation process of the instability can be obtained.<sup>15</sup> In the presence of strong turbulence the ion acoustic wave dispersion is expected to be modified<sup>23,24</sup>, and test wave experiments on new ion sound modes have been reported.<sup>25,26</sup> In rather few experiments three-dimensional wave propagation effects have been considered.<sup>27</sup>

In the present test wave studies the waves are excited near the anode ( $z = 7$  cm) from one of the short cylindrical Langmuir probes (0.13 mm diam, 2.5 mm length) and received with the second identical probe. In the plane normal to the exciter wire azimuthally symmetric cylindrical waves are excited in the absence of drifts. The receiver probe can be scanned in this plane, and the plane can be inclined with respect to the magnetic field. Thus, with minimum perturbation on the plasma three-dimensional propagation effects can be investigated.

#### Propagation of a Single Mode

In the measurements presented here the exciter signal is a single frequency cw signal. The receiver signal is usually amplified and applied to a broadband interferometer circuit whose output is proportional to  $\phi_1(\vec{r}, t) \cos(\vec{k}_1(t) \cdot \vec{r})$  where  $\phi_1(\vec{r}, t)$ ,  $\vec{k}_1(\vec{r}, t)$  are wave potential and propagation vector, resp., which may vary in space and time slowly compared to a wavelength and oscillation period, respectively. Fig. 11(a) shows the interferometer signal vs time at a fixed frequency ( $f = 3$  MHz) and axial probe spacing ( $\Delta z = 12$  mm). Also indicated are the beam pulse (top) and the sampling pulse (bottom trace). The growing oscillations indicate that amplitude and wave number vary in time. The former is

mainly due to the density increase which raises  $\omega_{pi}$  to above  $\omega$  and then reduces ion Landau damping as  $\omega \ll \omega_{pi}$ , and partly due to the lower level of turbulence at later times when the current penetration decreases. The latter is mainly due to electron heating ( $k = \omega/c_s = T_e^{-1/2}$ ) and partly due to dispersion [ $k = k(\omega_{pi}, T_e)$ , see Eq. (1)]. The fluctuations in the traces indicate the scattering of the test wave by the background noise which is not directly visible due to some low pass filtering of the interferometer signal. At early times ( $t_s < 100 \mu\text{sec}$ ) test wave propagation at any frequency  $\omega < \omega_{pi}$  exhibits severe damping due to wave-wave interactions in the strong turbulence. After the end of the current pulse the amplitude sharply drops since the instability vanishes. The wavenumber increase due to electron cooling gives again rise to an oscillatory pattern.

The temporal variation of the wavenumber gives rise to a phase modulation of the test wave signal which is either observable in the time domain [Fig. 11(a)] or the frequency spectrum as shown in Fig. 12. In the latter case the received signal  $\phi_1 \cos(\omega t - k\Delta z)$  is directly applied to a spectrum analyzer whose output is sampled. During the beam pulse [Fig. 12(b)] the decrease in  $k$  produces an upshifted sideband, in the afterglow of the beam pulse [Fig. 12(c)] the increase in  $k$  lowers the frequency. If the frequency spectrum were the only data available as is common in many pulsed experiments the interpretation of the sidebands could be ambiguous since Doppler effects and wave scattering produce similar results.

In Fig. 11(b) the interferometer signal is sampled at a fixed time  $t_s$  and displayed vs probe separation  $\Delta z$ . The test wave propagates at an almost constant amplitude in the direction of the electron drift. The phase velocity ( $v_p = f\lambda_{||} = 1.7 \times 10^5 \text{ cm/sec}$ ) corresponds to sound speed

in Krypton at  $kT_e = 3$  eV, a value approximately found from Langmuir probes.<sup>19</sup> By varying the sampling time the change in wavelength or electron temperature is verified.

At a fixed sampling time the test wave dispersion relation  $\omega$  vs  $k_{||}$  has been measured (Fig. 13). Due to the presence of the de-stabilizing electron drift waves almost up to the ion plasma frequency ( $f_{pi} = 3$  MHz) can be launched from a simple wire exciter. Since the probe dimensions are small (0.13 mm diam) and a high precision probe drive system has been used wavelengths as short as 300  $\mu\text{m}$  ( $k\lambda_D = 1.3$ ) have been measured which is commonly considered the regime restricted to laser scattering diagnostics.<sup>18</sup> The figure shows a constant phase velocity equal to sound speed  $c_s = \omega_{pi} \lambda_D$  at low frequencies and dispersion effects near the ion plasma frequency as predicted by the dispersion relation for ion acoustic waves from fluid theory

$$\omega = \omega_{pi} \frac{k\lambda_D}{(1 + k^2 \lambda_D^2)^{1/2}} \quad (1)$$

The detailed amplitude and phase distribution of a monochromatic test wave in a plane along  $\vec{B}_0$  (coordinate  $z$ ) and across  $\vec{B}_0$  (coordinate  $y$ ) is shown in Fig. 14. The exciter probe is located at the origin with its axis normal to the measurement plane. Fig. 14(a) presents a raw-data interferometer trace along  $\vec{B}_0$  which indicates weakly damped large amplitude ion waves propagating parallel to the electron drift  $\vec{v}_d$ , and strongly decaying small amplitude waves in the direction opposing  $v_d$ . Since the test wave is not a plane wave but diverges the constant amplitude pattern implies spatial growth.

Fig. 14(b) shows the phase fronts, i.e., contours of the interferometer maxima (circles) and minima (crosses). There is a noticeable difference in the parallel wavelengths or phase velocities along  $\vec{v}_d$  ( $v_{p+} = f\lambda_+ = 1.86 \times 10^5$  cm/sec) and opposing  $\vec{v}_d$  ( $v_{p-} = 1.02 \times 10^5$  cm/sec). A possible explanation for the asymmetry is a Doppler shift due to an ion drift toward the anode. The drift velocity is approximately  $v_{di} = (v_{p+} - v_{p-})/2 = 4.2 \times 10^4$  cm/sec, i.e.  $v_{di}/c_s = 0.29$  where  $c_s = (v_{p+} + v_{p-})/2 = 1.44 \times 10^5$  cm/sec. In a quiescent plasma the ions could not possibly drift against the electric field associated with the electron return current. However, in the present turbulent plasma where the wave electric field ( $|\delta E| = 2.5$  V/cm) is much larger than the dc field ( $E_{dc} = m v_d v_e / e \approx 0.14$  V/cm, where  $v_d \approx 0.1 v_e = 10^7$  cm/sec and  $v_e \approx \omega_{pi} = 2\pi \times 4$  MHz) the ion motion may be considerably different. The large amplitude waves can trap a significant number of ions resulting in asymmetric energetic tails or an average ion drift in the mean direction of wave propagation i.e., parallel to the electron drift. Although direct ion distribution function measurements have not been performed in this experiment the ion tail formation has been observed in other experiments<sup>28</sup> and in two-dimensional computer simulations.<sup>7</sup>

Fig. 14(c) shows contours of constant relative wave amplitude. In a current-free plasma the expected contours are concentric circles around the exciter since phase and group velocities point into the same direction ( $\omega \gg \omega_{ci}$ ).<sup>29</sup> In the present case the amplitude contours are not concentric with the source but are displaced in the electron drift direction. Thus, for  $\Delta z > 0$ , the cross section  $\Delta x \cdot \Delta y$  of a constant amplitude region increases initially with distance from the exciter which can be interpreted as wave amplification proportional to the increase in cross-section. A

quantitative evaluation of the plane wave growth rate would involve a calculation of the three-dimensional probe radiation pattern which has so far not been done.

Under identical conditions the test wave propagation has been investigated in the plane normal to the magnetic field and the results are shown in Fig. 15(a) - (c). Concentric circular phase fronts indicate the absence of ion drifts and electron temperature gradients in this plane. However, the amplitude contours are not completely symmetric and there are preferential directions for weak and strong amplitude decay. Similar asymmetries were noted in the noise correlation measurements and are possibly caused by minor gradients in the drift velocity.

#### Propagation and Interaction of Two Modes

While the experiments with a single ion acoustic test wave show basic dispersion and propagation characteristics the interaction among waves which will occur in the turbulent plasma can be investigated with multiple test waves of different frequencies. Three-dimensional wave-wave and wave-particle interactions are important mechanisms in establishing the stationary turbulence spectrum.<sup>3,30</sup> In current-free, unmagnetized plasmas experiments on nonlinear ion Landau damping have been reported for one-dimensional ion acoustic wave propagation<sup>31</sup> and these have recently been extended to three dimensions.<sup>27</sup> In the present work these effects are investigated in a current carrying plasma where the coupling coefficients are much larger than for  $v_d = 0$ .

As shown in Fig. 16(a) two test waves of different frequencies are launched from separate cylindrical exciter probes at different radial positions. With a third identical Langmuir probe the phase and amplitude distribution of the two oblique test waves  $(\omega_1, \vec{k}_1, \omega_2, \vec{k}_2)$  and the

nonlinear beat mode ( $\omega_3 = \omega_1 - \omega_2$ ;  $\vec{k}_3 = \vec{k}_1 - \vec{k}_2$ ) is mapped in the plane of the two exciter probes and  $\vec{v}_d$ . Interferometer traces parallel to  $\vec{v}_d$  along the symmetry axis of the two source are shown in Fig. 16(b). The ratio of the absolute wave amplitudes is  $\phi_1 : \phi_2 : \phi_3 = 1 : 2 : 1$ . Since the beat mode is destabilized by the electron drift its amplitude is comparable to that of the two test waves, i.e. about two orders of magnitude larger than in the current free case.<sup>31</sup> However, since in the present case the beat frequency is near the peak of the turbulence spectrum whose saturation amplitude is comparable to the maximum beat mode amplitude the signal-to-noise ratio is of order unity. While the frequency matching condition for the beat mode is accurately satisfied the verification of the wave vector matching requires two-dimensional interferometer data.

Fig. 17 displays the phase fronts of both excited modes and the nonlinear beat mode. For oblique propagation the beat mode is a nonresonant, driven mode with phase velocity  $v_p = (\omega_1 - \omega_2)/|\vec{k}_1 - \vec{k}_2| < (\omega_1 - \omega_2)/(|\vec{k}_1| - |\vec{k}_2|) = c_s$ . The local wave vector matching condition is found to be well satisfied as indicated by the two examples shown in Fig. 18 (points A and B are defined in Fig. 17). The wave vectors  $\vec{k}_1$ ,  $\vec{k}_2$  and  $\vec{k}_3$  are determined from the local wavelength and wave normal direction. For comparison, the expected beat wave vector  $\Delta\vec{k} = \vec{k}_1 - \vec{k}_2$  is shown together with the measured vector  $\vec{k}_3$  and the two  $\vec{k}$  values agree to within measurement accuracy. The difference in the direction of  $\vec{k}_1$ , and  $\vec{k}_2$  changes the phase velocity of the beat mode  $\omega_3/|\vec{k}_3|$  drastically. While at point A the beat mode still propagates near sound speed, at point B its phase velocity falls into the ion distribution function and the wave is subject to strong ion Landau damping. The observed amplitude distribution is shown in Fig. 19. Contours of constant amplitudes analogous to Figs. 14(c), 15(c) have been measured for the two excited waves and, as displayed in Fig. 19(a), the

amplitude product  $\phi_1 \cdot \phi_2$  has been formed since this quantity is proportional to the driving term for the beat mode. The measured amplitude distribution of the beat mode is shown in Fig. 19(b). The beat mode does not peak near point B where  $\phi_1 \cdot \phi_2$  is largest because of its slow phase velocity in this region [ $v_p = (kT_i/m_i)^{1/2}$ ]. It rather maximizes near point A where ion Landau damping is small even though the driving term  $\phi_1 \cdot \phi_2$  is reduced. Although the importance of electron over ion nonlinear Landau damping has been pointed out<sup>32,6</sup> the present observation of strong beat mode absorption when  $v_p \rightarrow (kT_i/m_i)^{1/2}$  indicates that ion Landau damping cannot be neglected in three-dimensional large amplitude ion sound turbulence.

#### IV. SUMMARY AND CONCLUSIONS

An experimental investigation into low frequency instabilities associated with the pulsed injection of a fast electron beam into a magnetized background plasma has been presented. By analyzing frequency and wavenumber spectra as well as the electron distribution function the noise has been identified as ion acoustic waves driven unstable by the return current to the injected beam. The instability evolves rapidly into strong ion sound turbulence. The three-dimensional aspect of the wave propagation has been emphasized. The low frequency cut off of the instability predicted from renormalized plasma turbulence theory has been verified in this experiment which is essentially free from boundary and collision effects. The magnetic field effects of ions are negligible and no ion cyclotron modes or lower hybrid modes have been identified. Propagation of test waves confirm the basic features of the ion acoustic instability. Nonlinear wave-wave interactions between two large test waves lead to beat modes which in turn are unstable and build up to large

amplitudes. Multiple interactions among many such modes can give rise to the observed wave turbulence. If the beat modes interact with the ions strong wave damping is encountered.

Besides the direct observations some conclusions may be drawn indirectly from the data. For example, the larger ion sound speed in the direction of the electron drift is indicative of an asymmetric ion distribution created by ion trapping in large amplitude waves. Electron trapping may also occur since the bounce frequency  $\omega_b = k(e\phi_1/m_e)^{1/2} = 4 \times 10^8 \text{ sec}^{-1}$  ( $k = 12 \text{ cm}^{-1}$ ,  $\phi_1 = 0.5 \text{ V}$ ) is far above the highest electron collision rate  $\nu_{en} = 4 \times 10^5 \text{ sec}^{-1}$ . However, since the electron Larmor radius is comparable to the wavelength trapping would mainly occur parallel to  $\vec{B}_0$ . Trapping may flatten the distribution function so as to saturate the instability<sup>33</sup>, produce asymmetric distributions and reduce the current flow. Since highly oblique waves are present many electrons can resonate with these waves ( $v_e = \omega/k_{||}$  where  $\omega < \omega_{pi}$ ,  $k_{||}/k_{\perp} < (m_e/m_i)^{1/2}$ ) but the nearly perpendicular wave electric field gives rise to only a small  $\vec{E} \times \vec{B}_0$  drift velocity ( $E/B_0 = 3 \times 10^6 \text{ cm/sec}$ ).

Although numerous observations have been presented the analysis of the beam-plasma interactions is not yet complete. Direct measurements of the ion distribution and of dc electric fields still have to be performed. Furthermore, the interaction between high frequency waves<sup>21</sup> driven unstable by the injected fast electron beam and the low frequency instabilities of the return current remain to be investigated.

#### ACKNOWLEDGEMENTS

The author wishes to thank Drs. R. W. Fredricks, W. Gekelman, W. DiVergilio and M. Caponi for helpful discussions. The expert technical assistance from Mr. W. Daley is gratefully acknowledged.

This work was supported in part by TRW Independent Research and Development Funds and in part by NASA under Contract NASW-2953.

REFERENCES

1. E. A. Jackson, Phys. Fluids 3, 786 (1960)
2. B. D. Fried and R. W. Gould, Phys. Fluids 4, 139 (1961)
3. B. B. Kadomtsev, Plasma Turbulence (Academic, New York, 1965) p. 68
4. L. M. Kovrishnykh, J. Expt. Theoret. Physics (USSR) 51, 1975,(1966)  
[Soviet Phys. JETP 24, 1210 (1967)]
5. J. A. Wesson and A. Sykes, Phys. Rev. Lett. 31, 449 (1973)
6. W. Horton, Jr., Duk-In Choi, and R. A. Koch, Phys. Rev. A. 14,  
424 (1976)
7. D. Biskamp and R. Chodura, Phys. Rev. Lett. 27, 1553 (1971), Phys.  
Fluids 16, 893 (1973)
8. M. Lampe, W. H. Manheimer, J. B. McBride, J. H. Orens, K. Papadopoulos,  
R. Shanny, and R. N. Sudan, Phys. Fluids 15, 662 (1972)
9. V. Arunasalam and S. C. Brown, Phys. Rev. 140 A, 471 (1965)
10. H. Tanaka, A. Hirose, and M. Koganei, Phys. Rev. 161, 94 (1967)
11. S. M. Hamberger and J. Jancarik, Phys. Fluids 15, 825 (1972); S. Q. Mah,  
H. M. Skarsgard, and A. R. Strilchuk, Phys. Rev. Lett. 25, 1409 (1970)
12. Y. Amagishi, Phys. Rev. Lett. 29, 405 (1972)
13. S. Watanabe, J. Phys. Soc. Japan 35, 600 (1973)
14. D. B. Fenneman, M. Raether, and M. Yamada, Phys. Fluids 16, 871 (1973)
15. A. Y. Wong, B. H. Quon, and B. H. Ripin, Phys. Rev. Lett. 30, 1299 (1973)
16. A. Mase and T. Tsukishima, Phys. Fluids 18, 464 (1975)
17. D. B. Ilić, Phys. Rev. Lett. 34, 464 (1975)

18. R. E. Slusher, C. M. Surko, D. R. Moler, and M. Porkolab, Phys. Rev. Lett. 36, 674 (1976)
19. R. Stenzel, Phys. Fluids (companion paper)
20. R. K. Fisher and R. W. Gould, Phys. Fluids 14, 857 (1971)
21. R. Stenzel, Bull. Am. Phys. Soc. 21, 1176 (1976); also submitted to J. Geophys. Res.
22. R. Stenzel and W. Gekelman, Phys. Fluids, Jan. 1976
23. S. Ichimaru, Phys. Rev. 165, 251 (1968)
24. T. Tanaka and K. Nishikawa, J. Phys. Soc. Japan 30, 894 (1971)
25. S. Watanabe and H. Tanaka, Phys. Lett. 33A, 125 (1970)
26. Y. Kawai and M. Hasegawa, J. Phys. Soc. Japan 40, 607 (1976)
27. T. Mantei, Bull. Am. Phys. Soc. 21, 1076 (1976)
28. R. D. Bengtson, K. W. Gentle, J. Jancarik, S. S. Medley, P. Nielson, and P. Phillips, Phys. Fluids 18, 710 (1975)
29. T. Ohnuma, H. Izawa, and S. Adachi; Phys. Rev. A 12, 1648 (1975)
30. V. N. Tsytovich, Usp. Fiz. Nauk 90, 435 (1966) [Sov. Phys. Uspekhi 9, 805 (1967)]
31. H. Ikezi and Y. Kiwamoto, Phys. Rev. Lett. 27, 718 (1971)
32. M. L. Sloan and W. E. Drummond, Phys. Fluids 13, 2554 (1970)
33. K. Nishikawa and C. S. Wu, Phys. Rev. Lett. 23, 1020 (1969)

FIGURE CAPTIONS

- Fig. 1. Fast sweeps of Langmuir probe voltage  $V_p$  (top trace, 5 V/div.) and current  $I_p$  (bottom trace, 0.5 mA/div.) during the injection of an electron beam ( $V_b = 10$  V,  $t_s = 100$   $\mu$ sec). Large amplitude, incoherent fluctuations in the electron saturation current are the result of the return current driven ion sound instability. The plane probe (No. 2 in Fig. 1, Ref. 19) is located at a distance  $\Delta z = 7$  cm from the anode with its surface normal parallel to the injected beam velocity. Krypton  $2 \times 10^{-4}$  Torr,  $t_a = 24$  msec,  $B_0 = 75$  G.
- Fig. 2. Frequency spectrum of an rf resonance cone signal excited in the presence of the ion acoustic instability. Density fluctuations modulate the cone angle and generate the sideband to the applied monochromatic rf signal at  $\omega_0/2\pi = 90$  MHz.
- Fig. 3. Top trace: beam voltage (20 V/div.); bottom trace: electron saturation current to a cylindrical Langmuir probe located at  $\Delta z = 7$  cm from the anode. Superposition of 8 exposures shows the development of the instability from coherent growth to turbulence at  $t = 15$   $\mu$ sec after turn-on of current. Probe bias +12 V,  $t_a = 24$  msec, Krypton  $2.3 \times 10^{-4}$  Torr.
- Fig. 4. Frequency spectrum of the saturated current-driven ion acoustic instability. The noise amplitude is the fluctuating electron saturation current of a cylindrical Langmuir probe Fourier transformed in a spectrum analyzer and sampled at  $t_s$ . The absolute peak density fluctuation level at  $\omega/\omega_{pi} = k\lambda_D = 0.2$  is  $\delta n_e/n_e \approx 20\%$ . The high frequency fall-off is  $\delta n_e/n_e \propto f^{-2.5}$ . The noise peak is not determined by collisions ( $\nu_{in} = 5 \times 10^3$  sec $^{-1}$ ) or

finite geometry but scattering of electron by waves. Krypton  
 $2.3 \times 10^{-4}$  Torr,  $z = 7$  cm.

Fig. 5(a) Unnormalized cross correlation function for delay time  $\tau = 0$   
 vs. position  $\Delta z$  along  $\vec{B}_0$ . The half width ( $\Delta z_{1/2} = 1$  mm) gives  
 a measure for the width of the wavenumber spectrum.

(b) Contours of constant correlation signal for  $\tau = 0$  in the hori-  
 zontal plane  $\Delta z \parallel \vec{B}_0$ ,  $\Delta y \perp \vec{B}_0$ . The stationary reference probe  
 is located at  $\Delta y = \Delta z = 0$ . Elliptical contours indicate angular  
 spread of wave propagation with respect to the preferred  
 direction parallel to  $\vec{v}_d$ . Subsequent data (Fig. 7) show that  
 propagation out of the plane also exhibits preferred directions.  
 $t_a = 24$  msec,  $z = 7$  cm, Kr,  $2.3 \times 10^{-4}$  Torr.

Fig. 6(a) Cross correlation signal at different delay times  $\tau$  vs. position  
 $\Delta z$  ( $\Delta x, \Delta y = \text{const.}$ ) The shift of the correlation peaks with  
 delay time indicates a unique direction of wave propagation.  
 The amplitude decay gives a measure for the correlation length  
 of waves ( $\Delta z_c = 50\lambda_D$ ).

(b) Time-position diagram for the correlation function (maximum A,  
 minimum B). Sign and magnitude of the trajectory slope show that  
 waves propagate at sound speed parallel to  $\vec{v}_d$ .

Fig. 7(a) Cross correlation signal vs. position  $\Delta x$  across  $\vec{B}_0$  normal to  
 the horizontal plane of Fig. 5(b).

(b) Contours of constant cross correlation amplitude in the x-y  
 plane normal to  $\vec{B}_0$  and orthogonal to the plane of Fig. 5(b).  
 Center region  $\Delta y = \pm 0.5$  mm was inaccessible for measurements.  
 Noncircular contours indicate asymmetric azimuthal wave propa-  
 gation. Preferred direction is normal to the major axes of

the elliptical contours. In those directions correlation function half-widths are comparable to those along  $\vec{v}_d$ .

$$t_a = 24 \text{ msec}, z = 7 \text{ cm.}$$

Fig. 8. Cross correlation signal vs. distance  $\Delta x$  across  $\vec{B}_0$  for different delay times  $\tau$ . In contrast to Fig. 6(a) the correlation function splits and moves to both sides indicating wave propagation in opposing directions across  $\vec{B}_0$ . Due to oblique propagation the phase velocity ( $v_p = 2.2 \times 10^5$  cm/sec) exceeds sound speed; different correlation lengths reflect azimuthal asymmetries.

Fig. 9. Schematic view of an array probe for observing turbulence in real time and space. The block diagram indicates the method for recording, with single shot exposures, six simultaneous traces of density fluctuations.

Fig. 10. Single exposure of simultaneous traces of density fluctuations vs. time of six probes aligned in an array across  $\vec{B}_0$  as sketched on the right. Two time markers applied to all channels provide for an absolute time reference and scale calibration. Perturbation labelled "a" at bottom represents a growing wave propagating at sound speed ( $c_s = 1.4 \times 10^5$  cm/sec) in the direction from probe #6 to #1 perpendicular to  $\vec{v}_d$ . Perturbation "b" is a decaying wave. Growth and decay scale lengths are  $\Delta r_c \approx 5$  mm corresponding to approximately two wavelengths; such short correlation lengths are characteristic for strong turbulence. Perturbations "c" and "d" propagate with velocity  $v > c_s$  oblique to the array axis. Amplitude decay along the wave crest is smaller than in propagation direction. Kr  $2.3 \times 10^{-4}$  Torr,  $z = 7$  cm,  
 $(\delta I_p / I_p)_{\max} = 25\%$ .

Fig. 11(a) Test wave interferometer signal vs. time at a constant frequency, applied amplitude and probe separation ( $f = 3$  MHz,  $\Delta z = 12$  mm). Propagation is along  $\vec{v}_d$ . Timing of current pulse is indicated on top. Lower trace is the boxcar sampling pulse. Oscillations reflect wavenumber changes due to temperature and density changes. Note build-up of large amplitude waves during the current flow and 20 dB smaller signals after current turn-off.

(b) Interferometer trace vs. position at a fixed sampling time.

Nearly undamped submillimeter ion acoustic waves are excited from a line source (0.13 mm diam, 2.5 mm length) in the direction of the electron drift.

Fig. 12. Frequency spectrum of the applied signal (a) and of the received ion acoustic wave during beam injection (b) and after end of beam pulse (c) (arbitrary vertical scales;  $t_p$  is the beam pulse length). Wave propagation in a time-varying medium gives rise to frequency shifts unrelated to Doppler effects or wave-wave interactions.

Fig. 13. Test wave dispersion  $\omega$  vs  $k_{||}$  for propagation in the direction of the electron drift.  $f_{pi} \approx 3$  MHz,  $\lambda_D^{-1} = 135$  cm<sup>-1</sup>,  $k_r 2.3 \times 10^{-4}$  Torr,  $z \approx 7$  cm.

Fig. 14(a) Test wave interferometer trace vs. axial position along  $\vec{B}_0$  at a radial distance  $\Delta x = 2$  mm from the isotropic exciter at  $\Delta x = \Delta y = \Delta z = 0$ . The preferred propagation in the direction of the electron drift is evident.

(b) Contours of constant phases of the test wave in the plane  $\Delta x$  ( $\perp \vec{B}_0$ ),  $\Delta z$  ( $\parallel \vec{B}_0$ ). Circles are maxima, crosses are minima of interferometer

traces. Note asymmetry in parallel wavelength with respect to the electron drift  $\vec{v}_d$  indicating the presence of an ion drift parallel to  $\vec{v}_d$  created by ion trapping in large amplitude waves along  $\vec{v}_d$ .

(c) Contours of constant relative wave amplitude. The excentricity of the contours with respect to the exciter at the origin indicates initial amplification of the diverging wave in the half space centered along  $\vec{v}_d$ .  $k_r 2.3 \times 10^{-4}$  Torr,  $t_a = 24$  msec,  $z = 7$  cm.

Fig. 15. Test wave properties in a plane orthogonal to that shown in Fig. 14 and normal to  $\vec{v}_d \parallel \vec{B}_0$ . (a) Interferometer traces vs  $\Delta x (\perp \vec{B}_0)$  at different orthogonal positions  $\Delta y (\perp \vec{B}_0)$ . (b) Phase fronts of the test wave launched at  $\Delta x = \Delta y = 0$ . (c) Contours of constant relative wave amplitude. Symmetric phase fronts indicate absence of ion drifts; asymmetric amplitude contours, previously noted in Figs. 7 and 8, are possibly due to radial gradients in  $v_d$ . Parameters as in Fig. 14.

Fig. 16(a) Schematic probe arrangement for exciting two oblique large amplitude test waves in order to investigate their nonlinear interaction. (b) Interferometer traces of the two excited modes ( $\omega_1, \omega_2$ ) and the beat mode ( $\omega_3 = \omega_1 - \omega_2$ ) vs. axial position along  $\vec{v}_d$  at equal radial spacing between the two exciters. Since the off-resonant beat mode is destabilized by the electron drift its amplitude is comparable to that of the normal modes (amplitude ratio  $\phi_1 : \phi_2 : \phi_3 = 1 : 2 : 1$ ).  $t_a = 24$  msec,  $z = 7$  cm, exciter probe separation  $\Delta r = 3$  mm.

Fig. 17. Phase fronts of the two test waves and their beat mode in a plane defined by radial and axial coordinates,  $\Delta r$ ,  $\Delta z$  respectively. The exciters are located at  $\Delta z = 0$ ,  $\Delta r_1 = -2$  mm,  $\Delta r_2 = +4$  mm. Points A and B are arbitrary locations at which wave vector matching will be demonstrated (see Fig. 18).  $z = 7$  cm,  $t_a = 24$  msec,  $k r \approx 2 \times 10^{-4}$  Torr.

Fig. 18. Examples of wave vector matching at two locations in Fig. 17. The three vectors  $\vec{k}_1$ ,  $\vec{k}_2$  and  $\vec{k}_3$  are determined from local wavelength and wave normal directions. The expected difference wave vector  $\Delta\vec{k} = \vec{k}_1 - \vec{k}_2$  agrees with  $\vec{k}_3$  to within measurement accuracy. The phase velocity of the beat mode is, in general, smaller than sound speed  $c_s$  and can fall into the ion distribution function (B). Parameters as in Fig. 17.

Fig. 19(a) Contour map of the product of the two normal mode amplitudes (arbitrary units).

(b) Contours of constant relative amplitude of the beat mode. Although the driving modes  $\phi_1 \cdot \phi_2$  are largest near point B the beat mode amplitude maximizes elsewhere since ion Landau damping is strong near B. Parameters as in Fig. 17.

ORIGINAL PAGE IS  
OF POOR QUALITY

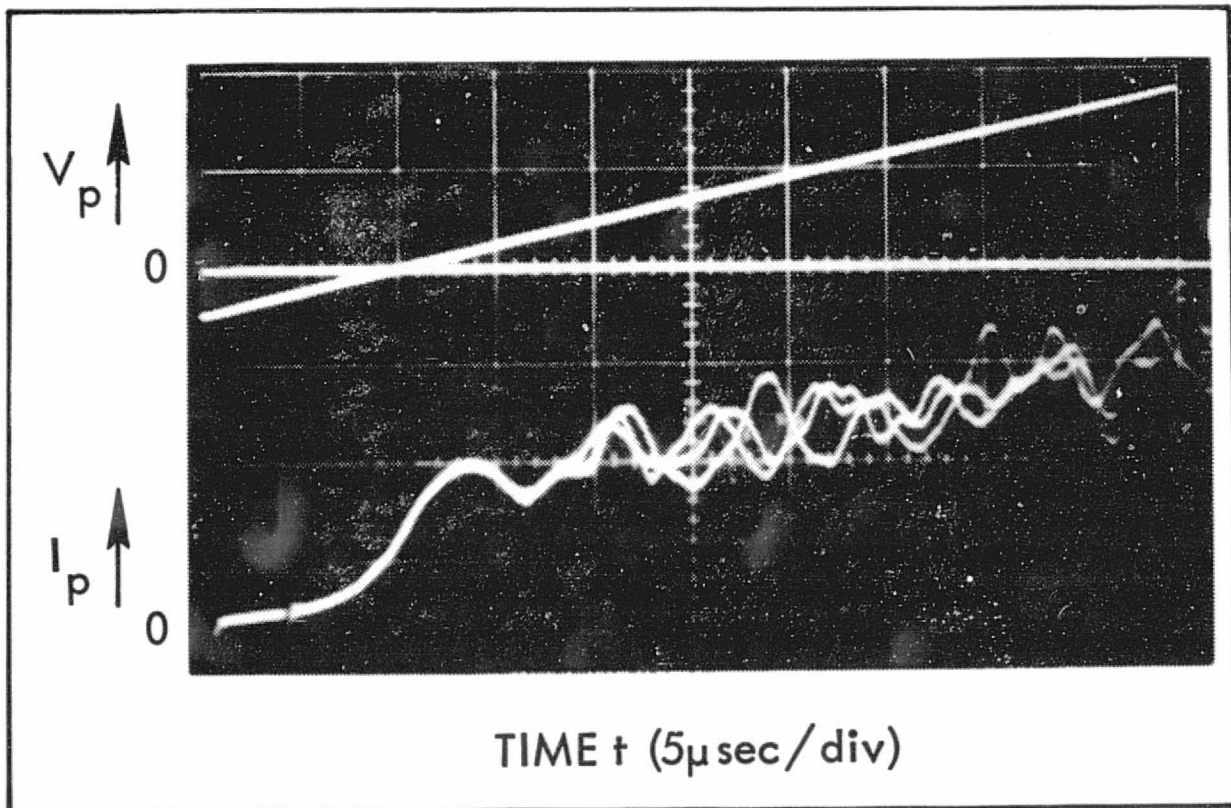


Fig. 1

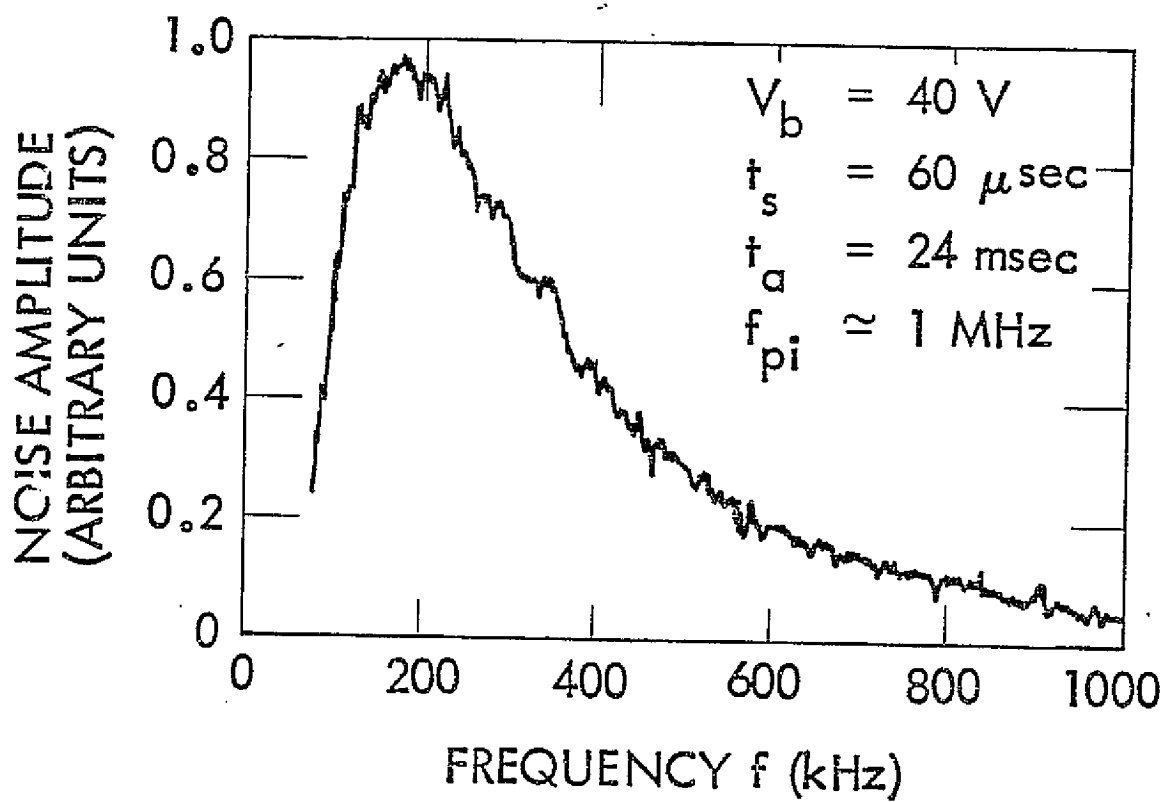


Fig. 2a

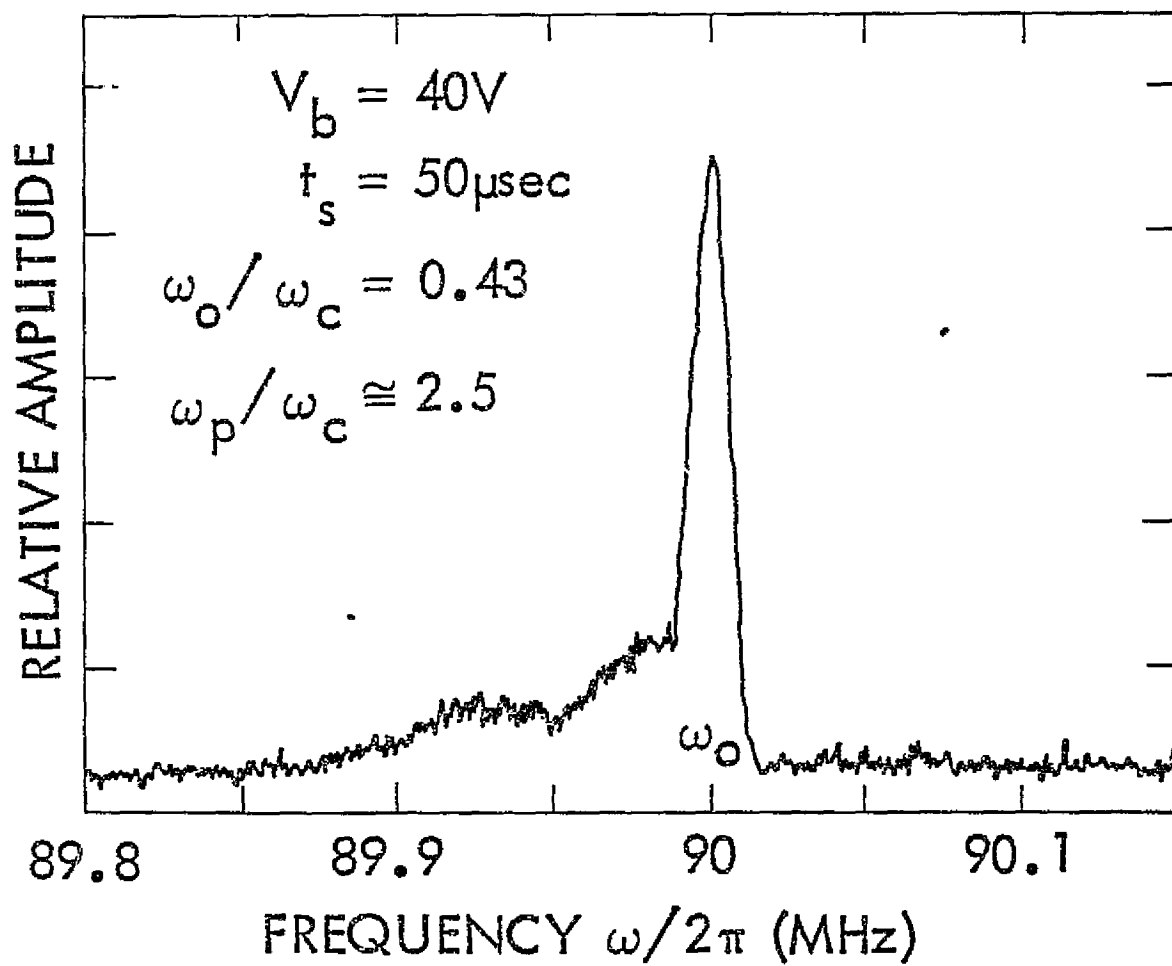


Fig. 2b

ORIGINAL PAGE IS  
OF POOR QUALITY

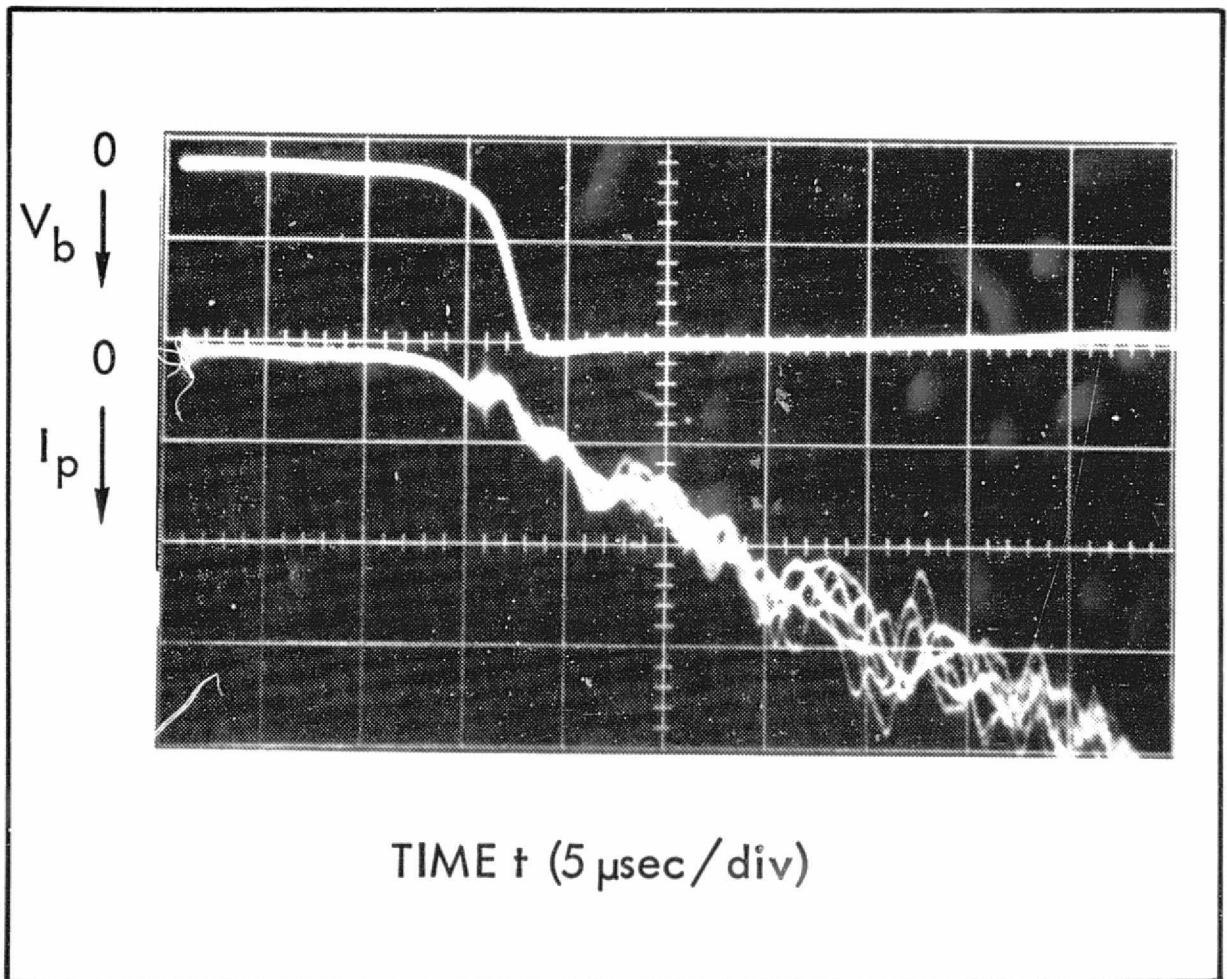


Fig. 3

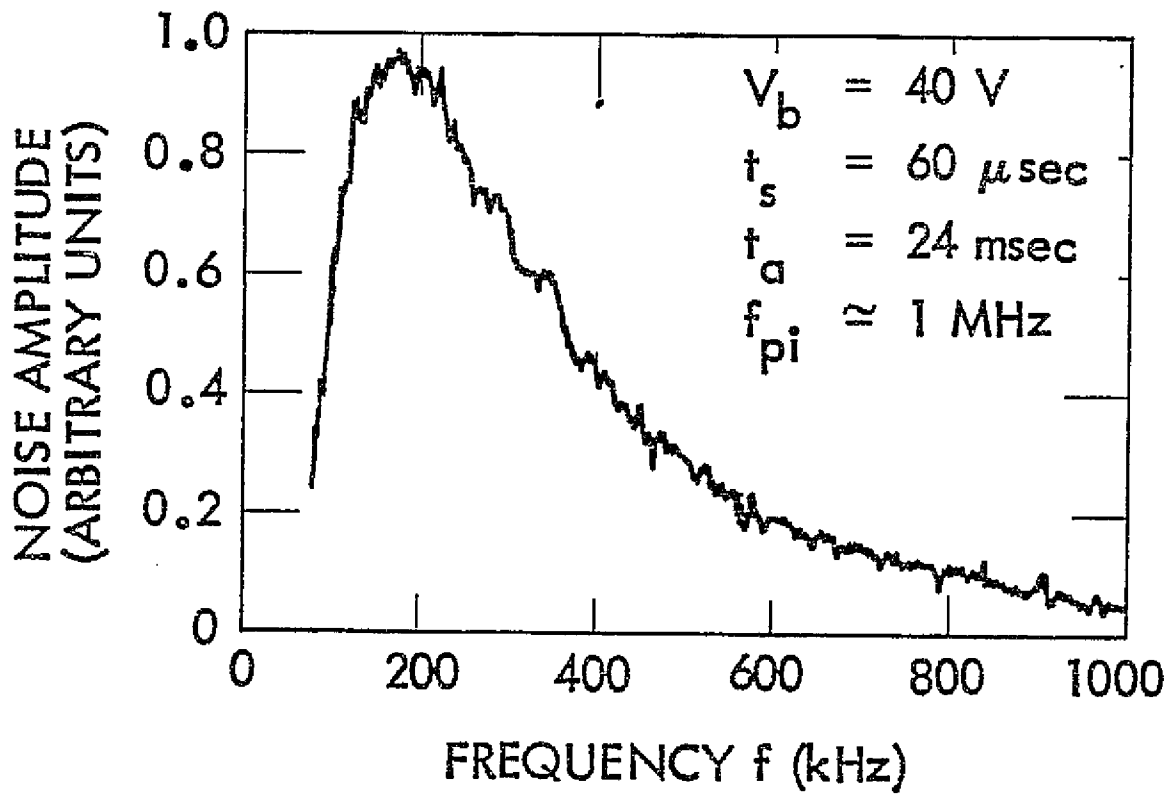
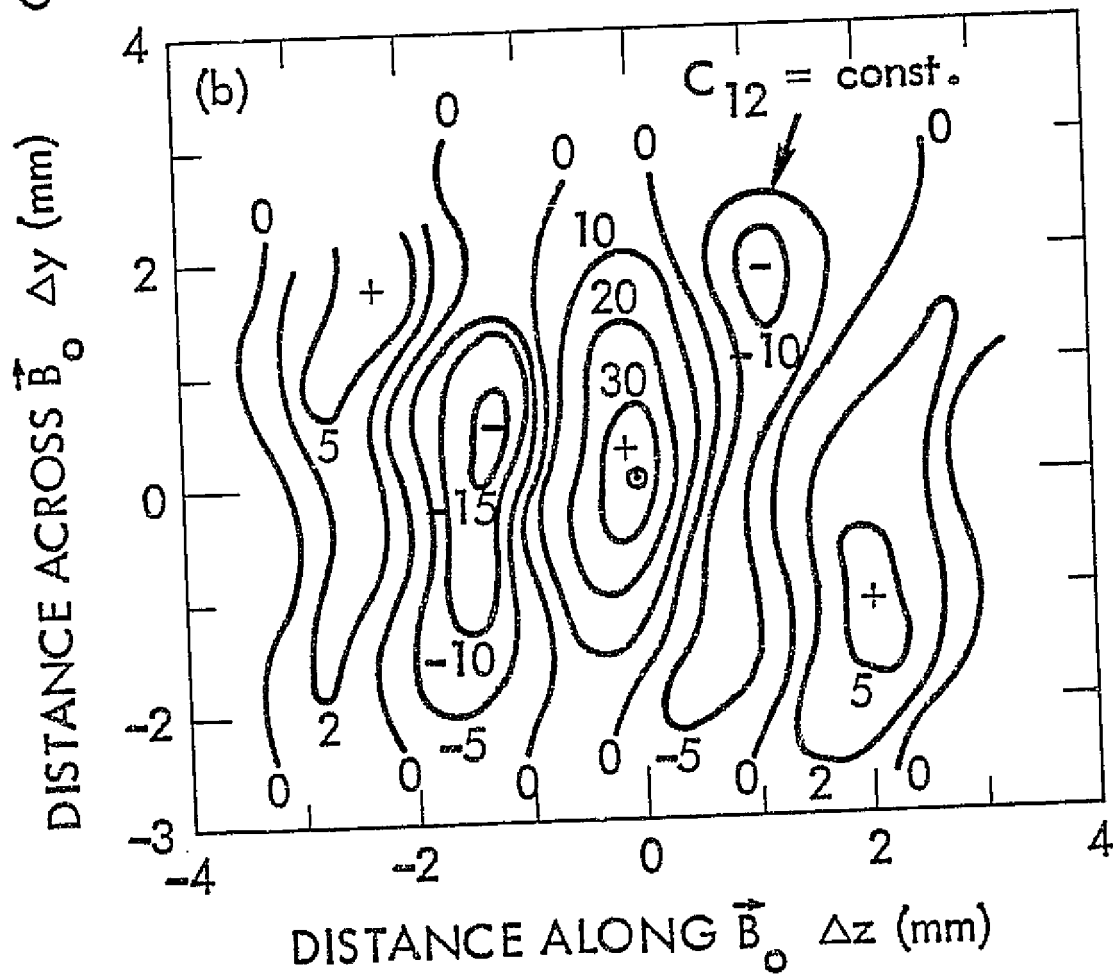
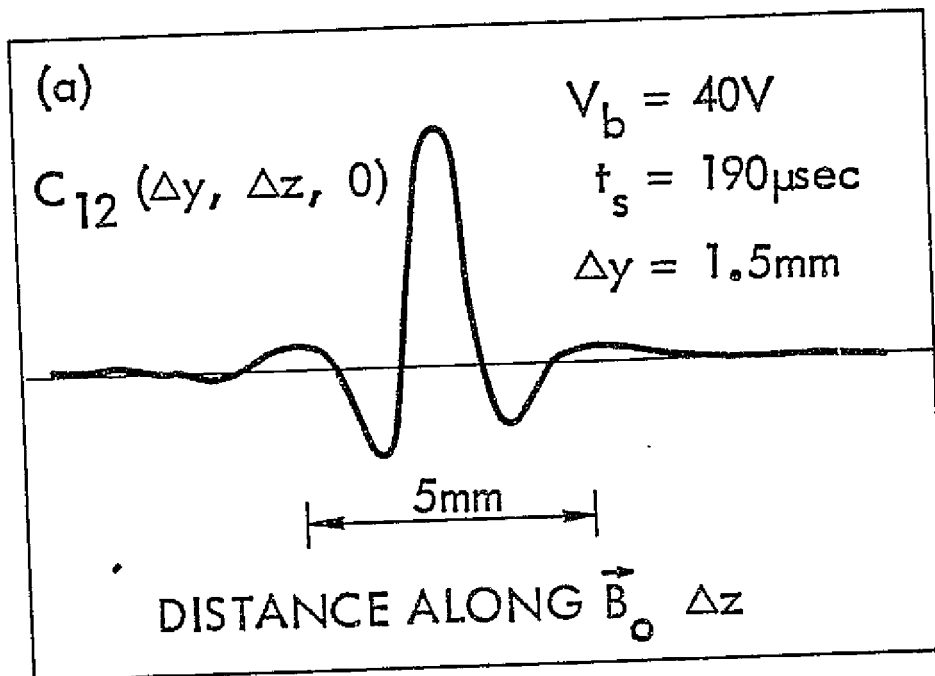


Fig. 4

CORRELATION FUNCTION



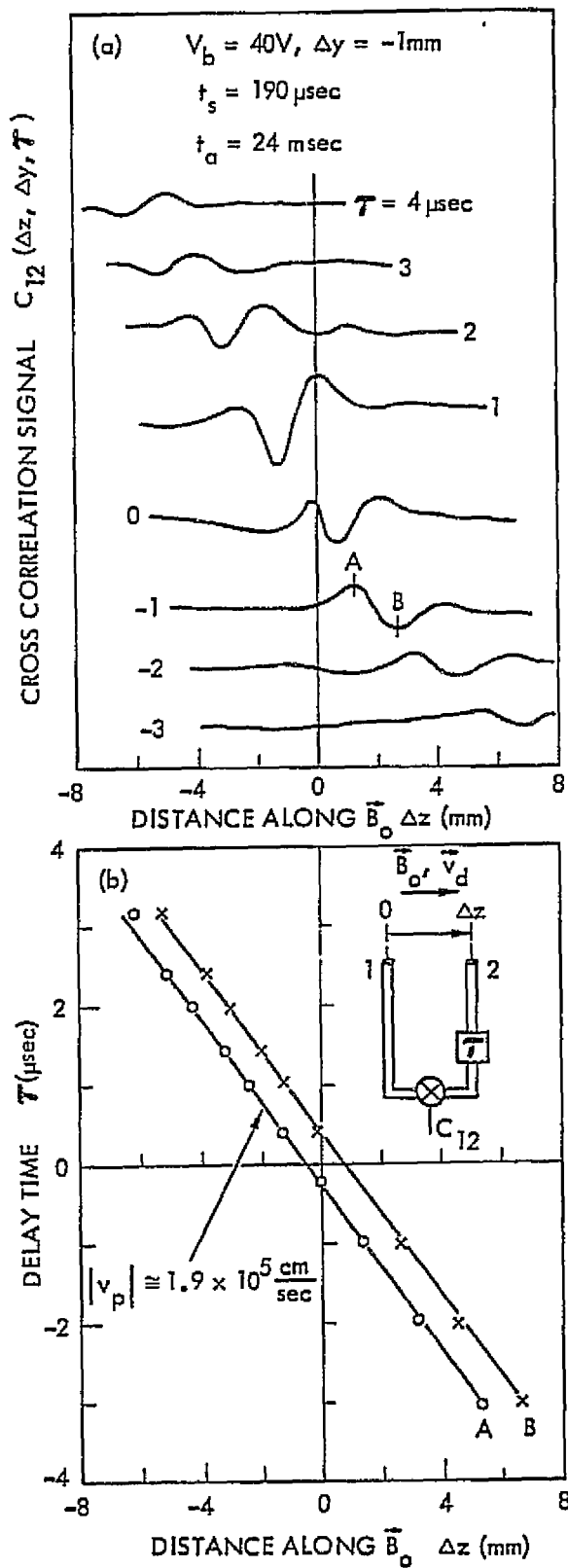


Fig. 6

CROSS CORRELATION FUNCTION  
DISTANCE ACROSS  $\vec{B}_0$   $\Delta y$  (mm)

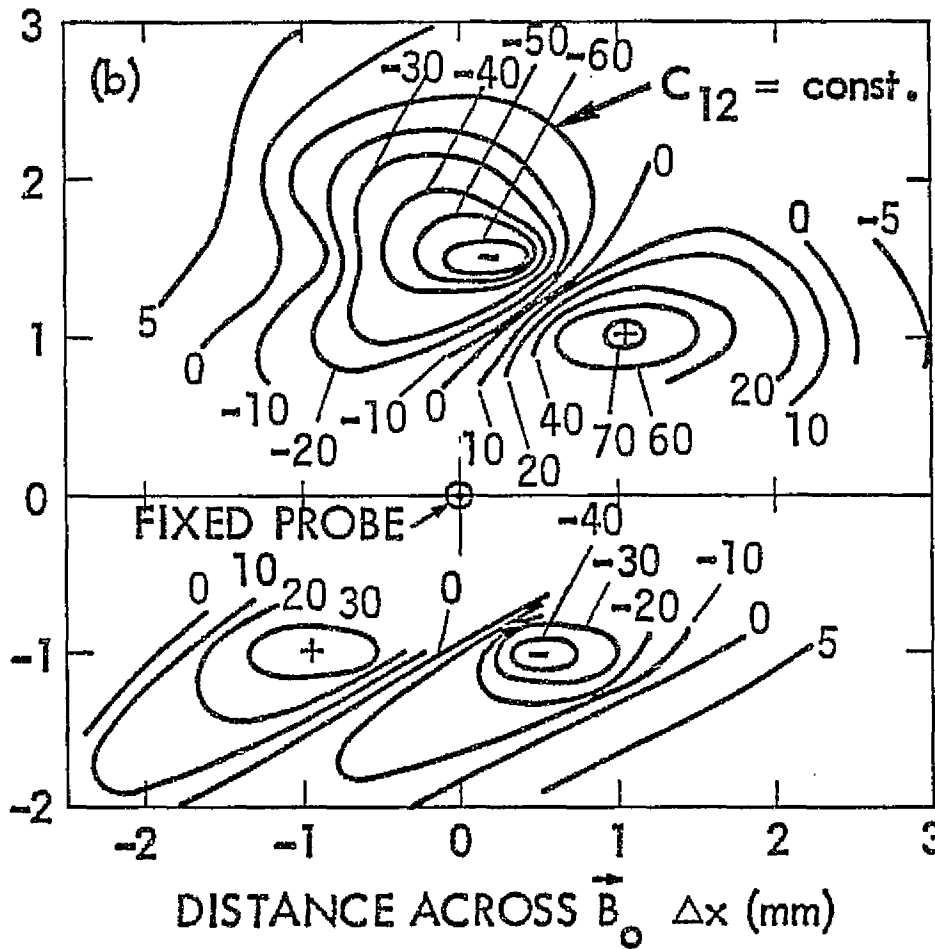
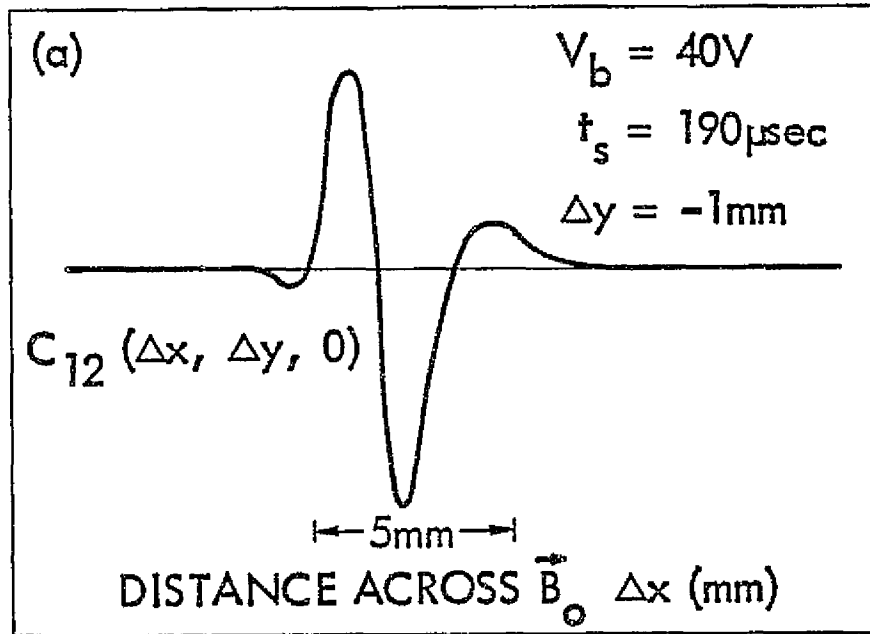


Fig. 7

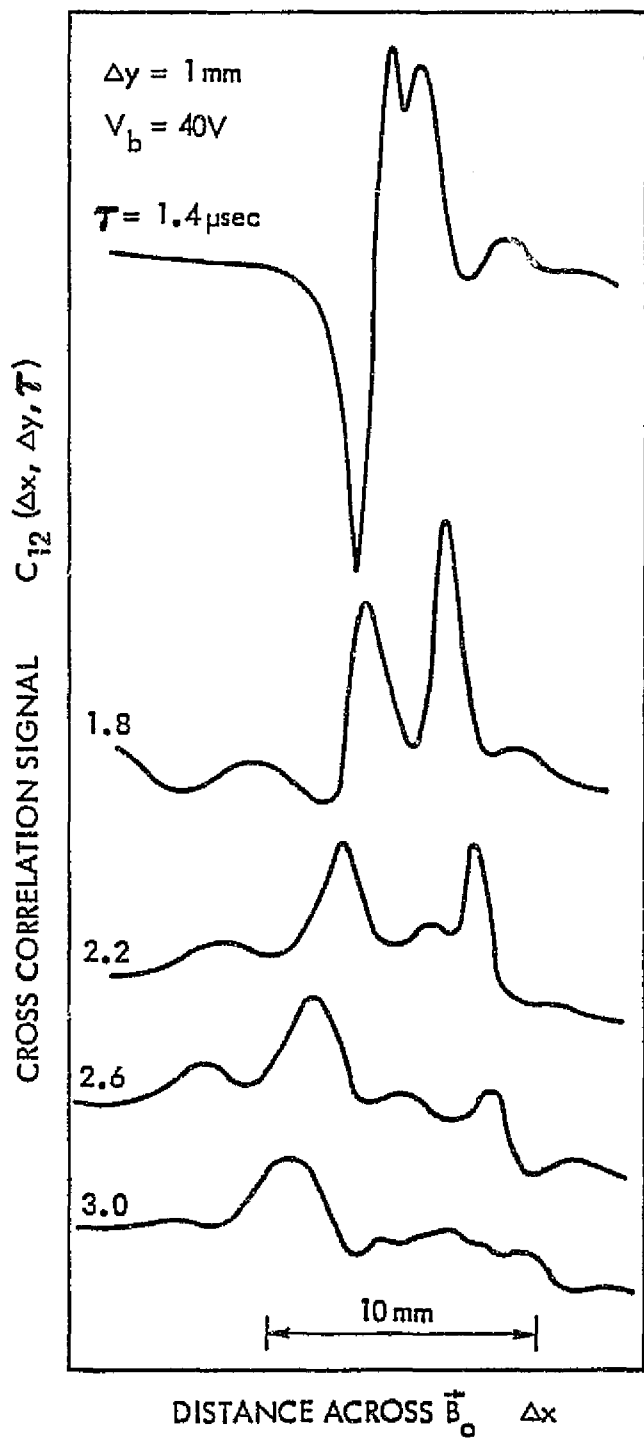


Fig. 8

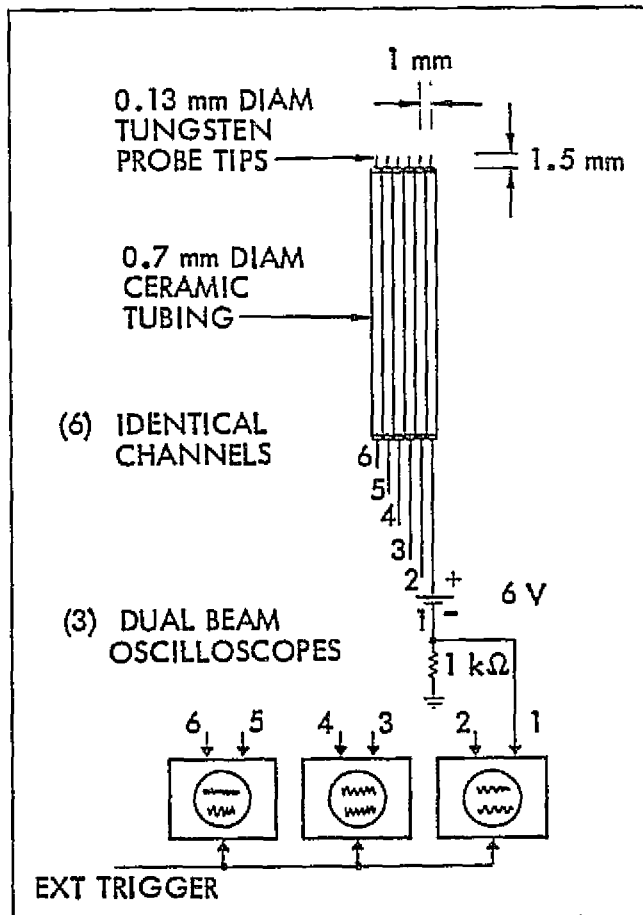


Fig. 9

ORIGINAL PAGE IS  
OF POOR QUALITY

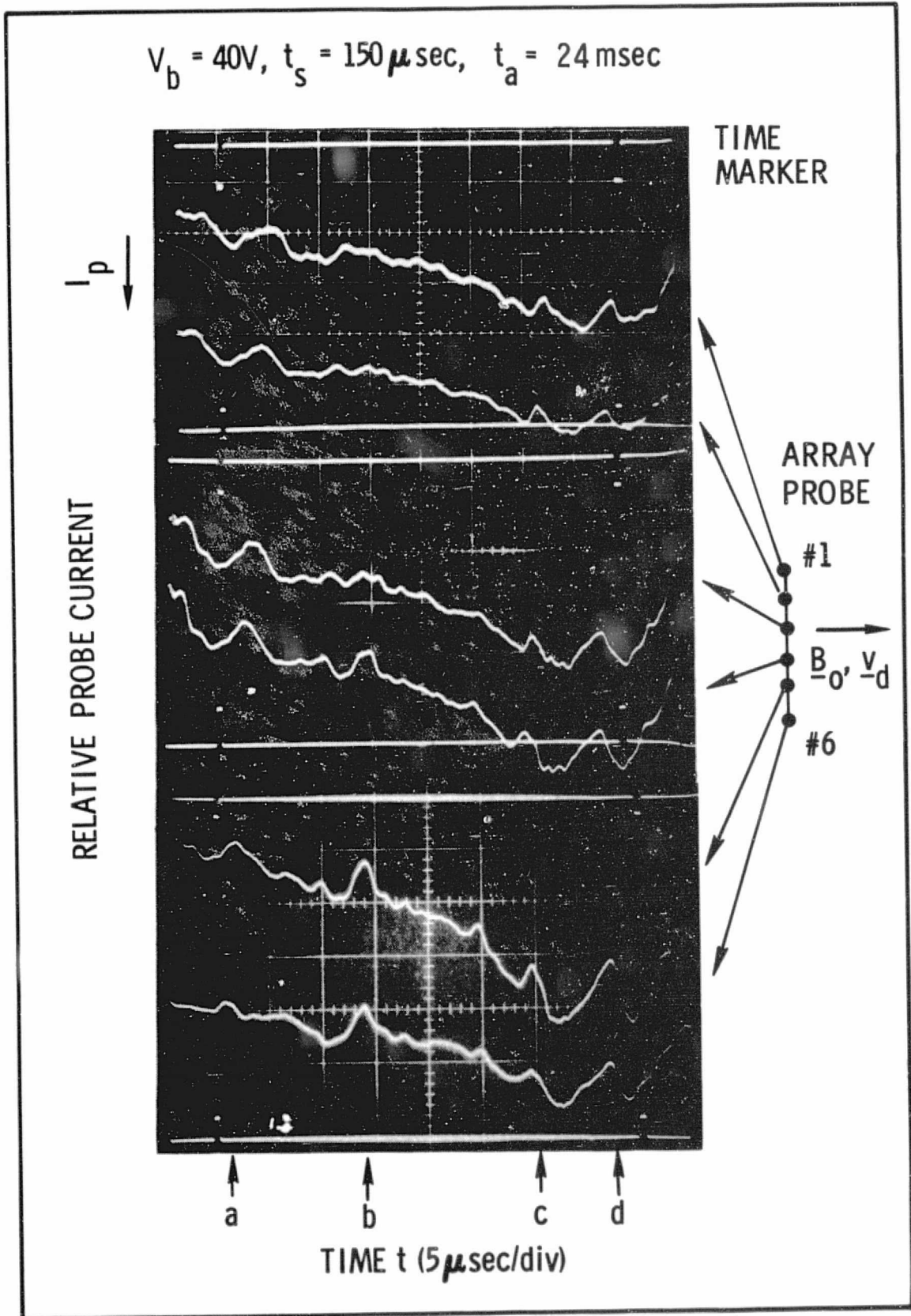


Fig. 10

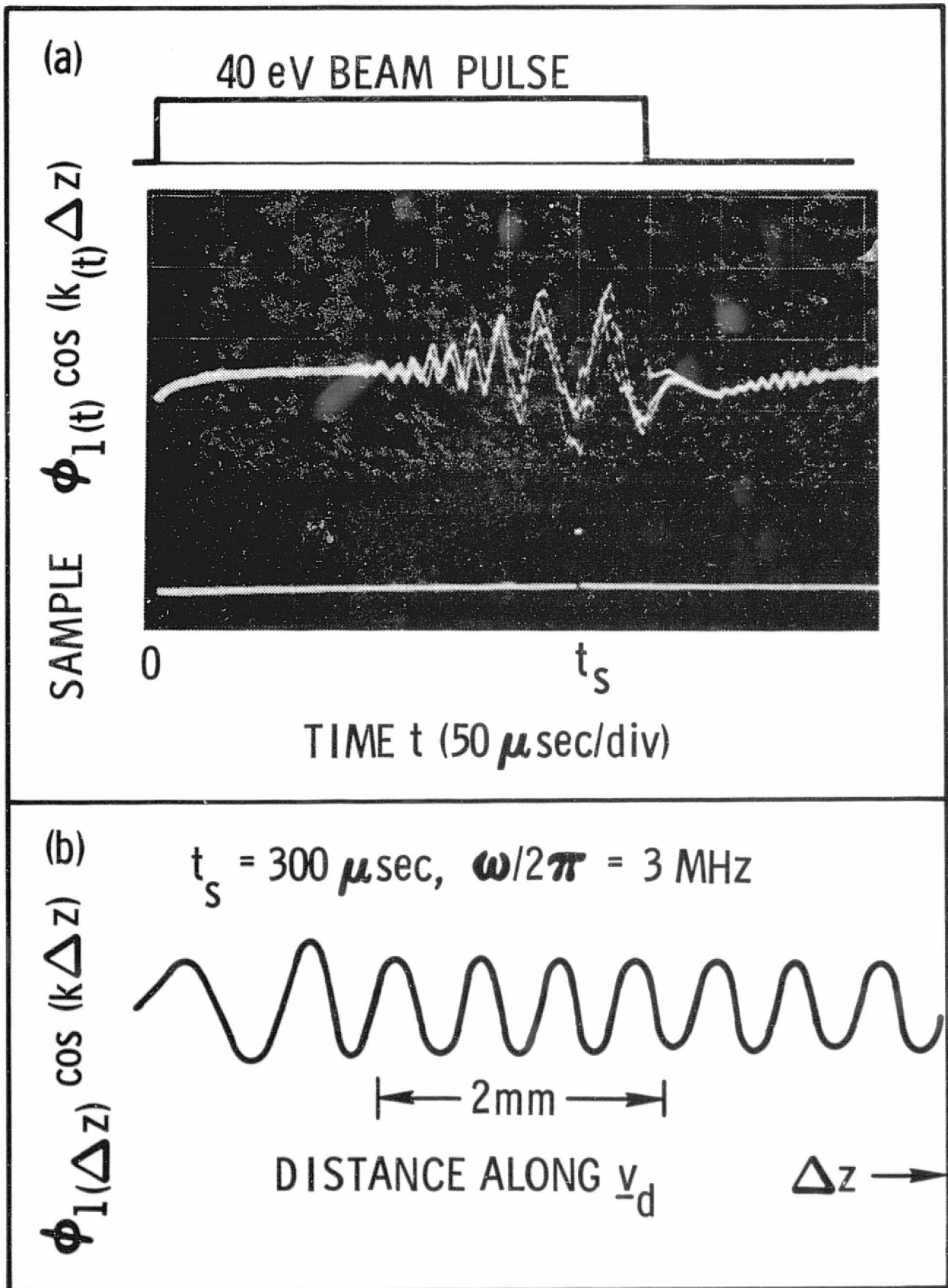


Fig. 11

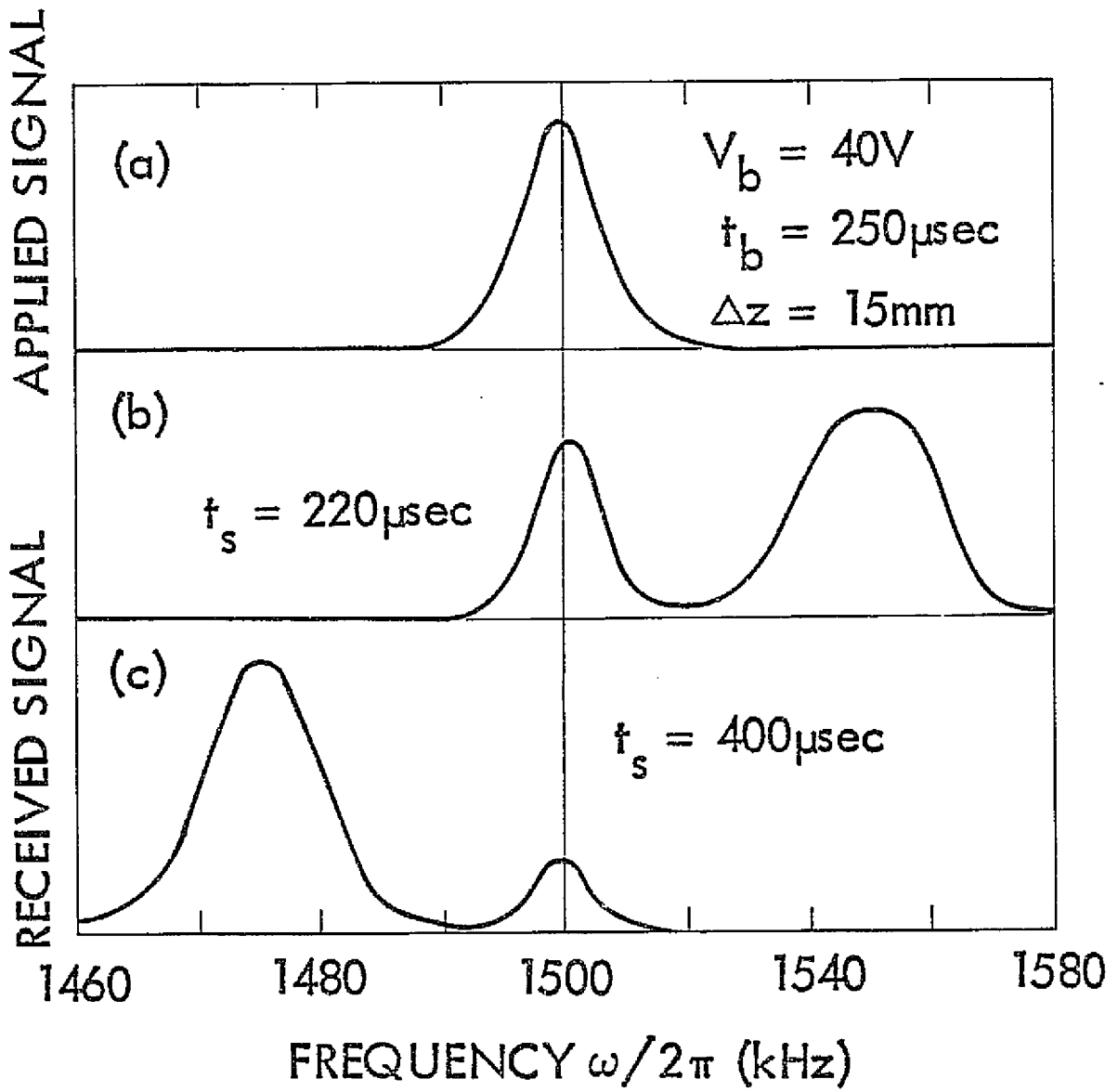


Fig. 12

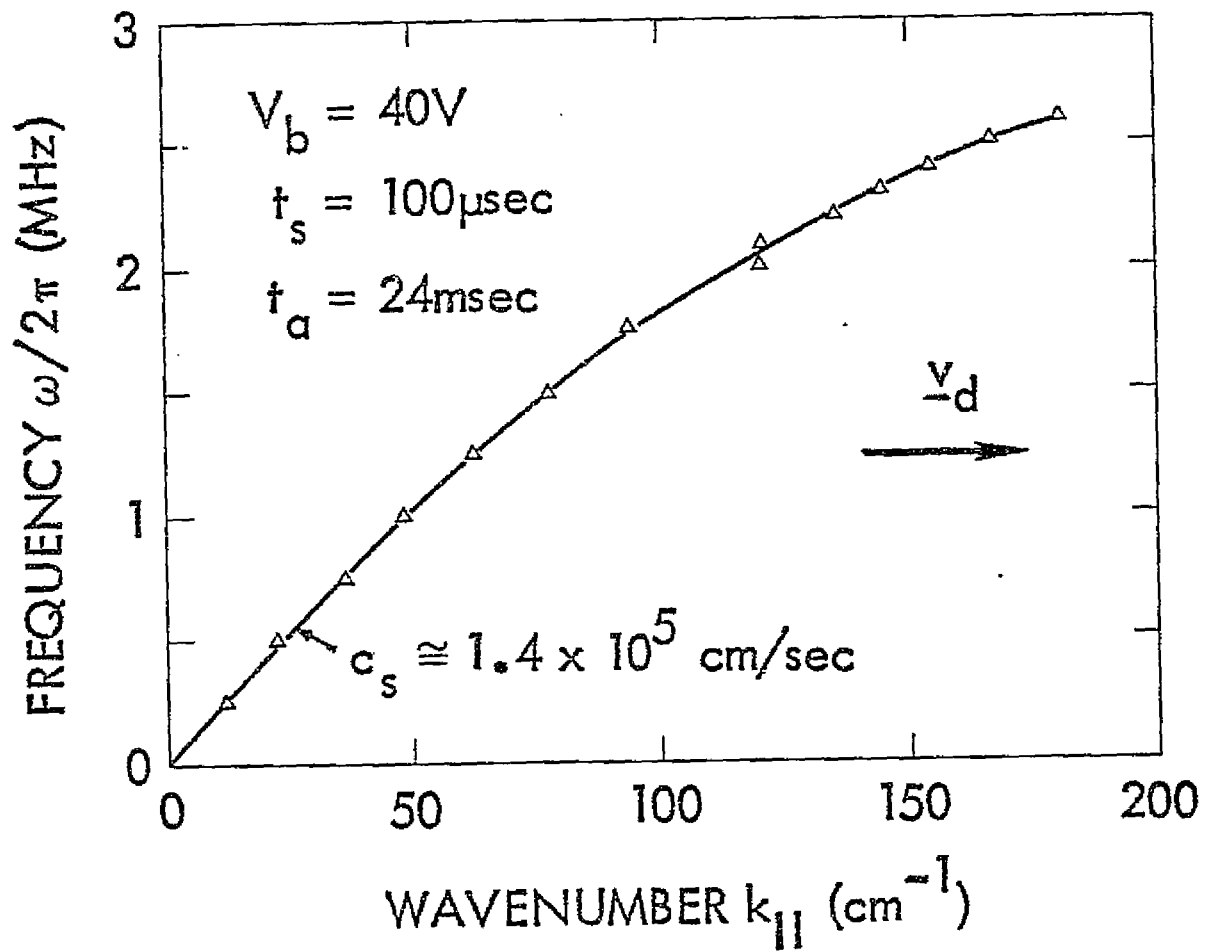


Fig. 13

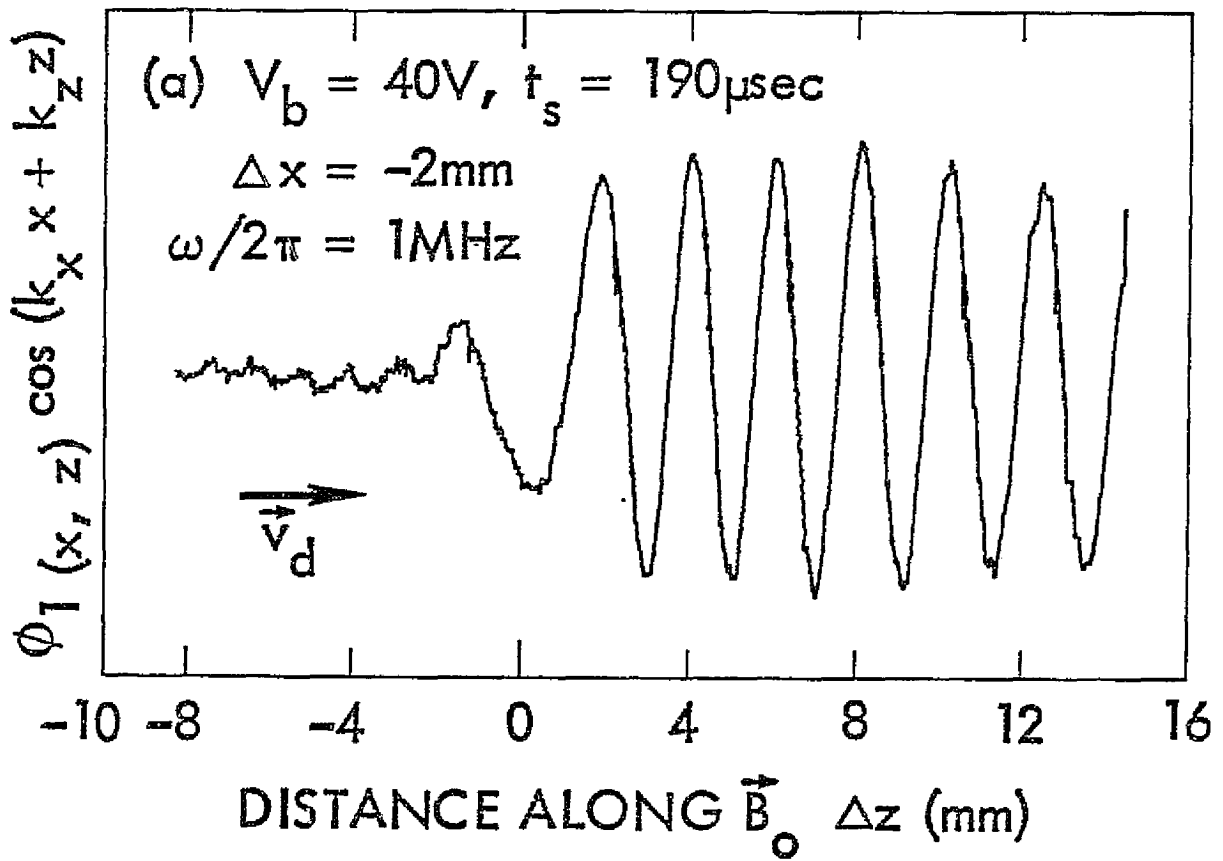


Fig 14(a)

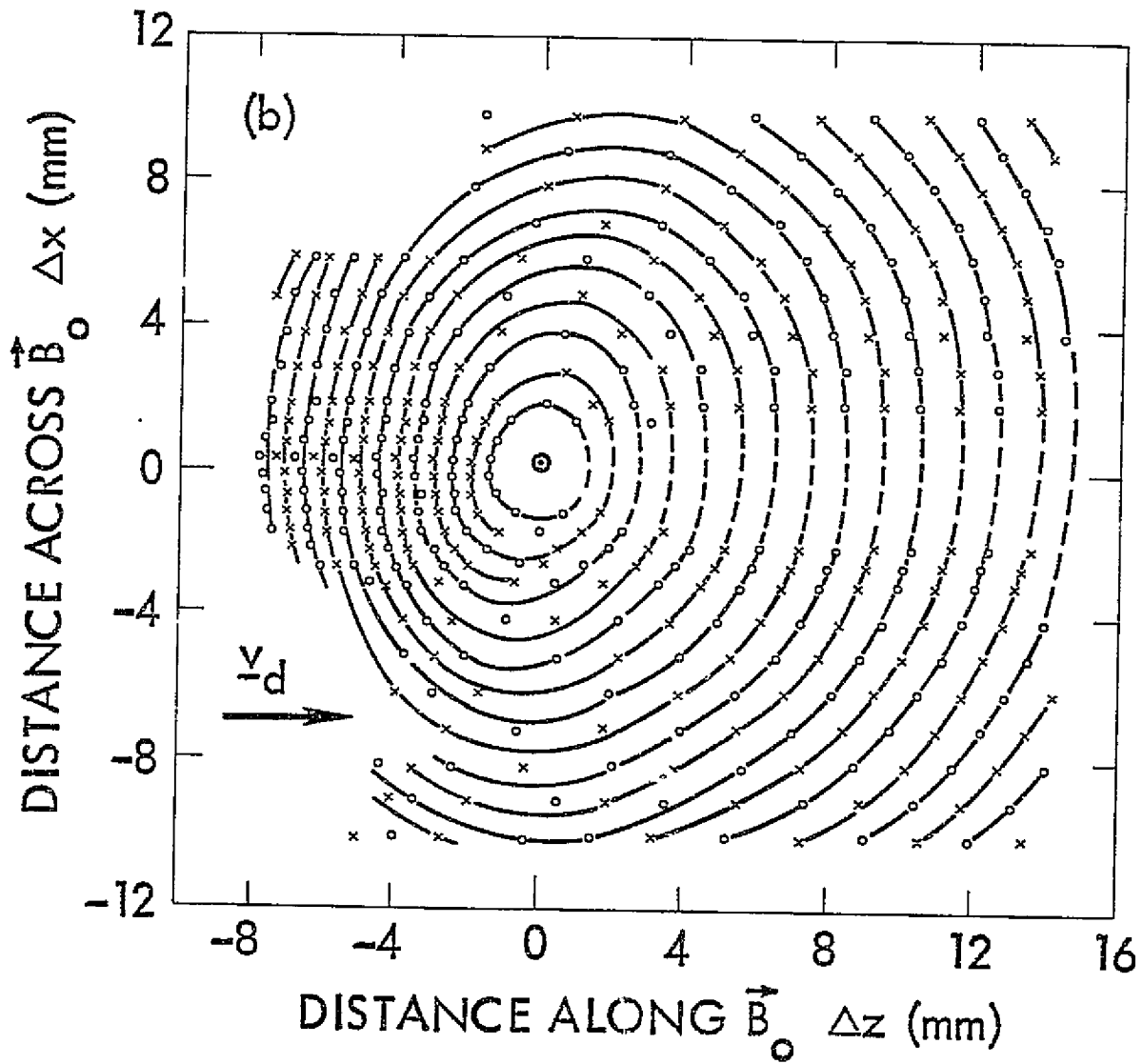


Fig 14(b)

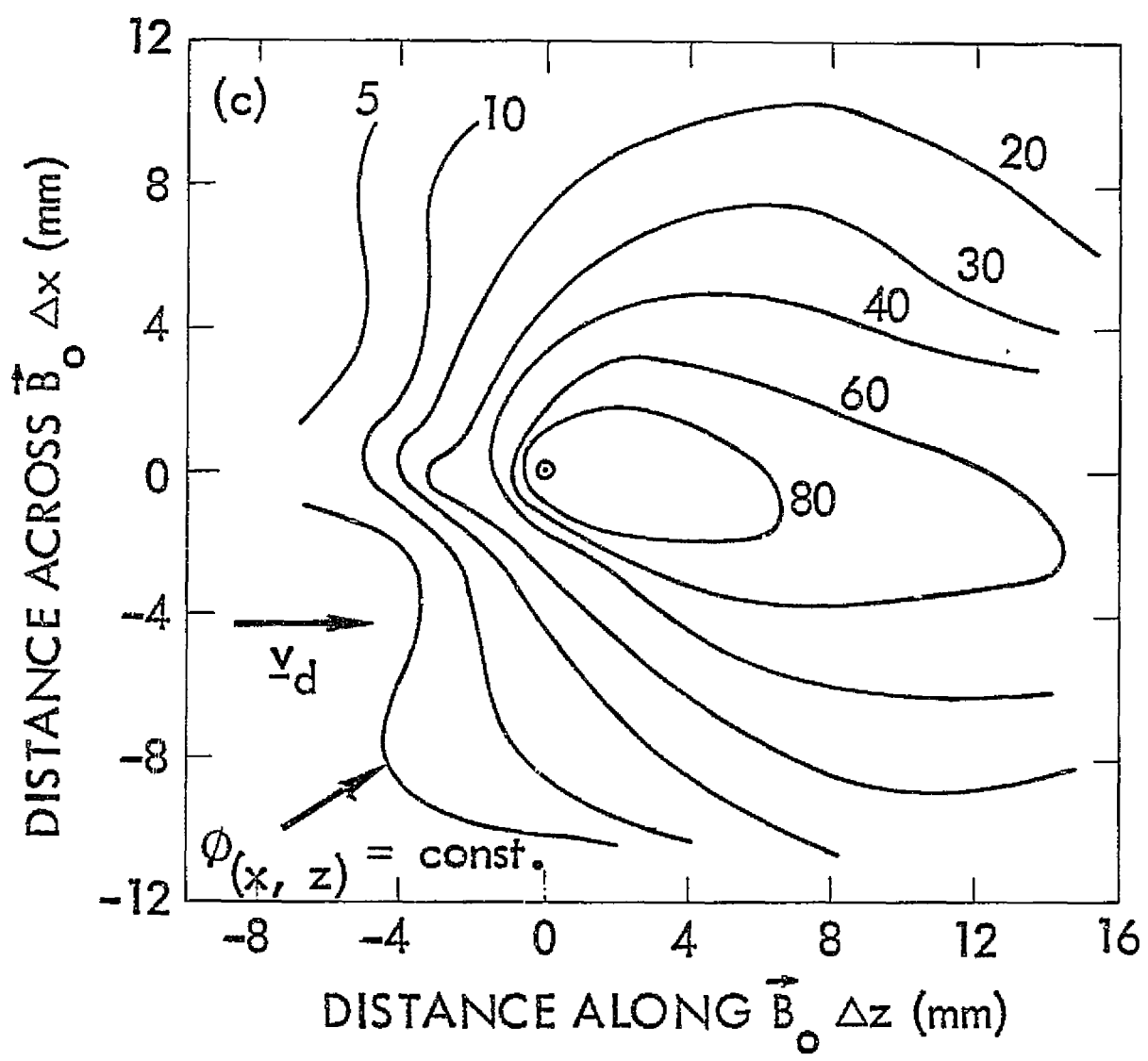


Fig 14(c)

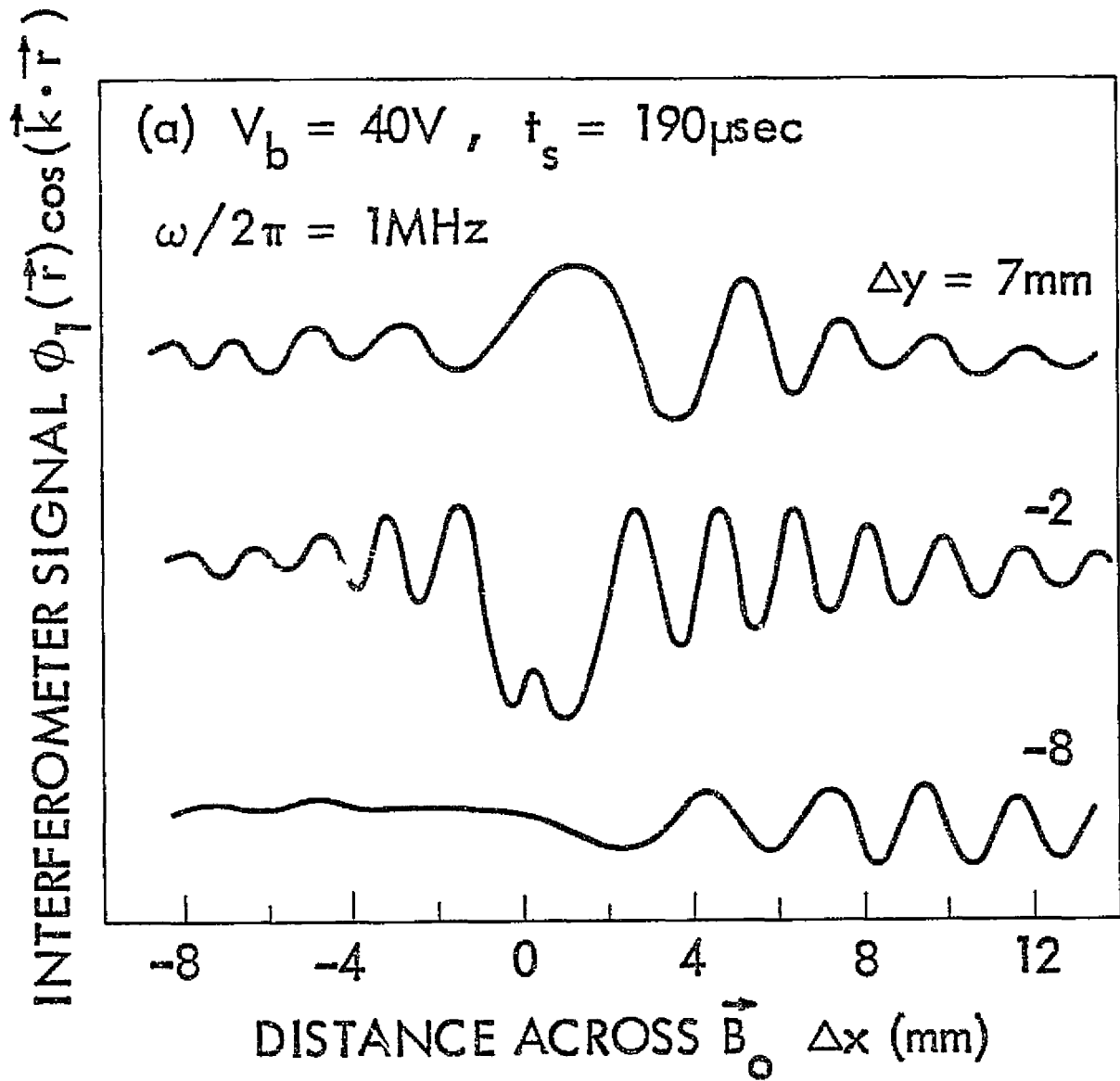


Fig 15(a)

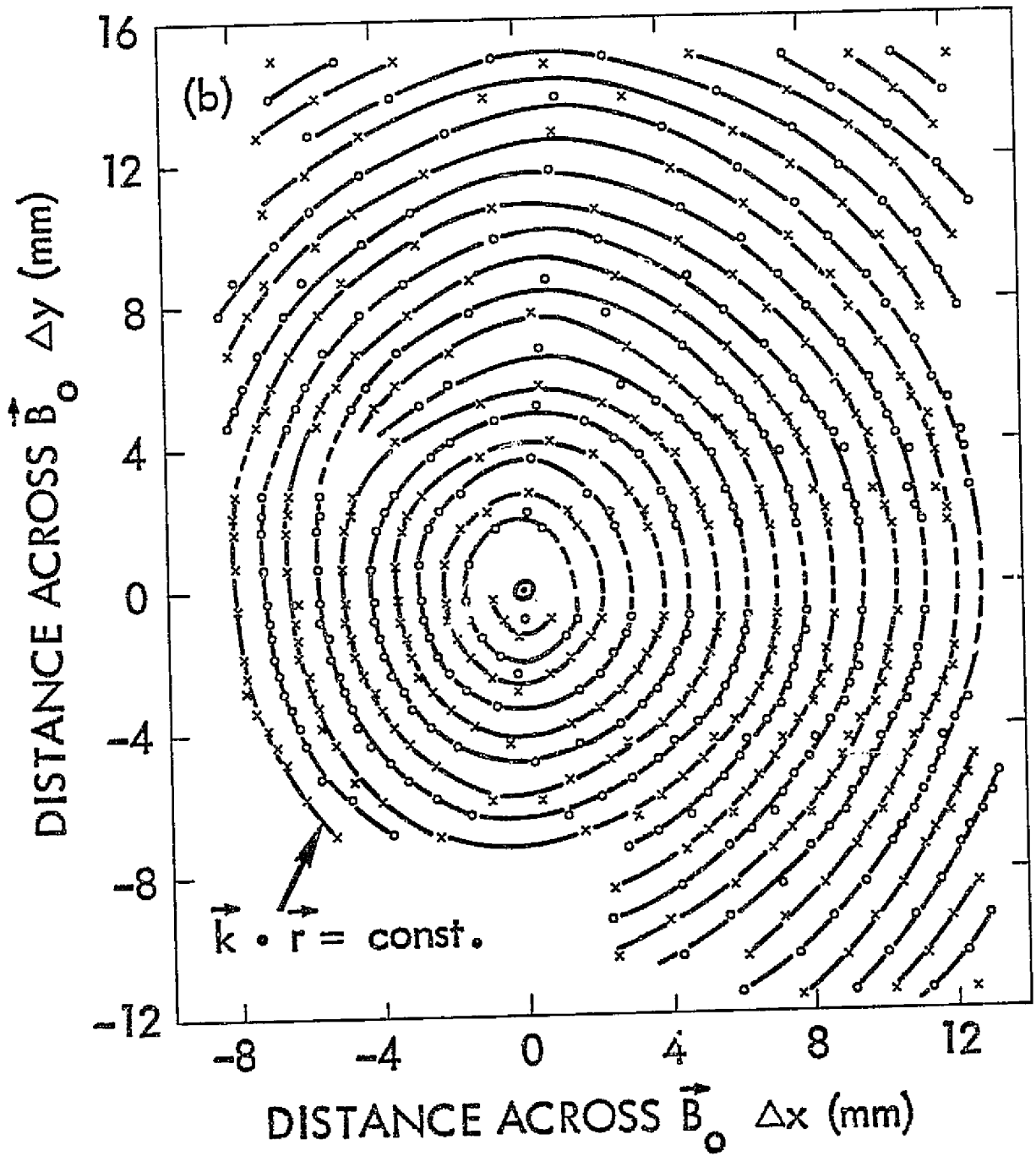


Fig 15(b)

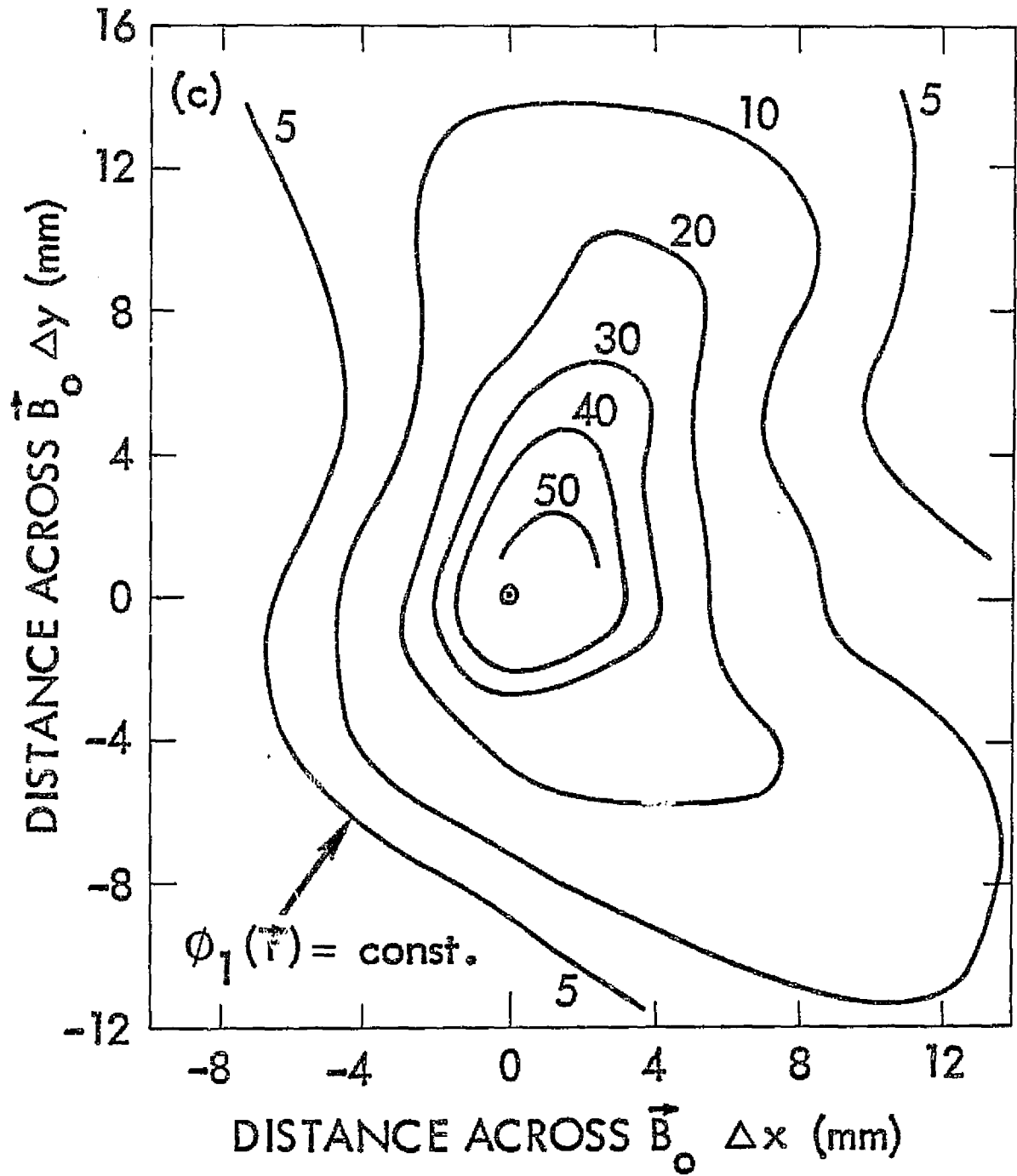


Fig 15(c)

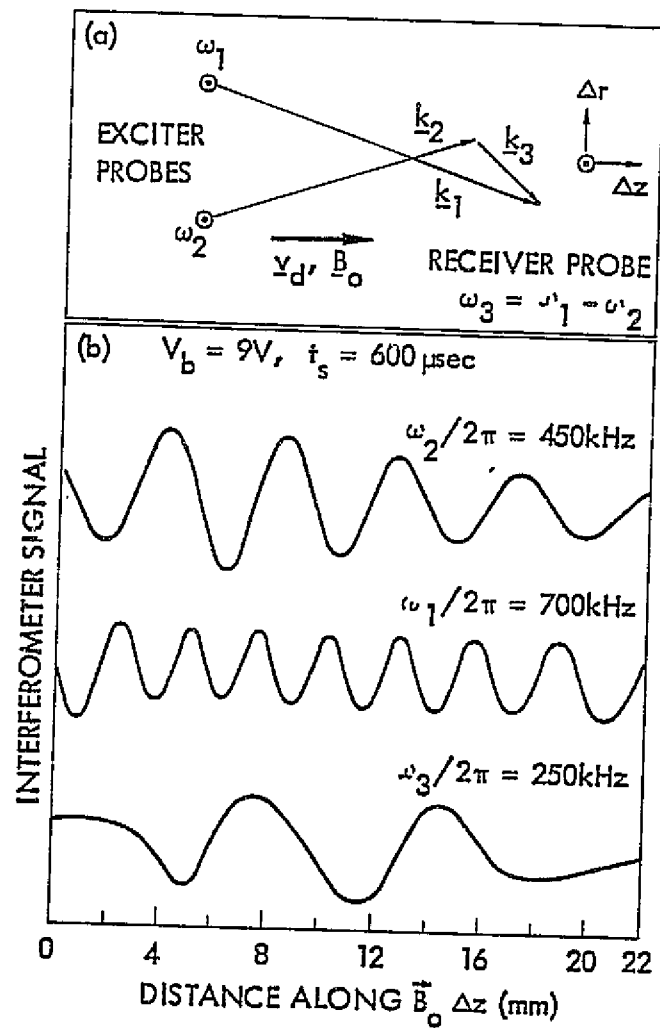


Fig. 16

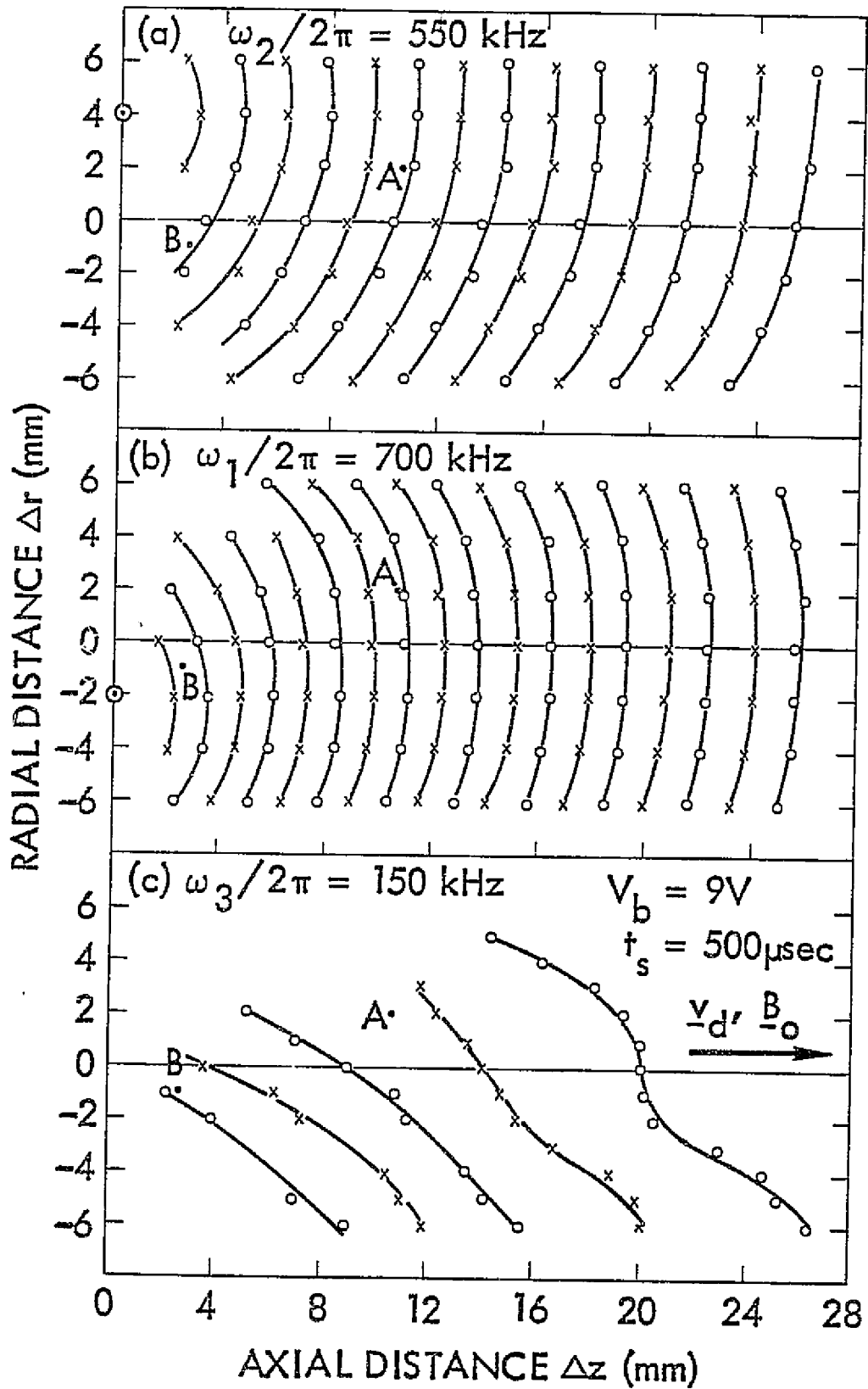


Fig. 17

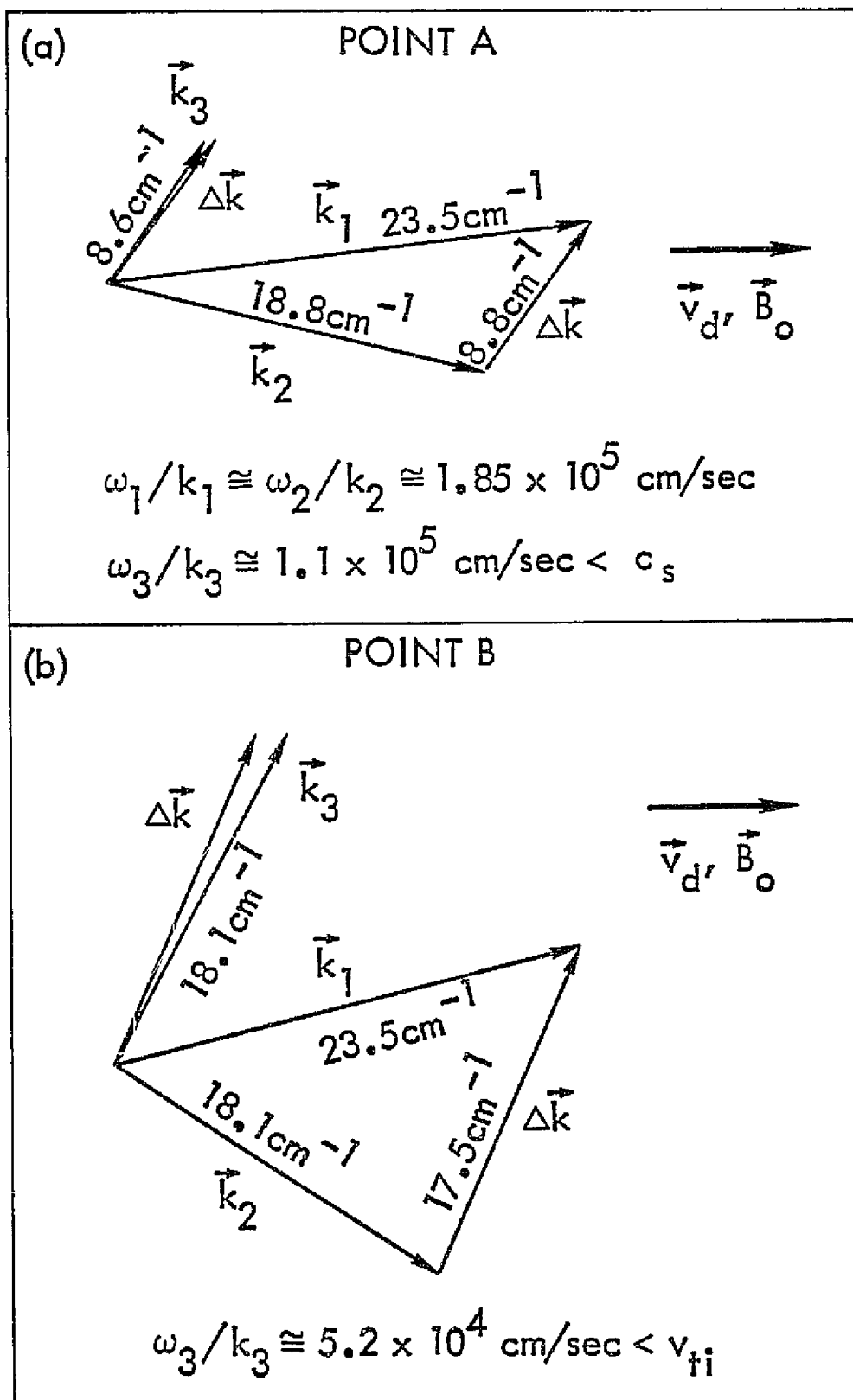


Fig. 18

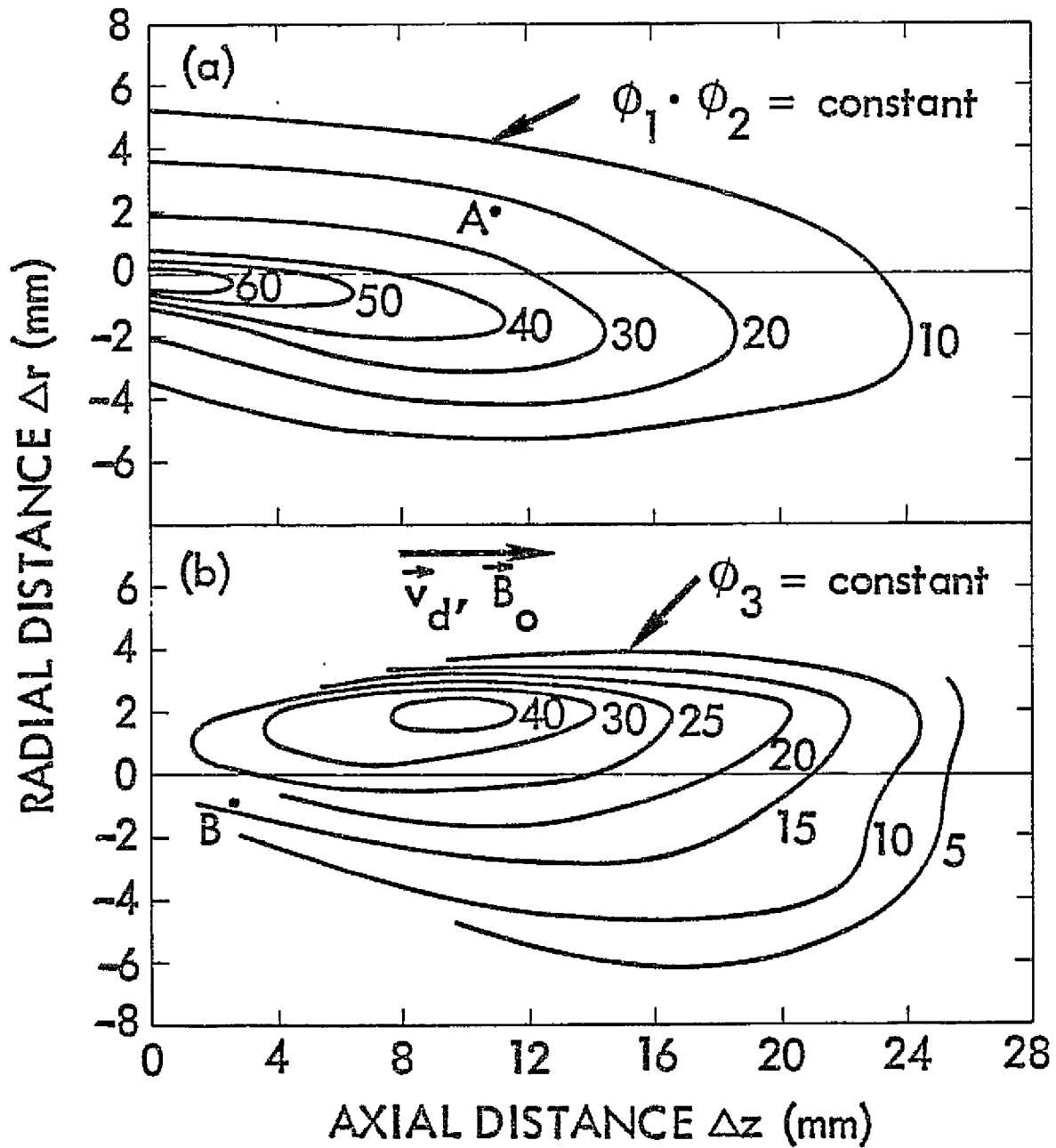


Fig. 19

N77-27262

APPENDIX D

THEORETICAL ASPECTS OF SOUNDER ANTENNA OPERATION

Principal Contributor: R.W. Fredricks

## I. INTRODUCTION

The operation of hard wire antenna systems immersed in a plasma which also contains an impressed magnetic field has been the subject of study for many years. The primary motivation has been to understand better the nature of signal transmission from satellites in or above the ionosphere. For frequencies well above the electron plasma frequency  $[f_{pe} = 9 \times 10^3 (n_e)^{1/2} \text{ Hz, where } n_e \text{ is the electron concentration in cm}^{-3}]$ , electromagnetic waves propagate quite freely, since the plasma dielectric "constant,"  $\epsilon \sim 1 - \omega_{pe}^2/\omega^2$ , is effectively unity, and thus for  $\omega \gg \omega_{pe}$  the propagation medium is approximately a vacuum. Thus, for VHF, UHF and SHF transmission, the predicted behavior of the antenna system may be well approximated by calculating the free-space radiation pattern, even though it is immersed in plasma.

However, there are two conditions under which the behavior of the antenna system will begin to deviate from that predicted by a free-space theory. First, even at frequencies well above the plasma frequency,  $\omega_{pe}$ , the nature of antenna behavior can be changed from free-space behavior by applying very hard drive (i.e., high input power) to the antenna. This can lead to such strong near fields that nonlinear plasma responses occur in the vicinity of the antenna. Examples of such apparent effects have been seen in data from sounder antenna experiments aboard the Alouette and the ISIS spacecraft (cf. bibliography section). This effect at high frequencies is of no concern to us in the present report.

The second condition under which antenna behavior becomes different from free-space behavior is one of operation at frequencies below the

electron plasma frequency. For the ionosphere/magnetosphere environment, this means operation at VLF, ELF and ULF. Quite aside from the problems associated with propagation of signals at these low frequencies in the inhomogeneous plasma and geomagnetic field above the ionospheric F layer, and the complex wave phenomena occurring when such waves impinge upon the earth/ionosphere cavity, and ionospheric "waveguides" formed in E and F layers (and also above the  $F_2$  peak), there are very important and so far unanswered questions concerning the way in which hard wire antenna systems couple energy into the surrounding ionospheric plasmas at frequencies  $\omega < \omega_{pe}$ .

## II. ELECTRIC DIPOLE ANTENNAS

Attempts to calculate the radiation from "short" electric dipole antennas immersed in a magnetoplasma and driven at frequencies  $\omega < \omega_{pe}$  (VLF and below) are quite numerous. They are listed under "Electric Dipoles" in the bibliography and reference section of this Appendix.

The fundamental problem of calculating the radiation from an electric dipole immersed in a magnetoplasma is one of solving Maxwell's equations coupled to the self-consistent field-particle equations describing the plasma. For very small applied antenna voltages, the plasma dynamics may be linearized, and the plasma reaction currents computed self-consistently in terms of the voltage on the antenna. Thus, the "short" dipole can be idealized as a point dipole of moment  $p_0 = C_A V_0 \ell$ , where  $C_A$  is the antenna element-to-plasma capacitance for a sheath of dimensions  $\sim$  several plasma Debye lengths and  $\ell$  is the dipole element's length.

In actual practice, it is at this point that the first difficulty with the antenna theory arises. Even for small signals, the sheath around such an antenna will exhibit a complex impedance. For larger signals,

that is for antenna voltages larger (or very much larger) than the mean thermal energy ( $kT_e$ ) of an electron divided by its charge (i.e., for  $V_0 >$  or  $\gg kT_e/e$ ), nonlinear effects appear. The usual sheath theory, and the concept of linear complex impedance are no longer valid. The coupling of energy fed to the antenna terminals to energy actually propagated away from the antenna in VLF, ELF or ULF modes is quite unknown. To the present date, no acceptable, or even believable theory is available to describe this highly nonlinear problem.

There are no (repeat, no) experiments available, either in the laboratory or on spacecraft, dealing with high-power, VLF to ULF radiation into a magnetoplasma. The only experimental work available so far is that involving sounder antennas aboard the Alouette and ISIS satellites [see bibliography and reference section], and an attempt to measure input impedance characteristics of a linear electric dipole on the USAF satellite OV 1-21 by the Aerospace Corporation group.

Other attempts to measure impedances of various configurations of small dipole-like receiving antennas were made during a NASA Javelin 8.45 rocket flight by Gurnett and co-workers at the University of Iowa.

In no case did any of the "resonances" or other peculiar phenomena predicted by the available theories of dipole antennas ever occur in the data, even in the small signal regime. In no case did the experiment attempted involve any measurement of the radiation from the antenna system.

In addition, it appears to us that no meaningful laboratory experiment has ever been performed to measure radiation from a dipole in a magnetoplasma at VLF and below. There are two laboratory experiments having some bearing on the problem, but they both have severe drawbacks that do not, in our opinion, allow extrapolation to the case of antennas in the ionosphere/magnetosphere. The first experiment is that of Fisher and

Gould (Reference B-1).

Contrary to a commonly held misconception, the Fisher-Gould theory and experiment neither calculated nor measured the far-field radiation from a short dipole. Their theory is based on a near-zone field approximation and involves a quasi-static ( $\underline{E} = -\nabla\phi$ ) assumption. Far-zone fields are known to have a primary dependence on the  $\nabla \times \underline{E}$  properties of Maxwell's equations. This same comment applies to the calculations by Kuehl (Reference B-2 and B-3) on the resonance cone interference phenomena found in oscillating electric doublets immersed in cold magnetoplasma.

The most complete attempt to calculate far-field radiation from an electric dipole antenna, keeping terms involving both  $\nabla \times \underline{E}$  and  $\nabla \cdot \underline{E}$ , has been carried out by Wang and Bell (References B-4 and B-5). The major drawbacks to these calculations are the nature of assumed plasma response (linearized cold\_magneto-fluid) and the assumed current distribution on the antenna itself (triangular). Neither assumption is generally correct, even under small applied antenna potentials, although the linearized fluid approximation is, perhaps, justifiable at small signal levels. However, the assumption of an effective radiating current distribution in the form of a triangular ramp on the two dipole elements may not so easily be justified. Statements to the effect that far fields are insensitive to the exact shape factor of the "small" dipole current distribution are simply extrapolations of results obtained in free-space calculations; there is no proof that such statements are correct for excitation by sources immersed in a magnetoplasma, especially for strong sources.

In fact, the conditions for strongly coupling antenna energy into some desired mode (such as the VLF Whistler) of the magnetoplasma will be a sensitive function of the geometry of the source current distribution. Since no spacecraft-borne experiment has yet been performed to look at radiation

from either electric dipoles or magnetic loops, one can only speculate concerning the actual efficiency for radiation at VLF by such systems. It is our opinion that laboratory experiments are now feasible and should be performed. (See Reference B-7)

### III. MAGNETIC LOOP ANTENNAS

For several reasons which will become clear subsequently, the magnetic loop antenna may perhaps avoid some of the problems besetting electric dipoles. The basis for this statement is simply that such loop antennas are current sources, rather than voltage sources, at VLF and below. The obnoxious effects of electrostatic (or quasi-static) sheaths and particle currents produced by sheath disturbances due to changing drive voltages applied to the antenna may be alleviated by the rather simple technical device of electrostatically shielding the loop conducting the current. At low enough frequencies the shield is relatively transparent to slowly varying magnetic fields, while preventing sheath conduction currents from becoming directly coupled to the antenna proper. Of course, currents may be induced in the electrostatic shield, and these will necessarily enter into the net driving current from which radiation is calculated.

There exist, in the literature, two publications in which Wang and Bell (References B-6 and B-7) have treated the problem of radiation of VLF and ELF waves by a loop antenna immersed in a cold magnetoplasma. The basic assumptions employed by these authors are similar to those invoked in the analysis of the electric dipole radiator discussed in the previous section. In effect, the response of the magnetoplasma was assumed to be described by linearized magneto-ionic equations, while the loop current strength was given. Thus, any plasma reaction back on the loop current other than that due to linear dynamical response was ignored to first approximation.

The Wang and Bell solutions to this problem are in the form of input

impedance of an arbitrary orientation with respect to magnetic field direction of the loop's axis of symmetry. They found that the loop orientation with respect to magnetic field did not have a very strong effect on the input impedance at VLF and ELF.

#### IV. SOME THEORETICAL ASPECTS OF ANTENNA-PLASMA COUPLING

Most of the past theory of operation of an antenna immersed in a magnetized plasma and driven at frequencies well below the electron plasma frequency has been based on notions that simple Debye Sheaths form, and plasma currents are linearized responses to the antenna's applied field.

Although under the present contract, both time and resources prevented a detailed theoretical treatment of the antenna-plasma coupling phenomenon, it is still pertinent to outline the elements of such a theory and to point out the novel elements of our approach to such a theory, an approach significantly different from previous ones.

##### A. Electric Dipole Antenna

Consider an electric dipole antenna immersed in a magnetized plasma of electron and ion temperatures  $T_e$ ,  $T_i$ , charge density  $n$ , and magnetic field  $B_0$  can be assumed. For purposes of simplicity, consider the dipole gap to have dimensions small compared to the length of the wires.

One notes that a planar sheet of field lines of  $B_0$  intersect the conducting antenna elements. In the absence of any voltages applied to the antenna, its conducting elements will float to some small potential,  $V_0 \approx kT_e/e$ , (i.e., determined by the plasma potential), so that equal thermal currents of ions and electrons are collected by the antenna surface. Note that these currents are collected primarily along lines of  $B_0$  representing guiding centers within one Larmor radius of the antenna.

Now, consider a "d.c." operation of the dipole, in which one element is driven at  $-V_1$  and the other at  $+V_1$  relative to their common ground. If  $V_1$  exceeds the order of  $V_0$ , then the antenna element at  $-V_1$  repels electrons, while that at  $+V_1$  attracts electrons, with reverse effects on the plasma ions.

Under this "d.c." mode, no change in plasma potential can occur in the plasma on field lines intersecting the half of the antenna at  $-V_1$ , because the ion current remains saturated. However, the plasma on field lines intersecting the half of the antenna at  $+V_1$ , electrons can be drawn from the plasma to the antenna, which leaves a negative charge deficiency along those field lines, and the plasma potential there assumes a larger positive value than it had previously.

For this reason, a strong electric field will develop along an interface between the regions defined by field lines intersecting the positively biased antenna element, and regions of non-intersecting field lines. This electric field is perpendicular to local field lines.

The electrons which participate in changing this plasma potential are predominantly fast, being the electron population with speeds on the order of or exceeding the mean thermal speed. Thus, a rather sizable volume of plasma can have its potential increased in this manner.

If the potential on the dipole is  $V_1 \sin \omega t$ , instead of d.c., then the plasma potential can be changed in volumes by each half of the antenna on alternate cycles, and such disturbances will lead to possible excitation of plasma modes, depending upon the applied frequency.

This effect has been observed in laboratory plasmas at TRW, and requires further investigation. It appears to represent a mechanism whereby excitation of a plasma at frequencies well below the electron plasma frequency can be effected.

A general model based on this concept can be constructed and examined theoretically and investigated experimentally. Because the electric fields produced are predominately normal to local  $B_0$ , it appears certain that very effective excitation of Bernstein and cyclotron waves will occur under appropriate conditions on the frequency.

BIBLIOGRAPHY

ELECTRIC DIPOLE ANTENNAS

A. Theoretical Calculations - Radiation Field

Balmain, K.G., "The Impedance of a Short Dipole Antenna in a Magneto Plasma", IEEE Transactions of the Professional Group on Antennas and Propagation, AP-12, 605, 1964.

Blair, W.E., "The Driving Point Impedance of an Electrically Short Cylindrical Antenna in the Ionosphere", Technical Report Number EE-109, Engineering Experiment Station, University of New Mexico, Albuquerque, 1964.

Galejs, Janis, "Impedance of a Finite Insulated Cylindrical Antenna in a Cold Plasma with a Longitudinal Magnetic Field", IEEE Transactions of the Professional Group on Antennas and Propagation, AP-14, 727, 1966<sup>a</sup>.

Galejs, Janis, "Impedance of a Finite Insulated Antenna in a Cold Plasma with a Perpendicular Magnetic Field", IEEE Transactions of the Professional Group on Antennas and Propagation, AP-14, 737, 1966<sup>b</sup>.

Seshadri, S.R., "Radiation Resistance of Elementary Electric-Current Sources in a Magnetoionic Medium", Proceedings of the Institute of Electrical Engineers, London, 112, 1856, 1965.

Staras, H., "The Impedance of an Electric Dipole in a Magnetoionic Medium", IEEE Transactions of the Professional Group on Antennas and Propagation, 12, 695, 1964

Weil, H. and D. Walsh, "Radiation Resistance of an Electric Dipole in a Magnetoionic Medium", IEEE Transactions of the Professional Group on Antennas and Propagation, AP-12, 297, 1964.

B. Resonance Cone-Quasi Static

Singh, N., "Effect of a Sheath on the Fields of a Probe in a Hot Magnetized Plasma", Physics of Fluids, 16, 698, 1973.

Singh, N. and R.W. Gould, "Waves in a Hot Uniaxial Plasma Excited by a Current Source", Physics of Fluids, 16, 75, 1973.

C. Langmuir Probe Action at ULF, and Sheath Effects

Fiala, V., "Mutual Impedance of Two Small Dipoles in Warm Streaming Plasma to Measure Cherenkov Cone of Plasma Waves", Journal of Plasma Physics, 10, 337, 1973.

Hauck, J.P., N. Rynn, and G. Benford, "Observation of Sheath Excitation of Electrostatic Waves and Ion Bursts in a Plasma," Physics of Fluids, 16, 1964, 1973.

LaFon, J.P., "On the Perturbation of a Plasma and Particle Collection by a Cylinder in a Magnetic Field," Journal of Plasma Physics, 10, 383, 1973.

Meyer, P., N. Vernet, and P. Lassudrie-Duchesne, "Theoretical and Experimental Study of the Effect of the Sheath on an Antenna Immersed in a Warm Isotropic Plasma," Journal of Applied Physics, 45, 700, 1974.

Prewett, P.D., and J.E. Allen, "Ion Refraction Waves in Cylindrical and Spherical Geometries," Journal of Plasma Physics, 10, 451, 1973.

Segall, S.B. and D.W. Koopman, "Application of Cylindrical Langmuir Probes to Streaming Plasma Diagnostics," Physics of Fluids, 16, 1149, 1973.

#### D. ISIS and Alouette Satellite Sounder Antenna Results

Barrington, R.E. and T.R. Hartz, "Resonances Observed by the Alouette Topside Sounders," in Plasma Waves in Space and in the Laboratory, [editors: J.O. Thomas and B.J. Landmark], University of Edinburgh Press, Elsevier Publishing Company, New York (page 55 et seq.), 1969.

Florida, C.D., "The Development of a Series of Ionospheric Satellites," Proceedings of the IEEE, 57, 867, 1969.

Graff, P., "Influence de la Gyrofrequence Protonique sur la Resonance d'une Antenne a la Frequence du Plasma Electronique," C.R.H. Academie du Science, Series B, 265, 618, 1967.

Palmer, F.H. and R.E. Barrington, "Excitation of Ion Resonances by the ISIS-2 HF Transmitter," Journal of Geophysical Research, 78, 8167, 1973.

#### E. Impedance Measurements in Space

Gurnett, D.A., G.W. Pfeiffer, R.R. Anderson, S.R. Mosier and D.P. Cauffman, "Initial Observations of VLF Electric and Magnetic Fields with the Injun 5 Satellite," Journal of Geophysical Research, 74, 4631, 1969.

Koons, H.C., D.A. McPherson and W.B. Harbridge, "Dependence of VLF Electric Field Antenna Impedance on Magnetospheric Plasma Density," Journal of Geophysical Research, 75, 2490, 1970.

Koons, H.C., F.A. Morse and D.A. McPherson, "Final Report for the NASC-117 Satellite Experiment: Measurement of the Nonlinear Impedance and Nonlinear Plasma Effects in the Near Field of an Electric Dipole Antenna," Aerospace Report No. TR-0074(9260-09)-1, Aerospace Corporation, El Segundo, California, October 15, 1973.

Shawhan, S.D. and D.A. Gurnett, "VLF Electric and Magnetic Fields Observed with the Javelin 8.45 Sounding Rocket," Journal of Geophysical Research, 73, 5649, 1968.

REFERENCES

- B-1. Fisher, R.K. and R.W. Gould, "Resonance Cones in the Field Pattern of a Radio-Frequency Probe in a Warm Anisotropic Plasma", Physics of Fluids, 14, 857, 1971
- B-2. Kuehl, H.H., "Electromagnetic Radiation from an Electric Dipole in a Cold Anisotropic Plasma", Physics of Fluids, 5, 1095, 1962
- B-3. Kuehl, H.H., "Interference Structure Near the Resonance Cone", Physics of Fluids, 16, 1311, 1973
- B-4. Wang, T.N.C. and T.F. Bell, "Radiation Resistance of a Short Dipole Immersed in a Cold Magnetoionic Medium", Radio Science, 4, 167, 1969
- B-5. Wang, T.N.C. and T.F. Bell, "On VLF Radiation Resistance of an Electric Dipole in a Cold Magnetoplasma", Radio Science, 5, 605, 1970
- B-6. Wang, T.N.C. and T.F. Bell, "VLF/ELF Input Impedance of an Arbitrarily Oriented Loop Antenna in a Cold, Collisionless Multicomponent Magnetoplasma", IEEE Transactions of the Professional Group on Antennas and Propagation, AP-20 (communication), 394, 1972
- B-7. Stenzel, R.L., "Antenna Radiation Patterns in the Whistler Regime Measured in a Large Laboratory Plasma," Radio Science, 11, 1045-1056, 1976

N77-27263

APPENDIX E

WHISTLER MODES IN BOW SHOCKS

Principal Contributor: E.W. Greenstadt

## WHISTLER SHOCK RELAXATION

Background

One of the modes of electromagnetic wave propagation in the solar wind is the whistler mode familiar in the magnetosphere and the laboratory. Presumably, any source of wave generation in the solar wind should produce whistlers, which will travel at phase and group velocities dependent on frequency, on the local plasma parameters, and on the direction of propagation with respect to the interplanetary magnetic field (the IMF). Any shock wave, including the earth's bow shock, is such a source, and the detection and behavior of whistlers in the solar wind near the bow shocks of Earth and Mercury has been the subject of reports by Fairfield (1974) and Fairfield and Behannon (1976).

In general, waves cannot propagate upstream from the bow shock into the oncoming solar wind. Indeed, the shock forms because the wind flows "super-magnetosonically." However, whistler, or fast, waves constitute the one mode that includes zero frequency in its range and that, for some frequencies and directions, can propagate upstream under fairly common parameter conditions. Dispersed whistler phase and group velocities are highest, regardless of direction, at frequencies somewhat below the electron gyrofrequency  $f_{ce}$ . These are the frequencies at which wave speeds are most likely to exceed the solar wind velocity  $V_{SW}$ , with waves running away from the shock, as reported by the authors cited above. At lower frequency, the phase velocity may match  $V_{SW}$ , with the result that the perpendicular-shock jump profile is strongly modified by the addition of whistler standing waves ahead of it in the solar wind, at least in laminar structures, when the IMF is about  $10^\circ$ - $40^\circ$  from the shock "front." Such standing wave profiles have been observed in the laboratory

(Robson, 1969) and in space (Greenstadt et al., 1975; Fairfield and Feldman, 1975). The whistler mode, then, is an important component, both theoretically and experimentally, in shock structure.

Certainly the most profound significance of the whistler mode for shock structure must occur when waves with the widest possible band of frequencies, especially including those low enough to approach the ion cyclotron frequency, are capable of overmatching the solar wind velocity and carrying a significant portion of the shock's energy upstream. This situation probably contributes to the total breakdown of shock discipline when the IMF,  $B$ , is less than about  $50^\circ$  from the local shock normal (Greenstadt et al., 1976). The properties of whistlers that lead to such shock "relaxation" is the subject of the study reported in this section.

Relaxation of a quasi-parallel plasma shock is a process of considerable complexity involving counterstreaming particles, local electric and electromagnetic wave excitation, wave amplification, reduced stream thermalization, upstream plasma modification, and energy escape by wave propagation. The part played by simple wave escape through the whistler mode has never been investigated thoroughly, particularly for typical solar wind plasmas, arbitrary angles of the IMF, and realistic curved shock profiles.

#### Objective

The objective of this study is to characterize fully the behavior of the whistler mode for arbitrary angles of propagation to  $B$ , under representative solar wind conditions. It is hoped that in this way the contribution of whistlers to quasi-parallel structure can eventually be assessed and described.

Approach

The initial attack on the problem outlined above proceeds from a simplified basis with the intention of restoring neglected complications later. The sections of the whistler dispersion curves where dissipation of shock energy must take place first are those where phase and group velocities are highest, i.e., where  $f_{ci} \ll f < f_{ce}$ . In this range of frequencies the Appleton-Hartree (A-H) approximation applies for cold plasma, and this defines the beginning approach.

The A-H dispersion relation for the fast mode (Stix, 1962, p 40) gives the phase velocity expression

$$u_{\phi}^2 = \left(\frac{\omega}{k}\right)^2 = c^2 \left(\frac{f_{ce}}{f_{pe}}\right)^2 \left[ \frac{f}{f_{ce}} \cos \theta - \left(\frac{f}{f_{ce}}\right)^2 \right]$$

where  $u_{\phi} = u_{\phi} k$ ,  $\theta$  is the angle between propagation vector  $k$  and  $B$ , and  $f_{ce}$  and  $f_{pe}$  are the electron cyclotron and electron plasma frequencies. The group velocity  $u_g$  of the waves differs in general in both speed and direction from  $u_{\phi}$ . If we take

$$\underline{u}_g = u_g \cos \theta \underline{B} + u_g \sin \theta \underline{B}_{\perp}$$

where  $\theta_g$  is the angle between  $\underline{u}_g$  and  $\underline{B}$ , and  $\underline{B}_{\perp}$  is a vector perpendicular to  $\underline{B}$  in the plane of  $\underline{u}_g$  and  $\underline{B}$ , the selected approximation gives, from  $\underline{u}_g = \frac{d\omega}{dk}$ ,

$$u_g^2 = \frac{u_{\phi}^2}{\cos^2 \theta} \left[ 3 \cos^2 \theta - 8 \frac{f}{f_{ce}} \cos \theta + 4 \left(\frac{f}{f_{ce}}\right)^2 + 1 \right]$$

and

$$\tan \theta_g = \left( \cos \theta - 2 \frac{f}{f_{ce}} \right) \tan \theta / \left[ \left( \cos \theta - 2 \frac{f}{f_{ce}} \right) + \frac{1}{\cos \theta} \right].$$

Obviously, even this simplified cold plasma approximation connects  $u_g$  and  $\theta_g$  through expressions whose properties are less than self-evident.

The plan is to exploit the above approximation to study the properties of whistler propagation in realistic solar wind models surrounding a model bow shock to see if any pattern of wave escape can be linked to experimental results describing the development of quasi-parallel structure.

### Status

In addition to derivation of the above mathematical model, a program has been written to compute and plot various versions of the elaborated relationships, and preliminary graphs have been constructed for a few parameter conditions, principally to test the program. Figure 1 is a sample polar plot of phase and group velocities vs angle for one frequency and one set of typical (cold) solar wind quantities,  $B = 5\gamma$ ,  $N = 7 \text{ cm}^{-3}$ , which determine  $f_{ce}/f_{pe}$ . The figure tells us that, for the selected quantities, the phase velocity would exceed a nominal solar wind velocity of 400 km/sec (dashed curve) at all angles  $\theta \leq 52^\circ$ , while the corresponding group velocity would be more than double the solar wind speed, but only for angles  $\theta_g \leq 15^\circ$ .

In application, the actual relationship of  $\underline{B}$  to the local shock normal and the appropriate component of solar wind velocity must be taken into account to determine the pattern of whistler wave escape from the shock. At the time of writing, the study has not been carried beyond production of a few test plots such as that in Figure 1. Eventually, it is hoped that a comprehensive picture of wave front and bow shock geometry will be developed.

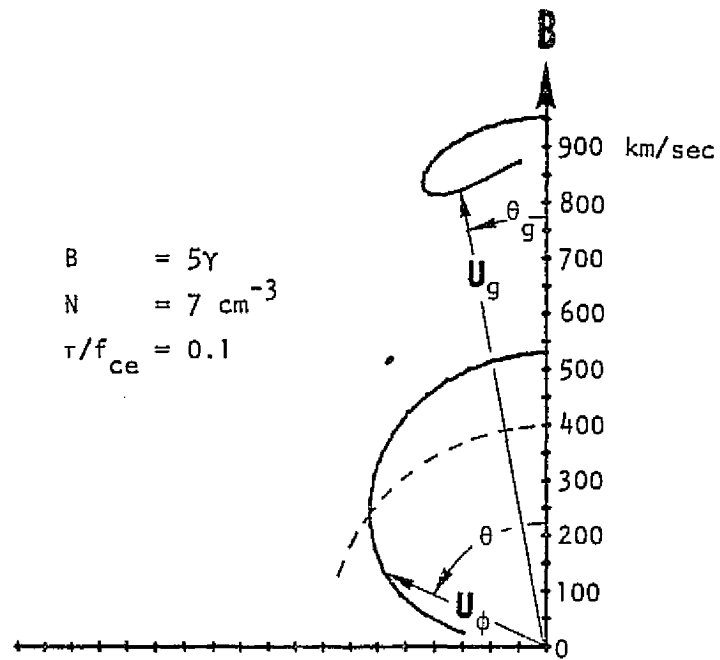


Figure 1. Polar plot of whistler phase and group velocities for one set of solar wind parameters.

REFERENCES

- Fairfield, D. H., Whistler waves observed upstream from collisionless shocks, J. Geophys. Res., 79, 1368, 1974.
- Fairfield, D. H., and Behannon, K. W., Bow shock and magnetosheath waves at Mercury, J. Geophys. Res., 81, 3897, 1976.
- Greenstadt, E. W., C. T. Russell, F. L. Scarf, V. Formisano, and M. Neugebauer, Structure of the quasi-perpendicular, laminar bow shock, J. Geophys. Res., 80, 502, 1975.
- Greenstadt, E. W., C. T. Russell, V. Formisano, P. C. Hedgecock, F. L. Scarf, M. Neugebauer, and R. E. Holzer, Structure of the quasi-parallel, quasi-laminar bow shock, J. Geophys. Res., 82, 651, 1977.
- Robson, A. E., Experiments on oblique shock waves, Spec. Publ. 51, ESRO, Frascati, Italy, p 159, 1969.
- Stix, T. H., The Theory of Plasma Waves, McGraw-Hill, New York, 1962.